Pontifícia Universidade Católica
do Rio de Janeiro

Lisseth Saavedra Patiño

Some novel full-wave, variational, and perturbational pseudo-analytic methods for electromagnetic propagation modeling in complex geophysical formations

Tese de Doutorado

Thesis presented to the Programa de Pós–graduação em Engenharia Elétrica of PUC-Rio in partial fulfillment of the requirements for the degree of Doutor em Engenharia Elétrica.

Advisor : Prof. José Ricardo Bergmann
Co-advisor: Prof. Guilherme Simon da Rosa

Rio de Janeiro
May 2020

Pontifícia Universidade Católica
do Rio de Janeiro

Lisseth Saavedra Patiño

Some novel full-wave, variational, and perturbational pseudo-analytic methods for electromagnetic propagation modeling in complex geophysical formations

Thesis presented to the Programa de Pós–graduação em Engenharia Elétrica of PUC-Rio in partial fulfillment of the requirements for the degree of Doutor em Engenharia Elétrica. Approved by the Examination Committee.

Prof. José Ricardo Bergmann
Advisor
Centro de Estudos em Telecomunicações – PUC-Rio

Prof. Guilherme Simon da Rosa
Co-advisor
Centro de Estudos em Telecomunicações – PUC-Rio

Prof. Emanoel Paiva de Oliveira Costa
Centro de Estudos em Telecomunicações – PUC-Rio

Prof. Adaildo Gomes D'Assunção
Universidade Federal do Rio Grande do Norte – UFRN

Prof. Flavio Jose Vieira Hasselmann
Centro de Estudos em Telecomunicações – PUC-Rio

Prof. Cássio Gonçalves do Rego
Universidade Federal de Minas Gerais – UFMG

Rio de Janeiro, May the 8th, 2020

Lisseth Saavedra Patiño

Lisseth Saavedra Patiño received the B.S. degree from the Nariño University, Nariño, Colombia, in 2013, and the M.S. degree from the Pontifical Catholic University of Rio de Janeiro (PUC-Rio), Rio de Janeiro, Brazil, in 2016, both in electrical engineering. She is currently pursuing the Ph.D. degree at PUC-Rio. Her research interests include pseudoanalytical techniques for geophysical well-logging applications and physical-optics-based solutions for high-performance reflector antenna.

Bibliographic data

Lisseth Saavedra Patiño

Some novel full-wave, variational, and perturbational pseudo-analytic methods for electromagnetic propagation modeling in complex geophysical formations / Lisseth Saavedra Patiño; advisor: José Ricardo Bergmann; co-advisor: Guilherme Simon da Rosa. – Rio de janeiro: PUC-Rio, Departamento de Engenharia Elétrica, 2020.

v., 110 f: il. color. ; 30 cm

Tese (doutorado) - Pontifícia Universidade Católica do Rio de Janeiro, Departamento de Engenharia Elétrica.

Inclui bibliografia

1. Engenharia Elétrica – Teses. 2. Técnicas de casamento de modos;. 3. Aproximação baseada no método de Born;. 4. Técnicas de onda completa;. 5. Espalhamento;. 6. Sensores para prospecção de petróleo.. I. Bergmann, José Ricardo. II. Simon da Rosa, Guilherme. III. Pontifícia Universidade Católica do Rio de Janeiro. Departamento de Engenharia Elétrica. IV. Título.

CDD: 621.3

Acknowledgments

First, I would like to thank my beloved family, especially my parents Gladis and Wilfredo, my brother Sebastian, my niece Antonia, my grandmothers Blanca and Maria, my boyfriend Álan, my aunts and cousins. They are always present in my daily life, thank you for teaching me that effort is the tool for success, for believing in me, and supporting me at all times.

I would deeply thank my advisors Bergmann and Guilherme Rosa for giving me the honor of working with them. I have immense gratitude and admiration. Their excellent guidance and patience inspired me to become a better researcher and person.

I thank the members of my doctoral committee, the CETUC staff and the PUC-Rio. I also would like to thank all professors who taught and motivate me in the aspects of the Electromagnetic Theory.

I would like to thank my colleagues and friends from CETUC, especially Keyla, Gidy, Guille, Jenni, Andy, Marcelo, Carlos O., Teddy, Junior, Mauricio, Américo, Albert, Jose C., Juano, André, Andrea, Tamara, Alireza, Lukas, Elizabeth, Javier O., Johnes, Edson, Uwe, Darwin, Azucena, Dailys, Yuneisi, Juliana, Diego, Cháo. I shared unforgettable moments with them.

I would also like to thank my friends and flatmates in Brazil, especially Jose R., Carlos P, Jose B., Lesslie, Camilo, Himer, Cris, Daniel, Lili, Evelina, Oscar, Javier P., Vanesa, Cesar, Luis T., Roxi, André B., Julia P., Marcos R., Thais A., Taís P., Fátima, Elliot, Ruberth, Julia V., Dalai and my friends in department of informatics. They made this journey happier.

Finally, I would like to thank CNPq, for their financial aid.

Abstract

Lisseth Saavedra Patiño; Bergmann, José Ricardo (Advisor); Simon da Rosa, Guilherme (Co-Advisor). **Some novel full-wave, variational, and perturbational pseudo-analytic methods for electromagnetic propagation modeling in complex geophysical formations**. Rio de Janeiro, 2020. 110p. Thesis – Departamento de Engenharia Elétrica, Pontifícia Universidade Católica do Rio de Janeiro.

This work presents a comprehensive study on some techniques for modeling electromagnetic sensors used in well prospecting. These sensors are usually immersed in complex geophysical formations (inhomogeneous, dissipative, and anisotropic) with multiscale dimensions and constitutive parameters of the medium abruptly varying, resulting in a challenging problem for conventional computational electromagnetic techniques. Our proposal overcomes these problems and contributes to a better understanding of the physical electromagnetic phenomena that occur in these structures. We analyzed the propagation problem by using: a) a full-wave method based on the mode-matching technique, b) perturbational solutions for solving a Fredholm integral equation on the grounds of the Born approximation, and c) variational methods for calculating the sensor impedance. We present results that demonstrate the ability of the techniques introduced in this dissertation to accurately and efficiently modeling electromagnetic sensors in a more realistic fashion when compared with other methods available in the literature.The computational cost of the numerical algorithms developed in this work is relatively low if compared to that required in traditional techniques (such as finite elements, finite differences, and method of moments).

Keywords

Mode-matching techniques; Born-based approximation; Full-wave techniques; Scattering; Well-logging sensors.

Resumo

Lisseth Saavedra Patiño; Bergmann, José Ricardo; Simon da Rosa, Guilherme. **Métodos pseudo-analíticos de onda completa, variacionais e de perturbação para modelagen da propagação eletromagnética em formações geofísicas complexas**. Rio de Janeiro, 2020. 110p. Tese de doutorado – Departamento de Engenharia Elétrica, Pontifícia Universidade Católica do Rio de Janeiro.

Este trabalho apresenta um estudo abrangente sobre novas técnicas para modelagem de sensores eletromagnéticos usados na prospecção de petróleo. Estes sensores normalmente ficam imersos em formações geofísicas complexas (não homogêneas, dissipativas e anisotrópicas) com dimensões e parâmetros constitutivos do meio envolvendo múltiplas escalas, e isso representa um problema desafiador para as técnicas tradicionais de eletromagnetismo computacional. Nossa proposta supera esses problemas e contribui para uma melhor compreensão dos fenômenos eletromagnéticos físicos que ocorrem nessas estruturas. Analisamos o problema de propagação usando: a) uma técnica de onda completa baseada no método de casamento de modos, b) soluções perturbacionais para a equação integral de Fredholm vetorial baseadas na aproximação de Born, e c) métodos variacionais para o cálculo da impedância dos sensores eletromagnéticos de interesse para a exploração geofísica. Nós apresentamos resultados que demostram a capacidade das técnicas introduzidas nesta tese para modelar de forma acurada e eficiente sensores eletromagnéticos de forma mais realista do que as alternativas disponiveis na literatura. O custo computacional dos algoritmos desenvolvidos é relativamente baixo comparado com técnicas puramente numéricas tradicionais (tais como os métodos de elementos e diferenças finitas ou o método dos momentos).

Palavras-chave

Técnicas de casamento de modos; Aproximação baseada no método de Born; Técnicas de onda completa; Espalhamento; Sensores para prospecção de petróleo.

Table of contents

List of figures

List of Abreviations

BA	–	Born approximation
CEM	–	Computational electromagnetics
EBA	–	Extended Born approximation
FDTD	–	Finite-difference time-domain method
FEM	–	Finite element method
GSM	–	Generalized scattering matrix
LWD	–	Logging while drilling
MMT	–	Mode-matching technique
NMM	–	Numerical mode-matching
MoM	–	Method of Moments
PEC	–	Perfect electric conductor
PML	–	Perfectly matched layer
RX	–	Receiver
TX	–	Transmitter

1
Introduction

1.1
General Introduction

The focus of this thesis is to explore full-wave, variational, and perturbational pseudo-analytic methods for electromagnetic propagation modeling in complex geophysical formations. These methods will be used for describing modern electromagnetic sensors employed by the oil and gas industry in well logging prospecting for hydrocarbon reservoirs. Well logging is the process of recording data about the geophysical characteristics of the media by using a measurement device crossing the media. This process has been used by a geologist as a mapping technique for exploring the earth subsurface, for a geophysicist, as support for surface seismic analysis, for a reservoir engineer to collect data for providing values to use in a simulator, and for a petrophysicists to evaluate the potential hydrocarbon production of a reservoir [2]. In this research, we will draw attention to the hydrocarbon and gas applications due to its industry and economic importance. The well-logging measurement methods comprise electrical, nuclear, and acoustic techniques [2 – 4]. It is due that the evaluated parameters could be sensitive to the properties of the geophysical formation or the fluid inside the rock porous. Modern petrophysics evaluation tools, as that illustrated in Figure 1.1, use several measurement devices to obtain the characteristics of the soil and the rocks surrounding the borehole [1, 3, 4]. In this thesis, we will focus on electromagnetic sensors.

In the past years, the data acquired by the logging sensors were transmitted to a surface station by using a wireline. This process is known as wireline logging, and the measurements are executed after the drilling completion [2, 5, 6]. Since the last decade, the wireline is giving way to modern logging-while-drilling (LWD) tools that have enabled real-time characterization of the lithological variations in the soil surrounding a prospecting oil well. In this configuration, both logging and drilling processes are performed at the same time that the borehole is drilled, by allowing the improving the early identification of potential pay-zones.

Electromagnetic LWD sensors are typically comprised of an array of

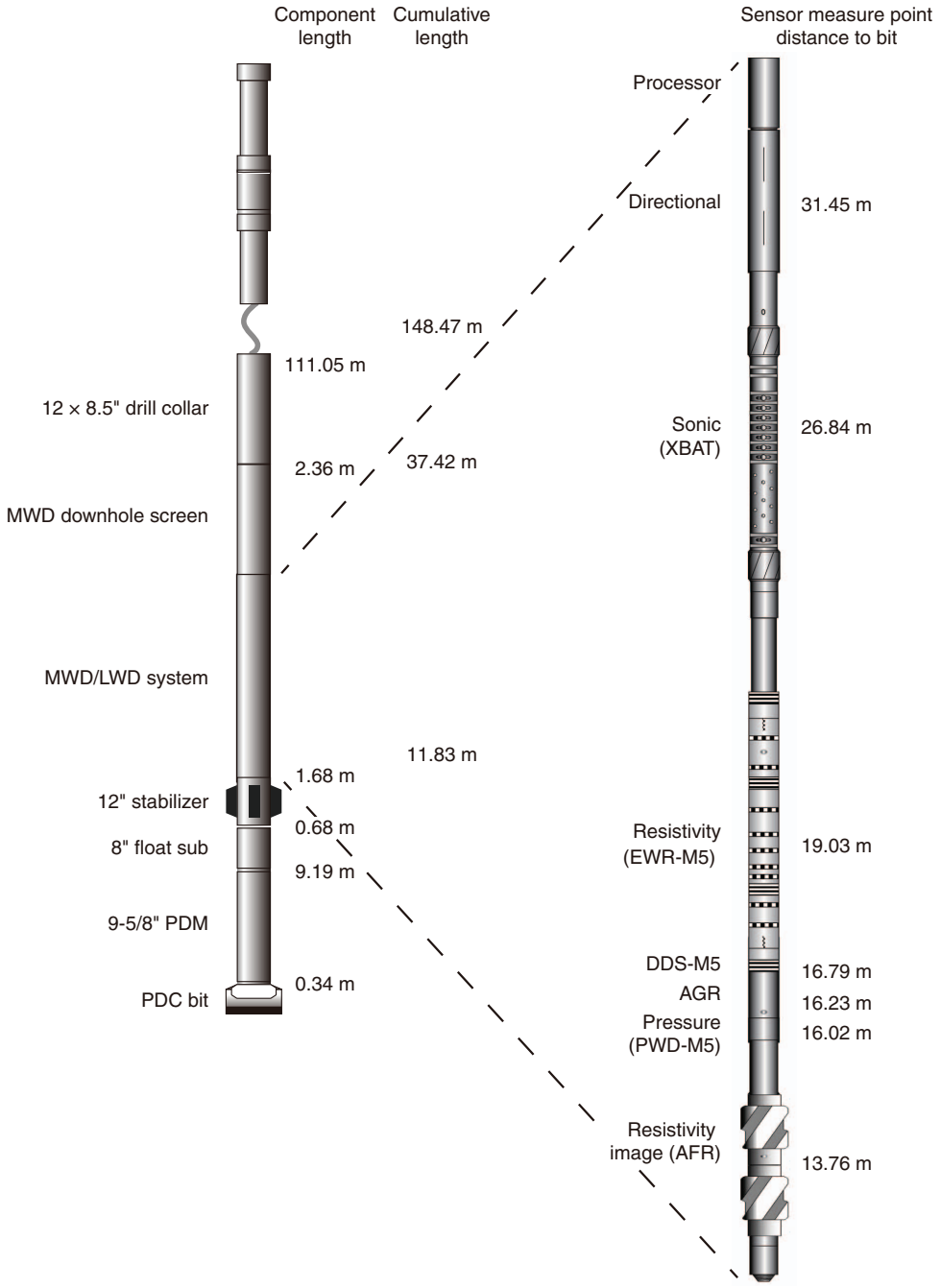

Figure 1.1: Example of a commercial measurement-while-drilling/logging-while-drilling (MWD/LWD) tool. This tool employs a bottom-hole assembly using a 12.25 inch mandrel. There are several sensors and devices installed on the drilling tube, including: PDM = positive displacement motor, PDC = polycrystalline diamond compact, XBAT = X-Bimodal AcousTic sonic, EWR = electromagnetic wave resistivity, DDS = drill string dynamic sensor, AGR = azimuthal gamma ray, PWD = pressure while drilling, AFR = azimuthal focused resistivity. Source [1].

horizontal or tilted-coil antennas wrapped around a metallic mandrel [7 – 14], as illustrated in Figure 1.1 and in Figure 1.2. The coil antennas operate in the

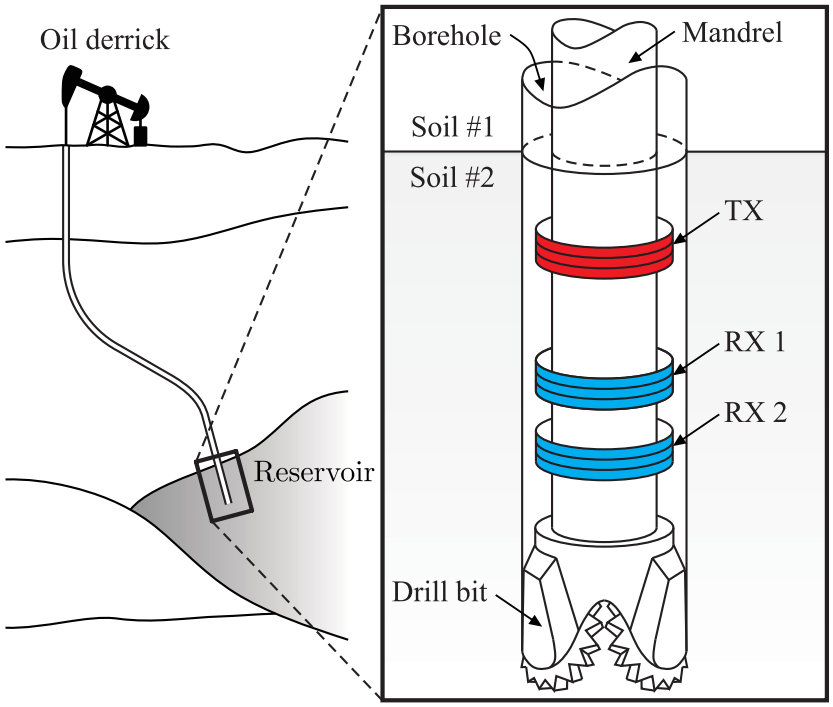

Figure 1.2: A typical planed well using of a triaxial LWD sensor within a complex geophysical formation.

frequency range from 100 kHz to 1 GHz, with a prevalence sensors dedicated to the frequencies of 2 MHz and 400 kHz [3, 4, 13]. The receivers (RXs) are distributed over the mandrel, up to a couple of meters away from the (TXs). The induced voltage at the RX antennas is measured during the drilling process, and its relative amplitudes and phase differences can be used in inverse algorithms for establishing the constitutive parameters of the medium surrounding the borehole.

The soil formations are generally complex, formed by inhomogeneous, dispersive, and anisotropic rocks. The anisotropy is given by some geological features such as the presence of sand and clay in the formation or the invasion of salt water in a directional soil fracture [15]. Such media characteristics will dictate the electromagnetic propagation of the fields radiated by the transmitter antennas [16 – 19]. Therefore, the induced voltage at the RX sensors will be strongly affected by the electromagnetic properties of the soil, including the electric conductivity (σ) and permittivity (ϵ) as well as the magnetic permeability (μ). For the typical LWD operation frequencies, however, the concerns are on σ and μ because the displacement currents are dominated by the conduction ones. It is especially important to characterize σ because high-resistivity media (or its inverse: low electrical conductivity) are frequently associated with the hydrocarbon concentration.

Computation electromagnetics (CEM) techniques can be used to model

the electromagnetic fields in the *direct problem*, where we know both sources (our the TXs) and the media. Thus, the simulation results for the voltages at the RXs are then used as a basis for an iterative reconstruction algorithm that solves the *inverse problem*, i.e., it correlates the RX voltages with the apparent soil resistivity [5,20,21]. For ensuring the accurate modeling of the LWD sensor response, a mathematical method should incorporate the media (with inhomogeneities and complex anisotropies) and geometry descriptions in a realistic fashion. Generally, a vertical well comprises a metallic mandrel concentric with a borehole and a geological formation surrounding the drilling tool [21 – 25], as that illustrated in Figure 1.3. The geological formation (background media) are usually approximated by a set of vertically homogeneous stacked layers [26 – 28] or, in a more realistic model, by a cylindrically-layered medium with both vertical and radial layers [21 – 25]. Such choices make easy the boundary conditions enforcement because of the cylindrical conformation. However, such models may be inadequate for representing underground prospecting scenarios with non-symmetric geometries. Consider, for instance, the case depicted in Figure 1.3: a scattering object will disturb the RX voltage response. The scattering objects can be used to represent a real-world matter, such as a mud-invaded zone, an injection well drilled parallel to the main production line, a hydraulic fracture in the formation, a dipping (tilted) layer, among others [15, 28 – 31]. We believe that the electromagnetic characterization of these asymmetric borehole environments was not yet properly explored in the literature, and it is the primary motivation of this thesis. We will address the problem as a three-dimensional (3D), anisotropic, and lossy scatterer inside a cylindrically-layered medium, as illustrated in Figure 1.3.

Integral equation-based methods are widely used for modeling the scattering by arbitrarily shaped objects due to their flexibility in handling irregular objects [32 – 36]. Nevertheless, these methods require the computation and the inversion of a large complex matrix, whose computational cost can become prohibitive in multi-scale EM problems, as the ones discussed in this work. Instead of using traditional CEM techniques (based on finite elements, finite differences, finite volumes, or method of moments), we present an accurate and numerically efficient solution for the propagation problem at hand by using a perturbational solution. Our approach to calculating the sensor induced voltages consists of two steps; first, we solve the electromagnetic problem in the absence of the non-symmetric object by using the mode-matching-based method as proposed in [21, 24]. Then, we solve Fredholm's integral equation based on the Born approximation (BA) [37] to obtain the field perturbation due to the scatterer. We use a full-wave method based on the

mode-matching technique (MMT) as a basis for the BA developments. The perturbation method proposed in this thesis is flexible to model arbitrarily heterogeneous and anisotropic earth formations. It contributes to a relatively low-cost computational algorithm that accounts for the LWD tool response in complex geophysical environments. However, as in any perturbational theory, this approach has some limitations. The BA can accurately represent only the problems where the EM field variations inside the scatterer are small (compared to the background), and its dimensions are substantially smaller than the working wavelength [38 – 41]. Besides of that, remarkable results are possible in modeling LWD sensors operating below 2 MHz, as will be well detailed later in Chapter 3.

The BA requires the dyadic Green's functions of the background media for computing the perturbation field due to a scatterer, and obtaining them is not a trivial task in complex environments. For this reason, several works have addressed the problem by using the dyadics for homogeneous and isotropic background media [37, 39, 40, 42]. This strategy, however, has a dramatic cost: volumetric integrals should be computed throughout the whole problem domain (each vertical and radial layer in addition to the scatterer). For example, for modeling the hole bored into the ground depicted in Figure 1.2, assuming the background as the formation in 1, we require the following integrals: over a) the metallic cylindrical mandrel, b) the borehole, c) the soil 1, in addition to d) the invaded zone (soil 2). In the recent works in [28, 31], a similar procedure was employed, but, the dyadic Green's functions for the background were computed for planar stratified media. This allows a tremendous reduction in the computational cost required by the BA because the volumetric integrals should now only be calculated in the volume of the borehole and scatterer. In the proposed strategy, the dyadic Green's functions for the entire symmetric background (with planar and radial layers) are obtained. Consequently, one of the major contributions of our work towards the modeling of such kind of problem is that our BA approach requires only the computation of volumetric integrals over the scatterer zone.

Another topic addressed in this thesis is the modeling of the electromagnetic LWD sensor impedance. The analysis of the self-impedance of a realistic coil-antenna (i.e., a non-delta-type current source) was computed by using the full-wave MMT-based field solution combined with a variational method. To the best of our knowledge, the modeling of self-impedance of antenna sensors is a topic that was not adequately addressed in the literature because it demands high-cost by using traditional CEM methods. Our objective is to compute the input impedance for some classes of antennas used in practical LWD tools such

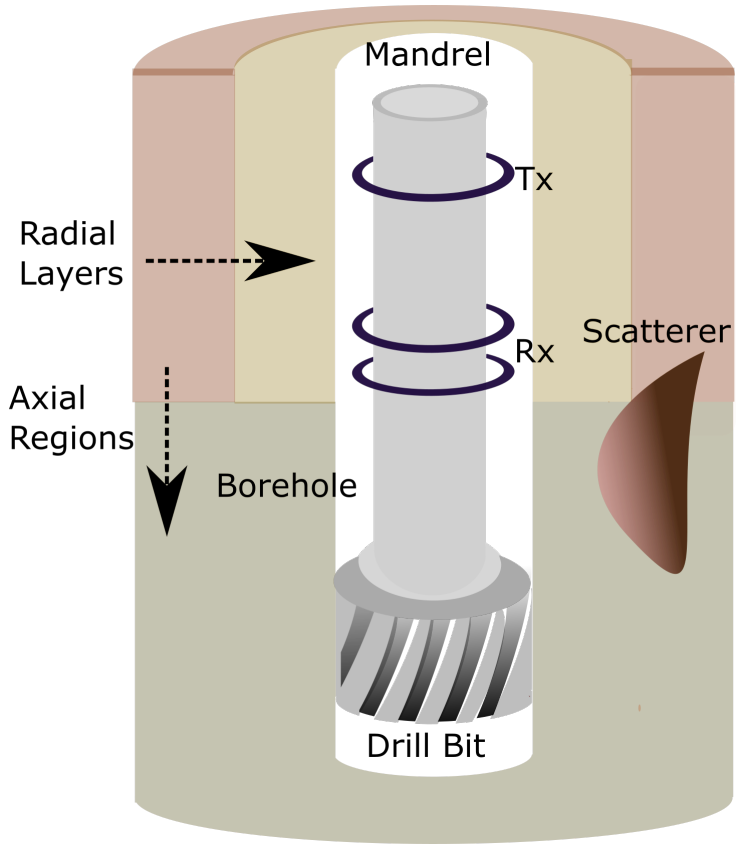

Figure 1.3: Geometry of a prospecting well drilled in a soil formation with a buried scatterer.

as those implemented by many oilfield contractors [9 – 12]. Several case studies are presented to validate the formulation mentioned above and to explore some antenna designs.

1.2 Major Research Contributions

The following topics of the research correspond to our original scientific contributions:

- The derivation of dyadic Green's functions for inhomogeneous cylindrically-layered media with both vertical and radial layers.
- The formulation and numerical implementation of a Born approximation (BA) for modeling the electromagnetic propagation in cylindrically-stratified formations (with vertical and radial layers) perturbed by three-dimensional anisotropic scatterers.
- The formulation of an extended version of the Born approximation (EBA) for modeling the electromagnetic propagation in cylindrically-stratified structures (with vertical and radial layers) perturbed by three-dimensional anisotropic scatterers.

– The formulation of electromagnetic scattering due to magnetodielectric objects with arbitrary anisotropy embedded in vertical and radial layered media in terms of BA and EBA.
– The computation of the LWD tool response with horizontal- and tilted-coil antennas traversing a non-uniform cross-section borehole.
– The formulation and numerical implementation of a variational mode-matching-based solution for computing the self-impedance of a realistic LWD tool immersed in a cylindrically-stratified soil formation.

1.3 Thesis Organization

The rest of this thesis is organized as follows. In Chapter 2, we review a semi-analytic formulation for analyzing the radiation due to LWD tools in anisotropic soil formations with both longitudinal and radial stratifications via a mode-matching-based technique. This approach employs an analytical eigenfield expansion that does not rely on a spatial discretization of the problem domain. The total field can be represented by a sum of a relatively small number of eigenmodes when compared to the number of grid points or discrete mesh required in other techniques, providing to this method the numerical efficiency demanded for the progress of real-time hydrocarbon exploitation.

In Chapter 3, we present a comprehensive mathematical formulation for modeling the electromagnetic propagation in cylindrically-stratified formations in the presence of 3D anisotropic scatterers. We have employed the field solutions obtained in Chapter 2 as a basis for representing the scattered fields, and we then derive a perturbation solution based on the Born approximation (BA) for the resulting Fredholm vector integral equation. We formulate two versions for perturbation corrections: one is based on the conventional BA, and the other is an extended version (EBA).

In Chapter 4, we present some relevant results obtained from our numerical implementation of the BA algorithm. Some case studies of LWD sensor responses were analyzed, including the effects of different kinds of scatterers, anisotropies, and antenna configurations.

In Chapter 5, we compare some aspects of BA and EBA for representing fields analysis inside the scatterer an in its vicinity.

In Chapter 6, we present a realistic model for the LWD sensor antennas. A detailed study was conducted to modeling the self- and mutual-impedance of finite-size coil antennas immersed in complex soil formations. We present results that demonstrate the ability of the techniques introduced in this thesis

for accurately to model electromagnetic logging sensors in a realistic way when it is compared with the Hertz-dipole-based model for TX and RX commonly found in the specialized literature. Most important: such results have shown that the computational effort required by our approach is relatively low if compared to other numerical techniques used as a reference.

Finally, in Chapter 7, we present the concluding remarks of this research and some suggestions for continued future works.

2
Electromagnetic Fields in Stratified Cylindrical Media

2.1
Introduction

Besides the earth soil being inherently an inhomogeneous environment, from a computational viewpoint, it is appropriated to model it as a *locally* stratified media by using a set of coupled layers (each one represented by a homogeneous, anisotropic, and lossy material), as illustrated in Figure 2.1. Due to the azimuthal symmetry of the well-logging tool that we want to describe (see Figure 1.2), the cylindrical coordinates system (ρ, ϕ, z) is a natural choice for the boundary condition enforcement. In this thesis, we assume (and subsequently we omit it) a time-harmonic dependence in the form $e^{-i\omega t}$, where ω is the angular frequency.

In this chapter, we review the semi-analytic method proposed in [5, 21] for solving the electromagnetic propagation in cylindrical-layered media. The formulation presented in this chapter is a fundamental base of the perturbational method for solving the propagation due to asymmetric scatterers. The chapter is organized as follows. In Section 2.2, we first solve the boundary problem of a radially-layered medium. Next, in Section 2.3, we use an axial mode-matching technique for solving the longitudinally-layered problem. We obtain a generalized scattering matrix (GSM) for describing each one of the vertical layers apart. The complete electromagnetic problem, including all vertical formations, can then be obtained by just properly combining the GSM matrices derived earlier. In sections 2.4 and 2.5, we describe the TX and RX by using a coil antenna model to approximate a real LWD sensor. Finally, in Section 2.6, we summarize the mathematical procedure reviewed herein and the associated numerical algorithm implementation.

2.2
Radial Layers

We first solve the propagation problem for radial layers; subsequently, we use these results to calculate the fields through vertical regions. An oil well cross-section can be represented by stratified media composed of N radial

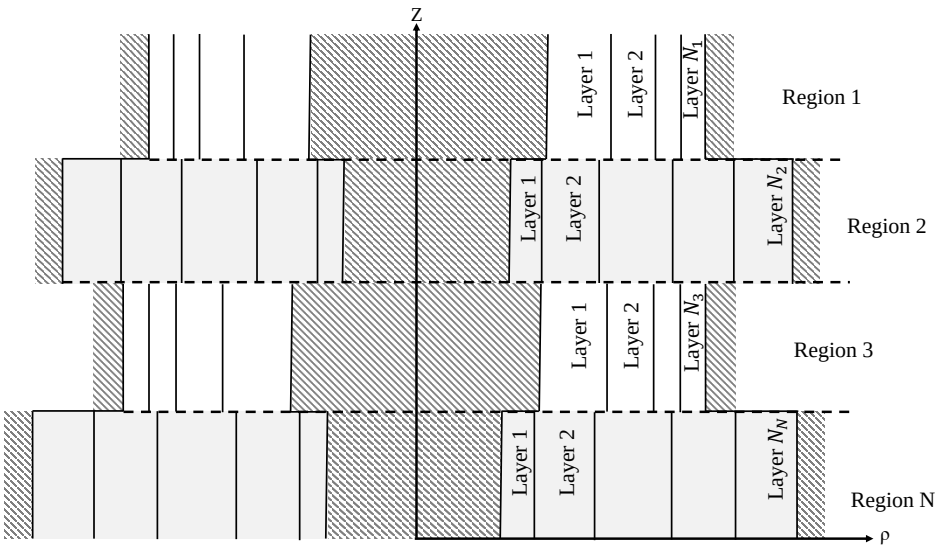

Figure 2.1: Stratified cylindrical structure composed by axial regions and radial layers.

layers, as illustrated in Figure 2.2. Each layer is located between $r_{j-1} < \rho < r_j$, with $j = \{1, 2, ...N\}$. Due to that, the analytic field solution for cylindrically stratified media is restricted to uni-axial materials. We characterize each layer by a uniaxial medium described by the complex-valued permittivity and permeability tensors:

$$\bar{\bar{\epsilon}}_j = \begin{bmatrix} \epsilon_{js} & 0 & 0 \\ 0 & \epsilon_{js} & 0 \\ 0 & 0 & \epsilon_{jz} \end{bmatrix}, \text{ with } \epsilon_{j\{s,z\}} = \epsilon_0 \epsilon_{jr\{s,z\}} + i\frac{\sigma_{j\{s,z\}}}{\omega}, \tag{2-1}$$

$$\bar{\bar{\mu}}_j = \begin{bmatrix} \mu_{js} & 0 & 0 \\ 0 & \mu_{js} & 0 \\ 0 & 0 & \mu_{jz} \end{bmatrix}, \text{ with } \mu_{j\{s,z\}} = \mu_0 \mu_{j\{s,z\}}, \tag{2-2}$$

where s represents the transverse components (ρ or ϕ), $\sigma_{j\{s,z\}}$ is the electrical conductivity and ϵ_0, μ_0 are the constitutive parameters for vacuum.

2.2.1 Electromagnetic Field Solutions

We calculate the electromagnetic fields for the proposed geometry by solving the Helmholtz equation in cylindrical coordinates by decomposing the fields in terms of transverse electric (TE^z) and magnetic (TM^z) to z contributions. Notice that this decomposition is useful for decoupling Maxwell's equations, but in general, we need hybrid modes (linear combination of TE^z and TM^z) for enforcing the boundary conditions. The solution of the associated

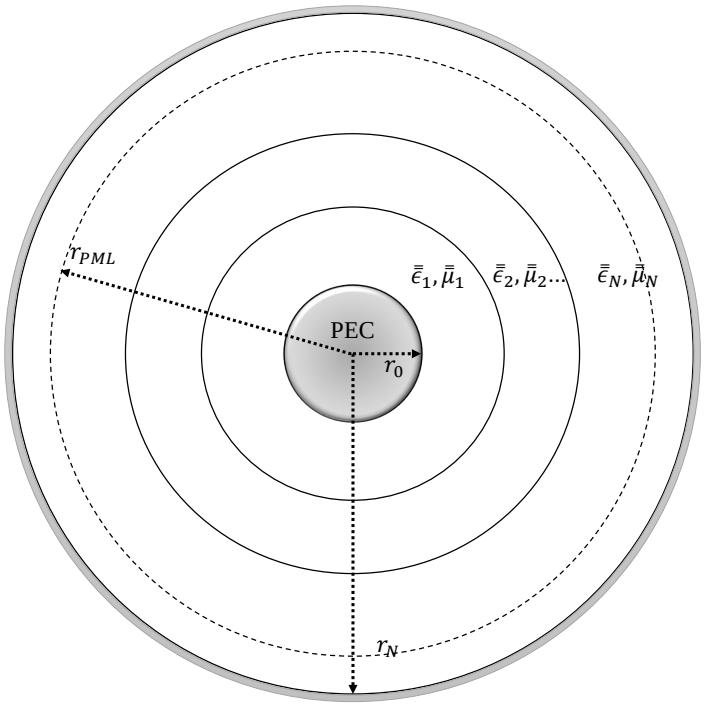

Figure 2.2: Radially-layered waveguide.

wave equation for fields parallel to $\hat{z}$ is given by [5, 21, 37, 43]

$$\psi = \sum_n \sum_{k_z} C_{n,k_z} R_n\left(\sqrt{\frac{p_z}{p_s}} k_\rho \, \rho\right) \Phi(n\phi) Z(k_z z), \tag{2-3}$$

where $\psi = \{E_z, H_z\}$, $p = \{\epsilon, \mu\}$, $R_n(\cdot)$ is a general solution for Bessel differential equation of integer order n, $\Phi(n\phi)$ and $Z(k_z z)$ are harmonic functions, k_z is the axial wavenumber, and k_ρ is the radial wavenumber that satisfies the dispersion relation

$$k_\rho^2 = k_s^2 - k_z^2, \quad \text{with} \quad k_s^2 = \omega^2 \mu_s \epsilon_s. \tag{2-4}$$

The summation in (2-3) is over all possible values (eigenvalues) of n and k_z. C_{n,k_z} is a source-dependent constant given by its source boundary condition. Once we determine the E_z and H_z, the fields components transversal to $\hat{z}$ can be obtained by using [37, p. 162], [5, Sec. 3.2.2]

$$\mathbf{E}_s = \frac{1}{k_\rho^2}[ik_z \boldsymbol{\nabla}_s E_z + i\omega\mu \boldsymbol{\nabla}_s \times (\hat{z} H_z)], \tag{2-5}$$

$$\mathbf{H}_s = \frac{1}{k_\rho^2}[ik_z \boldsymbol{\nabla}_s H_z - i\omega\epsilon \boldsymbol{\nabla}_s \times (\hat{z} E_z)], \tag{2-6}$$

where $\boldsymbol{\nabla}_s$ is the transverse (2D) nabla operator given by

$$\boldsymbol{\nabla}_s = \hat{\rho}\frac{\partial}{\partial \rho} + \hat{\phi}\frac{1}{\rho}\frac{\partial}{\partial \rho}. \tag{2-7}$$

We can represent the field components in (2-3), (2-5) and (2-6) for each layer j in a compact fashion [37, Ch. 3]:

$$\begin{bmatrix} E_{j\alpha} \\ H_{j\alpha} \end{bmatrix} = \sum_{n=-\infty}^{\infty} \sum_{p=1}^{\infty} \begin{bmatrix} e_{j\alpha,np}(\rho) \\ h_{j\alpha,np}(\rho) \end{bmatrix} e^{in\phi + ik_{z,np}z}, \quad \text{for} \quad \alpha = \{\rho, \phi, z\}, \tag{2-8}$$

where the index n refers to the azimuthal (ϕ) dependence of electromagnetic fields, while p refers to its radial (ρ) dependence. In addition, $e_{j\alpha,np}(\rho)$ and $h_{j\alpha,np}(\rho)$ are the ρ-dependent representation of the electric and magnetic fields given by a linear combination of cylindrical functions, i.e.,

$$\begin{bmatrix} e_{j\alpha,np}(\rho) \\ h_{j\alpha,np}(\rho) \end{bmatrix} = \bar{\bar{H}}_{zn}(k_{j\rho,np}\rho)\bar{a}_j + \bar{\bar{J}}_{zn}(k_{j\rho,np}\rho)\bar{b}_j, \tag{2-9}$$

where $\bar{a}_j$ and $\bar{b}_j$ are 2×1 column vectors of amplitudes determined from the boundary conditions, $\bar{a}_j$ represents TM modes while $\bar{b}_j$ TE modes, and they can be expressed as

$$\bar{a}_j = \begin{bmatrix} a^e_{j,np} \\ a^h_{j,np} \end{bmatrix}, \qquad \bar{b}_j = \begin{bmatrix} b^e_{j,np} \\ b^h_{j,np} \end{bmatrix}, \tag{2-10}$$

where the indexes e and h are used for electric and magnetic fields respectively, $k^{e,h}_{j\rho,np} = \alpha^{e,h}_j k_{j\rho,np}$, and $\alpha^{e,h}_j$ are anisotropic coefficients given by

$$\alpha^e_j = \sqrt{\frac{\epsilon_{jz}}{\epsilon_{js}}}, \qquad \alpha^h_j = \sqrt{\frac{\mu_{jz}}{\mu_{js}}}. \tag{2-11}$$

By enforcing the boundary conditions in each interface r_j, for each np-harmonic modal field, we can obtain the ρ-dependent fields in (2-9) as [5, 21, 37, 43]

$$\bar{g}_{j\alpha,np} = \left[\bar{\bar{H}}_{\alpha n}(k_{j\rho,np}\rho) + \bar{\bar{J}}_{\alpha n}(k_{j\rho,np}\rho)\tilde{\bar{\bar{R}}}^{(\rho)}_{j,j+1}\right]\bar{a}_j, \quad \text{or} \tag{2-12}$$

$$\bar{g}_{j\alpha,np} = \left[\bar{\bar{H}}_{\alpha n}(k_{j\rho,np}\rho)\tilde{\bar{\bar{R}}}^{(\rho)}_{j,j-1} + \bar{\bar{J}}_{\alpha n}(k_{j\rho,np}\rho)\right]\bar{b}_j, \tag{2-13}$$

where $\bar{g}_{j\alpha,np} = [e_{j\alpha,np}\ h_{j\alpha,np}]^t$ represents electromagnetic fields components in direction $\alpha = \{\rho, \phi, z\}$. In order to simplify the notation, in the next equations we will drop the modal subscript np, restoring it later if needed. Accordingly,

$\bar{\bar{H}}_{\alpha n}(k_{j\rho}\rho)$ and $\bar{\bar{J}}_{\alpha n}(k_{j\rho}\rho)$ become

$$\bar{\bar{G}}_{zn}(k_{j\rho}\rho) = \begin{bmatrix} G_n(k^e_{j\rho}\rho) & 0 \\ 0 & G_n(k^h_{j\rho}\rho) \end{bmatrix}, \tag{2-14}$$

$$\bar{\bar{G}}_{\phi n}(k_{j\rho}\,\rho) = \frac{1}{k^2_{j\rho}\rho} \begin{bmatrix} -n\,k_z\,G_n(k^e_{j\rho}\,\rho) & -i\omega\mu_{js}k^h_{j\rho}\rho G'_n(k^h_{j\rho}\rho) \\ i\omega\epsilon_{js}k^e_{j\rho}\rho G'_n(k^e_{j\rho}\rho) & -nk_zG_n(k^h_{j\rho}\rho) \end{bmatrix}, \tag{2-15}$$

$$\bar{\bar{G}}_{\rho n}(k_{j\rho}\rho) = \frac{1}{k^2_{j\rho}\rho} \begin{bmatrix} ik_zk^e_{j\rho}\rho G'_n(k^e_{j\rho}\rho) & -n\omega\mu_{js}G_n(k^h_{j\rho}\rho) \\ n\omega\epsilon_{js}G_n(k^e_{j\rho}\rho) & ik_zk^h_{j\rho}\rho G'_n(k^h_{j\rho}\rho) \end{bmatrix}. \tag{2-16}$$

In the above, the matrix $\bar{\bar{G}}_{\alpha n}(k_{j\rho}\rho)$ can be used for representing both $\bar{\bar{H}}_{\alpha n}(k_{j\rho}\rho)$ and $\bar{\bar{J}}_{\alpha n}(k_{j\rho}\rho)$. The Hankel function of first kind $H^{(1)}_n$ is represented when $\bar{\bar{G}}_{\alpha n}(k_{j\rho}\rho) = \bar{\bar{H}}_{\alpha n}(k_{j\rho}\rho)$. The Bessel function J_n is obtained when $\bar{\bar{G}}_{\alpha n}(k_{j\rho}\rho) = \bar{\bar{J}}_{\alpha n}(k_{j\rho}\rho)$. The prime ($'$) indicates the first derivative of the cylindrical functions with respect to the argument.

Returning to (2-12) and (2-13): the generalized reflection matrix $\tilde{\bar{\bar{R}}}^{(\rho)}_{j,j+1}$ is a 2×2 matrix given by [5, 37]:

$$\tilde{\bar{\bar{R}}}^{(\rho)}_{j,j\pm1} = \bar{\bar{R}}^{(\rho)}_{j,j\pm1} + \bar{\bar{T}}^{(\rho)}_{j\pm1,j}\tilde{\bar{\bar{R}}}^{(\rho)}_{j\pm1,j\pm2}\Big(\bar{\bar{I}} - \bar{\bar{R}}^{(\rho)}_{j\pm1,j}\tilde{\bar{\bar{R}}}^{(\rho)}_{j\pm1,j\pm2}\Big)^{-1}\bar{\bar{T}}^{(\rho)}_{j,j\pm1}, \tag{2-17}$$

where the tilde symbol is used for indicating *generalized* reflection and transmission matrices that take into account all the transmission and reflection effects emerging through N-layered boundary problem shown in Figure 2.2. The non-tilde matrices are *local* reflection and transmission matrices given by [5]

$$\bar{\bar{R}}^{(\rho)}_{j,j+1} = \bar{\bar{D}}^{-1}_{ja}\Big[\bar{\bar{H}}_{\phi j+1,j}\bar{\bar{H}}_{zj,j} - \bar{\bar{H}}_{\phi j+1,j}\bar{\bar{H}}_{zj+1,j}\bar{\bar{H}}^{-1}_{\phi j+1,j}\bar{\bar{H}}_{\phi j,j}\Big], \tag{2-18}$$

$$\bar{\bar{R}}^{(\rho)}_{j+1,j} = \bar{\bar{D}}^{-1}_{jb}\Big[\bar{\bar{J}}_{\phi j,j}\bar{\bar{J}}_{zj,j}\bar{\bar{J}}^{-1}_{\phi j,j}\bar{\bar{J}}_{\phi j+1,j} - \bar{\bar{J}}_{\phi j,j}\bar{\bar{J}}_{zj+1,j}\Big], \tag{2-19}$$

$$\bar{\bar{T}}^{(\rho)}_{j,j+1} = \bar{\bar{D}}^{-1}_{jb}\Big[\bar{\bar{J}}_{\phi j,j}\bar{\bar{H}}_{zj,j} - \bar{\bar{J}}_{\phi j,j}\bar{\bar{J}}_{zj,j}\bar{\bar{J}}^{-1}_{\phi j,j}\bar{\bar{H}}_{\phi j,j}\Big], \tag{2-20}$$

$$\bar{\bar{T}}^{(\rho)}_{j+1,j} = \bar{\bar{D}}^{-1}_{ja}\Big[\bar{\bar{H}}_{\phi j+1,j}\bar{\bar{H}}_{zj+1,j}\bar{\bar{H}}^{-1}_{\phi j+1,j}\bar{\bar{J}}_{\phi j+1,j} - \bar{\bar{H}}_{\phi j+1,j}\bar{\bar{J}}_{zj+1,j}\Big], \tag{2-21}$$

where $j = 1, 2, \ldots, N-1$, and

$$\bar{\bar{D}}_{ja} = \bar{\bar{H}}_{\phi j+1,j}\bar{\bar{H}}_{zj+1,j}\bar{\bar{H}}^{-1}_{\phi j+1,j}\bar{\bar{J}}^{-1}_{\phi j,j} - \bar{\bar{H}}_{\phi j+1,j}\bar{\bar{J}}_{zj,j}, \tag{2-22}$$

$$\bar{\bar{D}}_{jb} = \bar{\bar{J}}_{\phi j,j}\bar{\bar{H}}_{zj+1,j} - \bar{\bar{J}}_{\phi j,j}\bar{\bar{J}}_{zj,j}\bar{\bar{J}}^{-1}_{\phi j,j}\bar{\bar{H}}_{\phi j+1,j}. \tag{2-23}$$

In the above, we have used the shorthand notation

$$\bar{\bar{B}}_{\alpha i,j} = \bar{\bar{B}}_{\alpha,n}(k_{i\rho}r_j), \tag{2-24}$$

where $\bar{\bar{B}}_{\alpha,n} = \bar{\bar{H}}_{\alpha,n}$ or $\bar{\bar{J}}_{\alpha,n}$ with $\alpha = \{\phi, z\}$.

It should be observed that the superscript (ρ) used above in (2-17)–(2-21) is advisedly used to refer to radial discontinuities. This will avoid later confusions with other matrices associated with axial discontinuities.

2.2.2 Simulating the Unbounded Radial Domain

To mimic an unbounded media, we truncate the radial space by using an absorbing boundary layer. A perfectly matched layer (PML) is placed over $r_{\text{PML}} < \rho < r_N$ as illustrated in Figure 2.2. The PML allows us to absorb waves at the interface r_{PML} with zero reflection at all angles of incidence and for all frequencies [44, 45]. Although the interface r_{PML} is reflectionless, there is a reflection at r_N due to a perfect electric conductor (PEC) that is used for the radial domain truncation. Therefore, it is necessary to design the PML appropriately to avoid spurious reflections that affect the field's solutions.

There are different formulation for implementing a PML, one of the most common employs an artificial-anisotropic (biaxial) absorbing material [46] in $r_{\text{PML}} < \rho < r_N$. This formulation can be interpreted physically since we can imagine the anisotropic material coating the truncation layer. However, if we use this approach, we cannot use the formulation presented in Section 2.2.1 to calculate the modes introduced by the PML. We have assumed just uniaxial anisotropic layers for solving Maxwell's equations. In addition, it should be observed that the solution for Maxwell's equations in biaxial or totally anisotropic materials does not allow a conventional Helmholtz equation for E_z and H_z.

On the other hand, there is another PML formulation based on the complex-stretched coordinates [44, 47]. That is the mapping of the spatial coordinates into a complex domain. It ensures a smooth wave attenuation before the wave reaches r_N. By using this approach, the equations presented in Section 2.2 can be reused for calculating fields in both; the absorbing PML layer ($r_{\text{PML}} < \rho < r_N$), as well as in the non-absorbing regions ($r_0 < \rho < r_{\text{PML}}$). This formulation requires a mapping from the (real-valued) radial coordinate to a complex-valued coordinate inside the PML region. We can readily obtain a PML by employing $\rho \to \tilde{\rho}$ [5, 47], where

$$\tilde{\rho} = \int_0^{\rho} s_\rho(\rho')\, d\rho'. \tag{2-25}$$

The function $s_\rho(\rho')$ can be defined in the entire radial domain according to

$$s_\rho(\rho) = \begin{cases} 1, & \text{for } \rho < r_{\text{PML}} \\ 1 + i\,\alpha_{\text{PML}} \left(\frac{\rho - r_{\text{PML}}}{r_N - r_{\text{PML}}}\right)^q, & \text{for } r_{\text{PML}} \le \rho \le r_N, \end{cases} \tag{2-26}$$

by substituting (2-26) into (2-25), we obtain the mapping

$$\tilde{\rho} = \begin{cases} \rho, & \text{for } \rho < r_{\text{PML}} \\ \rho + i\,\alpha_{\text{PML}}\,\frac{(\rho - r_{\text{PML}})^{q+1}}{(q+1)(r_N - r_{\text{PML}})^q}, & \text{for } r_{\text{PML}} \leq \rho \leq r_N. \end{cases} \tag{2-27}$$

In short, the PML can be effectively implemented by choosing a complex-valued $r_N \to \tilde{r}_N = r'_N + ir''_N$ to mimic an unbounded medium. The real part, r'_N, must be large enough to allow the natural attenuation of evanescent modal fields that hit the end of the domain. The imaginary part, r''_N, must be properly selected to absorbs the radial-propagating fields. Further details can be found in [5, Ch. 2].

2.2.3 Characteristic Equation and the Guidance Condition

Returning to the ρ-dependent field vector in (2-12) and (2-13), we can obtain the following relations between $\bar{a}_j$ and $\bar{b}_j$:

$$\bar{a}_j = \bar{\bar{R}}^{(\rho)}_{j,j-1}\bar{b}_j, \tag{2-28}$$

$$\bar{b}_j = \bar{\bar{R}}^{(\rho)}_{j,j+1}\bar{a}_j. \tag{2-29}$$

By combining the above, we can easily obtain

$$\Big(\bar{\bar{I}} - \bar{\bar{R}}^{(\rho)}_{j,j+1}\bar{\bar{R}}^{(\rho)}_{j,j-1}\Big)\bar{b}_j = \bar{0}, \tag{2-30}$$

$$\Big(\bar{\bar{I}} - \bar{\bar{R}}^{(\rho)}_{j,j-1}\bar{\bar{R}}^{(\rho)}_{j,j+1}\Big)\bar{a}_j = \bar{0}. \tag{2-31}$$

These homogeneous matrix equations admit non-trivial solutions ($\bar{b}_j \neq \bar{0}$ and $\bar{a}_j \neq \bar{0}$) only if

$$\det\Big(\bar{\bar{I}} - \bar{\bar{R}}^{(\rho)}_{j,j-1}\bar{\bar{R}}^{(\rho)}_{j,j+1}\Big) = 0, \tag{2-32}$$

or

$$\det\Big(\bar{\bar{I}} - \bar{\bar{R}}^{(\rho)}_{j,j+1}\bar{\bar{R}}^{(\rho)}_{j,j-1}\Big) = 0. \tag{2-33}$$

By noting that $(\bar{\bar{I}} - \bar{\bar{R}}^{(\rho)}_{j,j-1}\bar{\bar{R}}^{(\rho)}_{j,j+1}) = (\bar{\bar{I}} - \bar{\bar{R}}^{(\rho)}_{j,j+1}\bar{\bar{R}}^{(\rho)}_{j,j-1})^t$, we can conclude that determinants in (2-32) and in (2-33) are equal. Also, since such relations hold for any $j = \{1, 2, \ldots, N\}$, for simplicity, we select $j = N$ and then we write the dispersion equation for the radially-layered problem as

$$f(k_z) = \det\Big(\bar{\bar{I}} - \bar{\bar{R}}^{(\rho)}_{N,N-1}\bar{\bar{R}}^{(\rho)}_{N,N+1}\Big) = 0, \tag{2-34}$$

the above equation must be solved numerically to determine the eigenvalues k_z that will contribute to our modal solution.

Since the media we are modeling are lossy, complex-valued k_z are supported and, before searching for the zeroes of (2-34), we need to determine

the number of eigenvalues that actually exists in a region of the complex plane. This problem will be solved by using the method proposed in [5, pp. 51–63], by rewriting the nonlinear characteristic equation in the simplified form $f(\gamma) = 0$. The Argument principle states that [48]

$$N_0 - N_p = \frac{1}{2\pi i} \oint_C \frac{f(\gamma)}{f'(\gamma)}\, d\gamma, \tag{2-35}$$

where N_0 is the number of zeros, and N_p is the number of poles inside the contour C. The integral over the contour is taken in counterclockwise sense, as shown in (2-35). Also, it was implicit assumed that function $f(\gamma)$ is holomorfic inside C, and there is no critical points (poles or zeroes) over C.

Since we are only interested in finding the number of eigensolution N_0 that dwell over C, in a second step we will remove the poles (that arise from the characteristic equation) by using a deflationary process. After some manipulations presented in [5], a pole-free characteristic equation can be obtained:

$$f_{pf}(k_z) = \prod_{j=1}^{N+1} \det\Big[(k_j^2 - k_z^2)^{m(j)/2} \bar{\bar{D}}_{j-1}\Big(\bar{\bar{I}} - \bar{\bar{R}}^{(\rho)}_{j-1,j} \bar{\bar{R}}^{(\rho)}_{j-1,j-2}\Big)\Big], \tag{2-36}$$

where $m(j)$ is the multiplicity of the critical point and it is given by:

$$m(j) = \begin{cases} \frac{3}{2} - \delta_{1,N}\Big[\frac{1}{2} + \delta\Big[\frac{1}{2} + \delta_{0,n}\Big] \\ -\delta_{0,r_0}\Big[\frac{1}{2} + n + \delta_{0,n}(1 - \delta_{1,N})\Big], & \text{if } j = 1, \\ \frac{3}{2}, & \text{if } j = N \text{ and } N > 1, \\ 0, & \text{if } j = N + 1, \\ 2, & \text{otherwise} \end{cases} \tag{2-37}$$

In the above, $\delta_{i,j}$ is the Kronecker delta defined as

$$\delta_{i,j} = \begin{cases} 1, & \text{for } i = j \\ 0, & \text{for } i \neq j \end{cases}. \tag{2-38}$$

With the pole-free characteristic equation (2-36), we can finally compute the number of eigensolutions inside contour C by using

$$N_0 = \frac{1}{2\pi i} \oint_C \frac{f_{pf}(k_z)}{f'_{pf}(k_z)}\, dk_z. \tag{2-39}$$

Now, the exact number of solutions was established in (2-39). Then, the desired zeroes of (2-36) readily computed by using a zero-finding technique, such as, the Newton-Raphson or the Muller method [49], [50, p. 466].

2.2.4 Modal Amplitudes

Based on the modal amplitude relations in (2-30) and (2-31), we can define the auxiliary matrix

$$\bar{\bar{M}}_N = \left(\bar{\bar{I}} - \bar{\bar{R}}^{(\rho)}_{N,N+1}\bar{\bar{R}}^{(\rho)}_{N,N-1}\right). \tag{2-40}$$

Once we solve the eigenvalues k_z, the matrix $\bar{\bar{M}}_N$ is determined and the modal field amplitudes can be found by solving the homogeneous linear system $\bar{\bar{M}}_N\,\bar{b}_N = \bar{0}$. The vector $\bar{b}_N$ is given by computing the null space of $\bar{\bar{M}}_N$. Since $\bar{\bar{M}}_N$ is a 2×2 matrix, we can decompose it as

$$\bar{\bar{M}}_N = \begin{bmatrix} m_{11} & m_{12} \\ m_{21} & m_{22} \end{bmatrix}. \tag{2-41}$$

For $\text{abs}\,(m_{11}) > \text{abs}\,(m_{22})$, we obtain

$$\bar{b}_N = \text{null}\,(\bar{\bar{M}}_N) = c \begin{bmatrix} -m_{12} \\ m_{11} \end{bmatrix}. \tag{2-42}$$

Otherwise, for $\text{abs}\,(m_{22}) > \text{abs}\,(m_{11})$, we get

$$\bar{b}_N = \text{null}\,(\bar{\bar{M}}_N) = c \begin{bmatrix} -m_{22} \\ m_{21} \end{bmatrix}, \tag{2-43}$$

where c is and arbitrary constant. Finally, the complete field solution can be computed by using (2-8), (2-12), and (2-13).

2.3 Axial Layers

We initially consider two semi-infinite waveguides, each one composing a given configuration of radial layers, that are coupled at the junction $z = z_1$. The geometry of this problem is illustrated in Figure 2.3. It is assumed that region 2 (characterized by the cross-section S_2) is wider than region 1 (described by S_1). The common coupling-aperture is denoted as S_a, while the non-coupled area $S_2 - S_1$ is denoted by S_w. In what follows, we will employ the modal fields derived up to now (the radially-layered solution) to describe the electromagnetic problem in regions 1 and 2. Then we will enforce the appropriated boundary conditions at junction $z = z_1$.

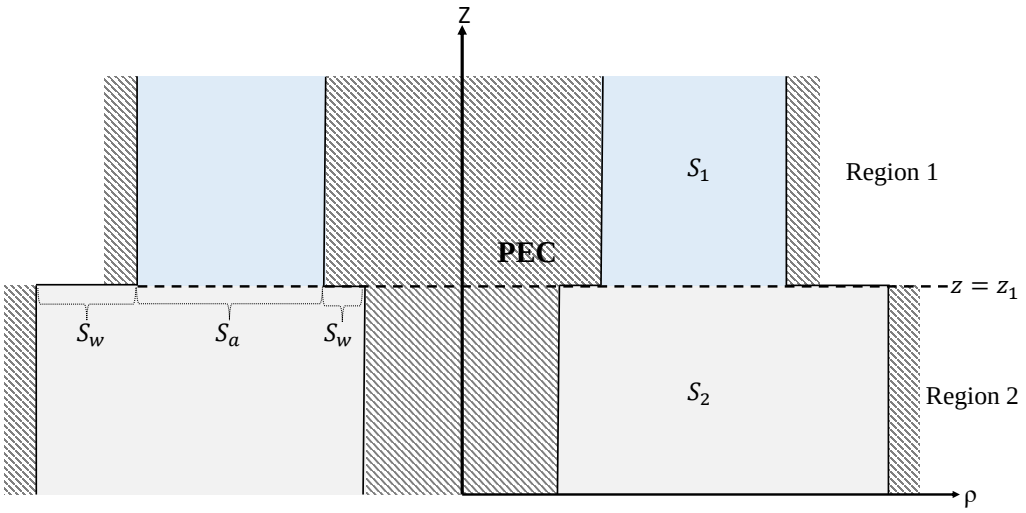

Figure 2.3: Junction between two semi-infinity waveguides. The hatched region is assume as a PEC.

2.3.1 Axial Mode-Matching

The electromagnetic field components transverse to $\hat{z}$ can be calculated in the region j by the modal expansion shown in (2-8), i.e.,

$$\mathbf{E}_{js} = \sum_{n=-\infty}^{\infty}\sum_{p=1}^{\infty}(a^{+}_{j,np}e^{ik_{z,np}z} + a^{-}_{j,np}e^{-ik_{z,np}z})\mathbf{e}_{js,np}(\rho)e^{in\phi}, \tag{2-44}$$

$$\mathbf{H}_{js} = \sum_{n'=-\infty}^{\infty}\sum_{p'=1}^{\infty}(a^{+}_{j,n'p'}e^{ik_{z,n'p'}z} - a^{-}_{j,n'p'}e^{-ik_{z,n'p'}z})\mathbf{h}_{js,n'p'}(\rho)e^{in'\phi}. \tag{2-45}$$

To simplify the notation, we will express the double sum in above as a single one. Then, we can write

$$\mathbf{E}_{js} = \sum_{m}^{\infty}(A^{+}_{j,m} + A^{-}_{j,m})\mathbf{E}_{js,m}, \tag{2-46}$$

$$\mathbf{H}_{js} = \sum_{m'}^{\infty}(A^{+}_{j,m'} - A^{-}_{j,m'})\mathbf{H}_{js,m'}, \tag{2-47}$$

where $j = \{1, 2\}$, $A^{\pm}_{j,m} = a^{\pm}_{j,m}e^{\pm ik_{z,m}z_1}$ are the forward/backward modal amplitudes at the junction $z = z_1$ for the mth modal field. Assuming these series are convergent, we can truncate the expansion with M modes in region 1 and N modes in region 2. By enforcing the continuity of the electric fields at the junction $z = z_1$, we obtain

$$\sum_{n=1}^{N}(A^{+}_{2,n} + A^{-}_{2,n})\mathbf{E}_{2s,n} = \sum_{m=1}^{M}(A^{+}_{1,m} + A^{-}_{1,m})\mathbf{E}_{1s,m}, \quad \text{inside } S_a, \tag{2-48}$$

$$\sum_{n=1}^{N}(A_{2,n}^{+}+A_{2,n}^{-})\mathbf{E}_{2s,n}=\mathbf{0},\quad \text{inside } S_w. \tag{2-49}$$

Multiplying (2-48) and (2-49) by $\mathbf{H}_{js,n'}$, with $n'=\{1,2,\ldots,N\}$, and integrating the result over the cross-section S_2, the projection over $\hat{z}$ will result in a set of N continuity equations that can be written in a matrix form as

$$\bar{\bar{Q}}_2(\bar{A}_2^{+}+\bar{A}_2^{-})=\bar{\bar{X}}_{12}(\bar{A}_1^{+}+\bar{A}_1^{-}), \tag{2-50}$$

where

$$\bar{\bar{X}}_{12}|_{n,m}=X_{1m,2n}, \tag{2-51}$$

$$\bar{\bar{Q}}_2|_{n,m}=X_{2m,2n}. \tag{2-52}$$

These matrices are filled with reaction integrals [51, 52] that couple regions 1 and 2. Using the generalize notation introduced in [5, p. 67], the reaction of the mth field in region i with respect to the nth field in region j is given by

$$X_{im,jn}=\langle\mathbf{E}_{is,m},\mathbf{H}_{js,n}\rangle \tag{2-53}$$

$$=\iint_{S_i}(\mathbf{E}_{is,m}\times\mathbf{H}_{js,n})\cdot\hat{z}\,\rho\,d\rho\,d\phi. \tag{2-54}$$

Similarly, for the continuity of the magnetic field at $z=z_1$, we can obtain

$$\bar{\bar{X}}_{12}^{t}\,(\bar{A}_2^{+}-\bar{A}_2^{-})=\bar{\bar{Q}}_1(\bar{A}_1^{+}-\bar{A}_1^{-}), \tag{2-55}$$

where

$$\bar{\bar{Q}}_1|_{n,m}=X_{1m,1n}. \tag{2-56}$$

With the aid of (2-50) and (2-55), we can relate the modal field amplitudes at the junction $z=z_1$ by using a generalized scattering matrix (GSM). Accordingly,

$$\begin{bmatrix}\bar{A}_1^{-}\\ \bar{A}_2^{+}\end{bmatrix}=\begin{bmatrix}\bar{\bar{R}}_{12}^{(z)} & \bar{\bar{T}}_{21}^{(z)}\\ \bar{\bar{T}}_{12}^{(z)} & \bar{\bar{R}}_{21}^{(z)}\end{bmatrix}\begin{bmatrix}\bar{A}_1^{+}\\ \bar{A}_2^{-}\end{bmatrix}, \tag{2-57}$$

where the scattering matrices are

$$\bar{\bar{R}}_{12}^{(z)}=\Big[\bar{\bar{Q}}_1+\bar{\bar{X}}_{12}^{t}\Big(\bar{\bar{Q}}_2\Big)^{-1}\bar{\bar{X}}_{12}\Big]^{-1}\Big[\bar{\bar{Q}}_1-\bar{\bar{X}}_{12}^{t}\Big(\bar{\bar{Q}}_2\Big)^{-1}\bar{\bar{X}}_{12}\Big], \tag{2-58}$$

$$\bar{\bar{T}}_{21}^{(z)}=2\Big[\bar{\bar{Q}}_1+\bar{\bar{X}}_{12}^{t}\Big(\bar{\bar{Q}}_2\Big)^{-1}\bar{\bar{X}}_{12}\Big]^{-1}\bar{\bar{X}}_{12}^{t}, \tag{2-59}$$

$$\bar{\bar{T}}_{12}^{(z)}=2\Big[\bar{\bar{Q}}_2+\bar{\bar{X}}_{12}\Big(\bar{\bar{Q}}_1\Big)^{-1}\bar{\bar{X}}_{12}^{t}\Big]^{-1}\bar{\bar{X}}_{12}, \tag{2-60}$$

$$\bar{\bar{R}}_{21}^{(z)}=-\Big[\bar{\bar{Q}}_2+\bar{\bar{X}}_{12}\Big(\bar{\bar{Q}}_1\Big)^{-1}\bar{\bar{X}}_{12}^{t}\Big]^{-1}\Big[\bar{\bar{Q}}_2-\bar{\bar{X}}_{12}\bar{\bar{Q}}_1^{-1}\bar{\bar{X}}_{12}^{t}\Big]. \tag{2-61}$$

2.3.2 Reaction Integrals

By using the azimuthal orthogonality over ϕ, the reaction of the (np)th modal field in region i with the (n',p')th modal field in region j is given by

$$X_{i(np),j(n',p')} = -\delta_{n,n'}\, 2\pi(-1)^n \int_{\rho_i} (s_n\, e_{i\rho,np}\, h_{j\phi,np'} + e_{i\phi,np}\, h_{j\rho,np'})\, \rho\, d\rho, \quad (2\text{-}62)$$

where $s_n = 1 - \delta_{0,n}$, the Kronecker delta is defined as $\delta_{n,n'} = 1$ for $n = n'$, and zero otherwise. A special case is obtained when $i = j$, and it corresponds to the self-reaction

$$X_{j(np),j(n',p')} = -\delta_{n,n'}\, \delta_{p,p'}\, 2\pi(-1)^n \int_{\rho_j} (s_n\, e_{j\rho,np}\, h_{j\phi,np'} + e_{j\phi,np}\, h_{j\rho,np'})\, \rho\, d\rho. \quad (2\text{-}63)$$

Taking advantage of azimuthal orthogonality, we can solve the GSM matrix (2-57) for each azimuthal index n independently. The fields components required in the reaction integrals (2-62) and (2-63) are given by

$$e_{1\rho} = \frac{1}{k_{1\rho}^2 \rho}(ik_{1z}\, \alpha_1^e\, k_{1\rho}\, \rho B_n'^{e1} - n\omega\mu_{1s} B_n^{h1}), \quad (2\text{-}64)$$

$$h_{2\phi} = \frac{1}{k_{2\rho}^2 \rho}(i\omega\, \epsilon_{2s}\, \alpha_2^e\, k_{2\rho}\, \rho B_n'^{e2} - nk_{2z} B_n^{h2}), \quad (2\text{-}65)$$

$$e_{1\phi} = \frac{1}{k_{1\rho}^2 \rho}(-nk_{1z} B_n^{e1} - i\omega\, \mu_{1s}\, \alpha_1^h\, k_{1\rho}\, \rho B_n'^{h1}), \quad (2\text{-}66)$$

$$h_{2\rho} = \frac{1}{k_{2\rho}^2 \rho}(n\omega\, \epsilon_{2s}\, B_n^{e2} + ik_{2z}\, \alpha_s^h\, k_{2\rho}\, \rho B_n'^{h2}), \quad (2\text{-}67)$$

where $B_n^{\{e,h\}j}$ is the rho-dependent parcel of the axial fields:

$$B_n^{ej} = B_n^{ej}(\alpha^e k_{j\rho}\rho) = e_{jz}(\rho), \quad (2\text{-}68)$$

$$B_n^{hj} = B_n^{hj}(\alpha^h k_{j\rho}\rho) = h_{jz}(\rho). \quad (2\text{-}69)$$

Substituting (2-64)-(2-67) in (2-62) we obtain

$$\begin{aligned} X_{1,2} \;=\; & -2\pi(-1)^n \int_{\rho_1} \frac{1}{k_{1\rho}^2 k_{2\rho}^2 \rho^2} \\ & \times \Big\{ -\omega\epsilon_{2s}\, k_{1z}\, (s_n\, \alpha_1^e\, k_{1\rho}\, \rho\, B_n'^{e1}\, \alpha_2^e\, k_{2\rho}\, \rho\, B_n'^{e2} + n^2 B_n^{e1} B_n^{e2}) \\ & +\; \omega\mu_{1s}\, k_{2z}\, (\alpha_1^h\, k_{1\rho}\, \rho\, B_n'^{h1}\, \alpha_2^h\, k_{2\rho}\, \rho\, B_n'^{h2} + n^2 B_n^{h1} B_n^{h2}) \\ & -\; ik_{1z}\, k_{2z}\, n\, (\alpha_1^e\, k_{1\rho}\, \rho\, B_n'^{e1} B_n^{h2} + B_n^{e1}\, \alpha_2^h\, k_{2\rho}\, \rho\, B_n'^{h2}) \\ & -\; i\omega^2\mu_{1s}\, \epsilon_{2s} n (B_n^{h1} \alpha_2^e\, k_{2\rho}\, \rho\, B_n'^{e2} + \alpha_1^h\, k_{1\rho}\, \rho\, B_n'^{h1} B_n^{e2}) \Big\} \rho\, d\rho. \end{aligned} \quad (2\text{-}70)$$

The following cylindrical functions identities will be used to simplify the

expression (2-70):

$$x\,C_n'(x)\,y\,D_n'(y) + n^2 C_n(x) D_n(y) = \frac{xy}{2}\Big[C_{n-1}(x)D_{n-1}(y) + C_{n+1}(x)D_{n+1}(y)\Big], \tag{2-71}$$

$$x\,C_n'(x) D_n(y) + C_n(x)\,y\,D_n'(y) = \frac{xy}{2n}\Big[C_{n-1}(x)D_{n-1}(y) - C_{n+1}(x)D_{n+1}(y)\Big], \tag{2-72}$$

where $C_n(x)$ and $D_n(y)$ are cylindrical functions. Equation (2-70) can now be reduced to

$$X_{1,2} = -\frac{(-1)^n \pi}{k_{1\rho} k_{2\rho}} \Bigg\{ -s_n \omega \epsilon_{2s} k_{1z} \alpha_1^e \alpha_2^e \mathfrak{L}_n^+\Big(B_n^{e1}, B_n^{e2}\Big) + \omega \mu_{1s} k_{2z} \alpha_1^h \alpha_2^h \mathfrak{L}_n^+\Big(B_n^{h1}, B_n^{h2}\Big) - i k_{1z} k_{2z} \alpha_1^e \alpha_2^h \mathfrak{L}_n^-\Big(B_n^{e1}, B_n^{h2}\Big) - i\omega^2 \epsilon_{2s} \mu_{1s} \alpha_2^e \alpha_1^h \mathfrak{L}_n^-\Big(B_n^{h1}, B_n^{e2}\Big) \Bigg\}, \tag{2-73}$$

for $n \geq 0$, and where the integrals $\mathfrak{L}_n^{\pm}(C_n, D_n)$ are

$$\mathfrak{L}_n^{\pm}(C_n, D_n) = \mathfrak{L}_{n-1}(C_{n-1}, D_{n-1}) \pm \mathfrak{L}_{n+1}(C_{n+1}, D_{n+1}), \tag{2-74}$$

where Lommel integral is given by

$$\mathfrak{L}_m(B_m^1, B_m^2) = \int_{\rho_{\min}}^{\rho_{\max}} B_m^1(\alpha_1 k_{1\rho}\rho) B_m^2(\alpha_2 k_{2\rho}\rho) \rho\, d\rho, \tag{2-75}$$

which is an analytical integral, and closed-form solutions are available in [5,53].

We can generalize (2-62) for matching waveguides with arbitrary number of radial layers, as illustrated in Figure 2.4. We define two sets of radii that describe the radial layers in regions 1 and 2 as:

$$r_1 = \{r_{1,0}, r_{1,1}, r_{1,2}, ...r_{1,N_1}\}, \tag{2-76}$$

$$r_2 = \{r_{2,0}, r_{2,1}, r_{2,2}, ...r_{2,N_2}\}. \tag{2-77}$$

Then, the radii are intercepted and sorted for creating the vector $r_a = \text{sort}\,(r_1 \cup r_{12})$. As result, the reaction integral (2-62) between two generic radially-stratified waveguides can be calculated via

$$X_{1(np),2(-np')} = -2\pi(-1)^n \times \sum_{j=0}^{\dim(r_a)} \int_{r_{a,j}}^{r_{a,j+1}} \left[s_n\, e_{1\rho,np}(\rho)\, h_{2\phi,np'}(\rho) + e_{1\phi,np}(\rho)\, h_{2\rho,np'}(\rho)\right] \rho\, d\rho, \tag{2-78}$$

a particular case, the self-reaction, is given by

$$Q_{i,np} = -2\pi(-1)^n \sum_{j=0}^{\dim(r_i)} \int_{r_{i,j}}^{r_{i,j+1}} \left[s_n\, e_{i\rho,np}(\rho)\, h_{i\phi,np}(\rho) + e_{i\phi,np}(\rho)\, h_{i\rho,np}(\rho)\right] \rho\, d\rho. \tag{2-79}$$

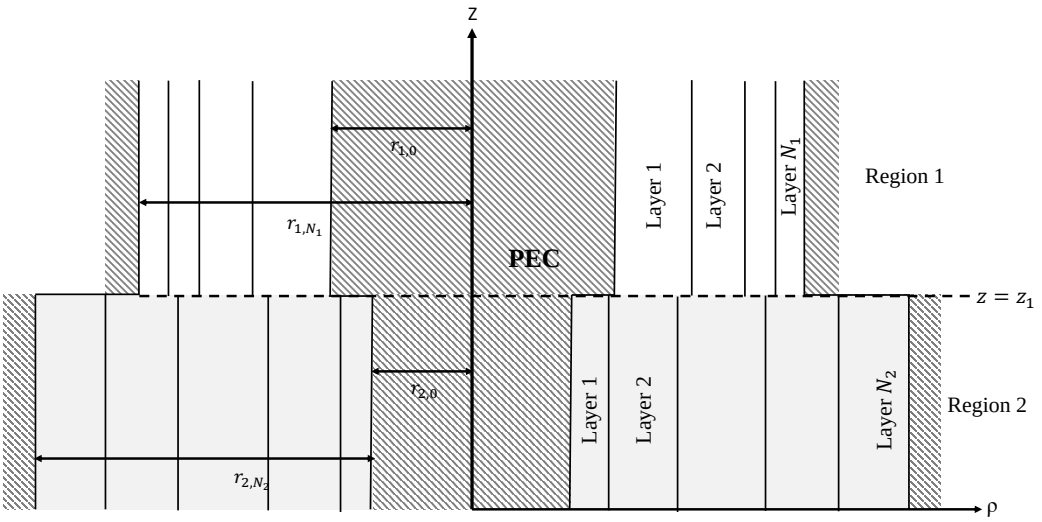

Figure 2.4: Junction between two semi-infinitely-long and radially-stratified waveguides.

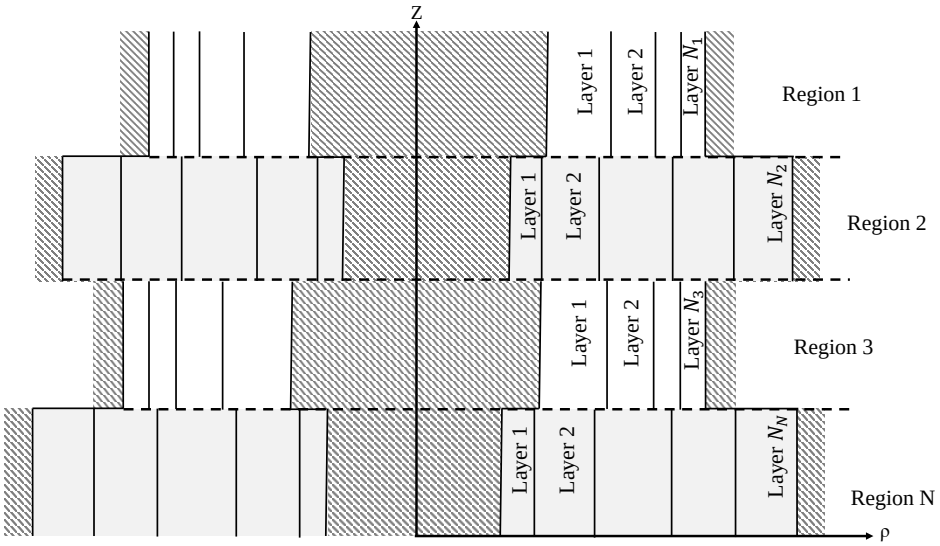

Figure 2.5: Generalized stratified cylindrical structure composed by N axial regions. Each one composed of an arbitrary number of radial layers.

2.3.3 Fields at an Arbitrary Observation Point

If our problem is composed by several axial regions as illustrated in Figure 2.5, we should calculate the modal forward/backward amplitudes by using (2-57) in each vertical junction. Then, we need to transmit these amplitudes between the source (TX) and the observation point (RX). Supposing the RX is placed in layer m at a position $\mathbf{r}$, while the TX is in layer $\tilde{n}$ at $\mathbf{r}_0$, the modal amplitudes at the receiver point are given by

$$\bar{A}_r^{\pm} = \bar{\bar{P}}_{\tilde{n}}^{\pm}(z_{\tilde{n}}^{\mp}, z_r)\bar{\bar{T}}_{m\tilde{n}}\bar{\bar{M}}_m^{\pm}(z_m^{\pm})[\bar{\bar{P}}_m^{\pm}(z_0, z_m^{\pm})\bar{A}_{r_0}^{\pm} + \bar{\bar{U}}_m^{\mp}(z_0, z_m^{\pm})\bar{A}_{r_0}^{\mp}], \tag{2-80}$$

for $m < \tilde{n}$

$$\bar{A}_r^{\mp} = \bar{\bar{U}}_{\tilde{n}}^{\pm}(z_n^{\mp}, z_r)\bar{\bar{T}}_{m\tilde{n}}\bar{\bar{M}}_m^{\pm}(z_m^{\pm})[\bar{\bar{P}}_m^{\pm}(z_0, z_m^{\pm})\bar{A}_{r_0}^{\pm} + \bar{\bar{U}}_m^{\mp}(z_0, z_m^{\pm})\bar{A}_{r_0}^{\mp}], \tag{2-81}$$

for $m > \tilde{n}$

$$\bar{A}_r^{\pm} = \bar{\bar{M}}_m^{\pm}(z_r)[\bar{\bar{P}}_m^{\pm}(z_0, z_r)\bar{A}_{r_0}^{\pm} + \bar{\bar{U}}_m^{\mp}(z_0, z_r)\bar{A}_{r_0}^{\mp}], \tag{2-82}$$

for $m = \tilde{n}$, and $z_0 < z_r$

$$\bar{A}_r^{\mp} = \bar{\bar{M}}_m^{\mp}(z_r)[\bar{\bar{U}}_m^{\pm}(z_0, z_r)\bar{A}_{r_0}^{\pm} + \bar{\bar{D}}_m^{\mp}(z_0, z_r)\bar{A}_{r_0}^{\mp}], \tag{2-83}$$

for $m = \tilde{n}$, and $z_0 > z_r$. We have that $z_j^+ = z_j$ and $z_j^- = z_{j-1}$.

The matrices presented in (2-80)-(2-83) are given by

$$\bar{\bar{M}}_m^{\pm} = \left(\bar{\bar{I}} - \bar{\bar{R}}_{m,m\mp1}\bar{\bar{P}}_m\bar{\bar{R}}_{m,m\pm1}\bar{\bar{P}}_m\right)^{-1}, \tag{2-84}$$

$$\bar{\bar{P}}_m = \bar{\bar{P}}_m^+(z_{m-1}, z_m) = \bar{\bar{P}}_m^-(z_m, z_{m-1}), \tag{2-85}$$

$$\bar{\bar{P}}_j^{\pm}(z', z)|_{pp} = e^{\pm ik_{pz}(z-z')}, \text{by using the axial wavenumber in region } m \tag{2-86}$$

$$\bar{\bar{T}}_{m,\tilde{n}} = \left(\prod_{j=\mp\tilde{n}}^{m\pm2}\bar{\bar{T}}_{\mp j\mp1,\mp j}\bar{\bar{P}}_{\mp j\mp1}\right)\bar{\bar{T}}_{m,m\pm1}, \tag{2-87}$$

$$\bar{\bar{T}}_{j,j-1} = \bar{\bar{M}}_{j-1}^-(z_J^-)\bar{\bar{T}}_{j,j-1} \tag{2-88}$$

$$\bar{\bar{U}}_j^-(z', z) = \bar{\bar{P}}_j^+(z_{j-1}, z)\bar{\bar{R}}_{j,j-1}\bar{\bar{P}}_j^-(z', z_{j-1}), \tag{2-89}$$

$$\bar{\bar{U}}_j^+(z', z) = \bar{\bar{P}}_j^-(z_j, z)\bar{\bar{R}}_{j,j+1}\bar{\bar{P}}_j^+(z', z_j), \tag{2-90}$$

$$\bar{\bar{D}}_j^-(z', z) = \bar{\bar{P}}_j^-(z_j^+, z)\bar{\bar{R}}_{j,j+1}\bar{\bar{P}}_j^+(z_j^-, z_j^+)\bar{\bar{R}}_{j,j-1}\bar{\bar{P}}_j^-(z', z_j^-), \tag{2-91}$$

$$\bar{\bar{D}}_j^+(z', z) = \bar{\bar{P}}_j^+(z_j^-, z)\bar{\bar{R}}_{j,j-1}\bar{\bar{P}}_j^-(z_j^+, z_j^-)\bar{\bar{R}}_{j,j+1}\bar{\bar{P}}_j^+(z', z_j^+). \tag{2-92}$$

$$\bar{\bar{R}}_{j,j+1} = \bar{\bar{R}}_{j,j+1} + \bar{\bar{T}}_{j+1,j}\bar{\bar{P}}_{j+1}\bar{\bar{R}}_{j+1,j+2}\bar{\bar{P}}_{j+1}\bar{\bar{M}}_{j+1}^+(z_n^+)\bar{\bar{T}}_{j,j+1}. \tag{2-93}$$

Further details on the above formulation can be found in [5, App. B]. Finally, the complete solution for electromagnetic fields at an arbitrary point are given by

$$\mathbf{E}_s(\rho, \phi, z_r) = \sum_n\sum_p(A_{r,np}^+ + A_{r,np}^-)\mathbf{e}_{s,np}(\rho)e^{in\phi}, \tag{2-94}$$

$$E_z(\rho, \phi, z_r) = \sum_n\sum_p(A_{r,np}^+ - A_{r,np}^-)e_{z,np}(\rho)e^{in\phi}, \tag{2-95}$$

$$\mathbf{H}_s(\rho, \phi, z_r) = \sum_n\sum_p(A_{r,np}^+ - A_{r,np}^-)\mathbf{h}_{s,np}(\rho)e^{in\phi}, \tag{2-96}$$

$$H_z(\rho, \phi, z_r) = \sum_n\sum_p(A_{r,np}^+ + A_{r,np}^-)h_{z,np}(\rho)e^{in\phi}. \tag{2-97}$$

2.4 Electromagnetic Sources

The forward and backward fields radiated by a generic source can be expanded in terms of the sum of eigenfields that we derived earlier in this chapter, namely,

$$\mathbf{E}^{\pm} = \sum_{n=-\infty}^{\infty} \sum_{p=1}^{\infty} A_{np}^{\pm} \left[\mathbf{e}_{\mathbf{s},np}^{\pm}(\rho) \pm \hat{z} e_{z,np}(\rho) \right] e^{\pm i k_{z,np}(z-z_T)+in\phi}, \tag{2-98}$$

$$\mathbf{H}^{\pm} = \sum_{n=-\infty}^{\infty} \sum_{p=1}^{\infty} A_{np}^{\pm} \left[\mathbf{h}_{\mathbf{s},np}^{\pm}(\rho) \pm \hat{z} h_{z,np}(\rho) \right] e^{\pm i k_{z,np}(z-z_T)+in\phi}, \tag{2-99}$$

for $z \gtrless z_T^{\pm}$. The source amplitudes $A_{np}^{\pm}$ can be calculated by employing the Lorentz reciprocity theorem [51, 54]. The complete process for computing the amplitudes is presented in [5, Sec. 3.5], the final expressions are showed bellow:

$$A_{np}^{\pm} = \frac{\hat{S}_{np}^{\pm}}{\hat{N}_{np}}, \tag{2-100}$$

$$\hat{S}_{np}^{\pm} = (-1)^n S_{np}^{\pm}, \tag{2-101}$$

$$\hat{N}_{np} = (-1)^n N_{np}, \tag{2-102}$$

$$\begin{aligned} S_{np}^{\pm} = (-1)^n \int_V \Big[& (-s_n e_{\rho,np}\,\hat{\rho} + e_{\phi,np}\hat{\phi} \pm s_n e_{z,np}\hat{z}) \cdot \mathbf{J} \\ & \pm (h_{\rho,np}\,\hat{\rho} - s_n h_{\phi,np}\hat{\phi} \mp h_{z,np}\hat{z}) \cdot \mathbf{M} \Big] e^{-in\phi} e^{\mp i k_{z,np} z}\, dv, \end{aligned} \tag{2-103}$$

$$N_{np} = 4\pi(-1)^n \int (S_n e_{\rho,np} h_{\phi,np} + e_{\phi,np} h_{\phi,np})\, \rho\, d\rho \tag{2-104}$$

$$= -2\, Q_{np}, \tag{2-105}$$

where Q_{np} is the self-reaction given by (2-79).

In the following, we obtain the source modal amplitudes $A_{np}^{\pm}$ for modeling coils, the type of antenna typically used in well-logging sensing.

2.4.1 Tilted-Coil Antenna

A tilted-coil antenna offers directional sensitivity provided by azimuthal information. Tilted-coil antenna excites and receives hybrid modes, that is, the electromagnetic fields have the three components (ρ, ϕ, z) [25]. Consider a tilted-coil antenna source with coordinates

$$\mathbf{r}_T = \hat{\rho}\,\rho_T + \hat{z}[z_T - \rho_T \tan\theta_T \cos(\phi - \phi_T)], \tag{2-106}$$

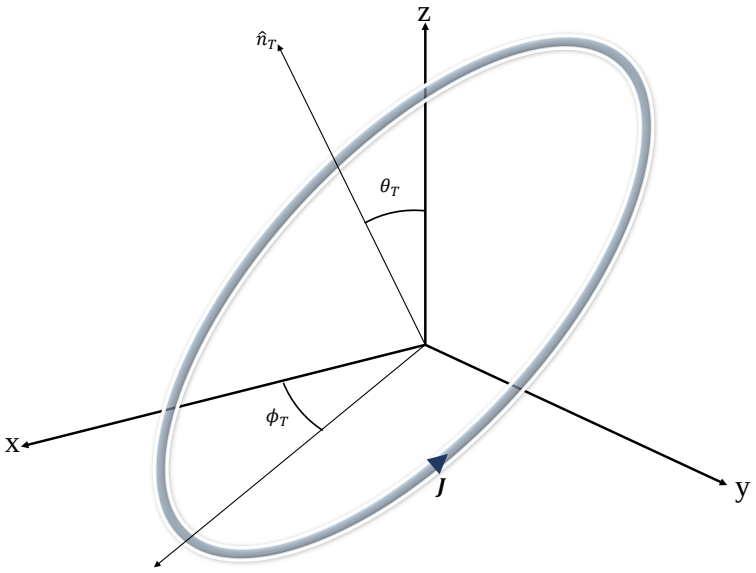

Figure 2.6: Geometry of a tilted-coil antenna.

where ρ_T is the coil radius, z_T is the axial position at the coil center, and ϕ_T and θ_T are the azimuthal and elevation tilt angles, as illustrated in Figure 2.6. The coil is carrying an electrical current I_T, and its associated electrical density is given by

$$\mathbf{J} = I_T\, \boldsymbol{\delta}_T, \tag{2-107}$$

where

$$\boldsymbol{\delta}_T = \delta(\rho - \rho_T)\delta(z - z_T + \rho_T \tan\theta_T \cos(\phi - \phi_T))(\hat{\phi} + \hat{z}\tan\theta_T \sin(\phi - \phi_T)). \tag{2-108}$$

Substituting (2-107) in (2-103) we get that, for a tilted-coil antenna, the parameter $S_{np}^{\pm}$ is given by

$$\begin{aligned} S_{np}^{\pm} =& (-1)^n I_T \rho_T e^{\mp i k_{z,np} z_T} \int_{-\pi}^{\pi} \left[e_{\phi,np}(\rho_T) \pm s_n e_{z,np}(\rho_T) \tan\theta_T \sin(\phi - \phi_T) \right] \\ & \times e^{-in\phi} e^{\pm i k_{z,np} \rho_T \tan\theta_T \cos(\phi - \phi_T)}\, d\phi, \end{aligned} \tag{2-109}$$

the solution for the integral over ϕ is known, and we can obtain

$$S_{np}^{\pm} = (-1)^n I_T \rho_T 2\pi i^n J_n(\pm\kappa_T) \left[e_{\phi,np}(\rho_T) - \frac{n}{k_{z,np}\rho_T} e_{z,np}(\rho_T) \right] e^{-in\phi_T} e^{\mp i k_{z,np} z_T}, \tag{2-110}$$

where

$$\kappa_T = k_{z,np}\rho_T \tan\theta_T. \tag{2-111}$$

2.5 Induced Voltage at the Receiver Antennas

The induced voltage at a tilted-coil antenna can be calculated by

$$V_{RX} = -\int_V (\mathbf{E}^+ + \mathbf{E}^-) \cdot \boldsymbol{\delta}_R \, dv, \tag{2-112}$$

with help of the field expressions (2-94) and (2-95), the voltage received at RX can be written as

$$V_{RX} = \sum_{n=-\infty}^{\infty} \sum_{p=1}^{\infty} (V^+_{RX,np} + V^-_{RX,np}), \tag{2-113}$$

where

$$V^{\pm}_{RX,np} = -A^{\pm}_{r,np} \rho_R e^{\pm i k_{z,np} z_R} \int_{-\pi}^{\pi} \left[e_{\phi,np}(\rho_R) \pm e_{z,np}(\rho_R) \tan\theta_R \sin(\phi - \phi_R) \right] \times e^{in\phi} e^{\mp i k_{z,np} \rho_R \tan\theta_R \cos(\phi - \phi_R)} \, d\phi. \tag{2-114}$$

Splitting the above equation in sub-integrals, we can solve each one separately, and then by combining the results we can finally obtain

$$V^{\pm}_{RX,np} = -A^{\pm}_{r,np} \rho_R \, 2\pi i^n J_n(\mp\kappa_R) \left[e_{\phi,np}(\rho_R) - \frac{n}{k_{z,np}\rho_R} e_{z,np}(\rho_R) \right] e^{in\phi_R} e^{\pm i k_{z,np} z_R}, \tag{2-115}$$

where

$$\kappa_R = k_{z,np} \, \rho_R \, \tan\theta_R. \tag{2-116}$$

The above voltage result is valid for the case where the TX and the RX antennas are placed in the same axial region. In a generic scenario, let us now assume that the TX lays at the region t and the RX at r. After finding the source amplitudes at the region t by using (2-100), we need to transmit the modal amplitudes to the observation region r. To facilitate these computations, we will now redefine the modal amplitudes for both transmitting and receiving antennas at $z_{T,R} = 0$ and at $\phi_{T,R} = 0$ according to

$$A^{\pm}_{T,np} \rightarrow A^{\pm}_{t,np}(z_T) = A^{\pm}_{t,np} e^{\mp i k_{z,np} z_T}, \tag{2-117}$$

$$A^{\pm}_{R,np} \rightarrow A^{\pm}_{r,np}(z_R) = A^{\pm}_{r,np} e^{\mp i k_{z,np} z_R}, \tag{2-118}$$

$$R_n(\phi', \phi) = e^{in(\phi - \phi')}. \tag{2-119}$$

As a result, we obtain

$$V^{\pm}_{RX,np} = -A^{\pm}_{r,np} \rho_R \, 2\pi i^n J_n(\mp\kappa_R) \left[e_{\phi,np}(\rho_R) - \frac{n}{k_{z,np}\rho_R} e_{z,np}(\rho_R) \right] R_n(\phi_T, \phi_R). \tag{2-120}$$

2.6 Summary of Chapter 2

The mathematical formulation presented in this chapter was numerically implemented via an algorithm described by the flowchart depicted in Figure 2.7.

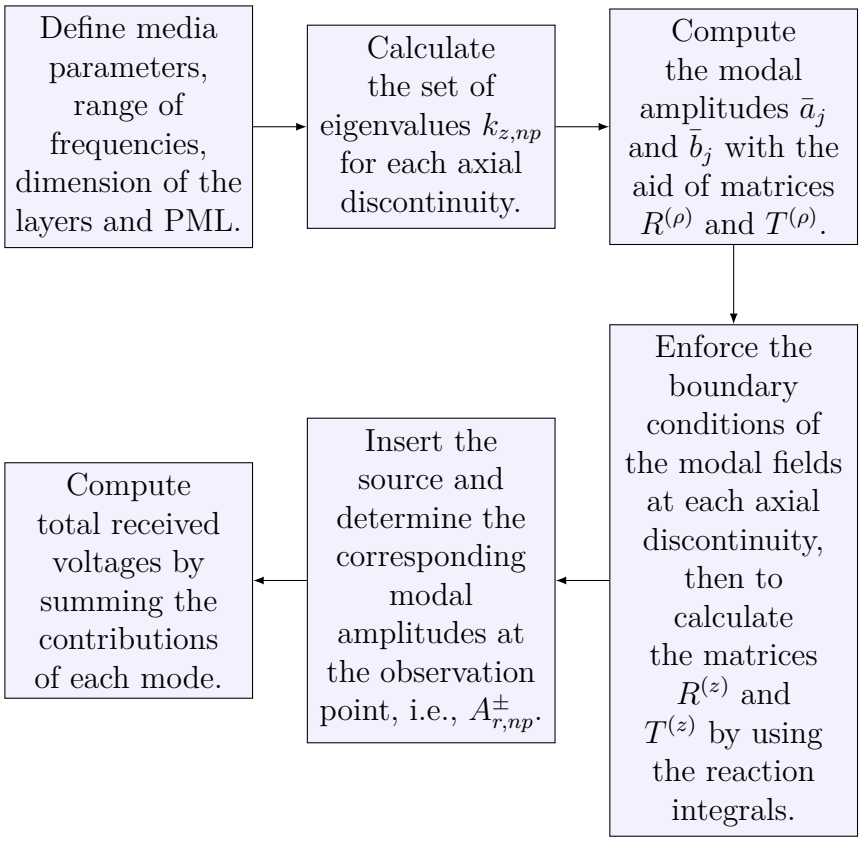

Figure 2.7: Flowchart for the numerical algorithm.

3
Born-Based Approximations for Modeling the Electromagnetic Propagation in Cylindrically-Stratified Formations Perturbed by Three-Dimensional Anisotropic Scatterers

3.1
Introduction

The induced voltage at the RXs (due to a transmitting source TX) is affected by the geophysical environment where antennas are immersed. To ensure an accurate modeling of electromagnetic well-logging sensors, we need an appropriate mathematical description that incorporates the most representative parameters of the geophysical media and the associated borehole geometry. In Chapter 2, we modeled the well-logging environment as an inhomogeneous, dispersive, and anisotropic medium comprising vertical and radial cylindrical layers. However, there are some important scenarios in the underground prospecting of unconventional soil formations where the presence of buried objects perturbs the logging response.

This chapter presents an approximate technique to model the electromagnetic propagation in geophysical formations perturbed by a generic 3D scatterer, as illustrated in Figure 3.1. The main objective is to evaluate the impact of the buried objects on the RXs voltage responses. This formulation will contribute to a low-cost computational algorithm for accounting, in a realistic fashion, the LWD tool response in complex geophysical environments.

The evaluation of electromagnetic fields due to arbitrarily shaped scatterers are related to the solution of the integral equation for EM scattering [37], and several numerical strategies have been used to solve this kind of problem [32, 37, 55, 56]. Nevertheless, the solution of the integral equation via numerical methods yields a complex matrix, which requires an inversion to compute the electromagnetic fields inside the scatterer. Due to multi-scale dimensions of geophysical formations, the operation frequency of LWD tools and the complexity of the media, the computational costs when using conventional EM solvers such as the finite difference method, finite element method (FEM), or method of moments (MoM) can become prohibitive.

The requirements of computer memory storage increase quadratically

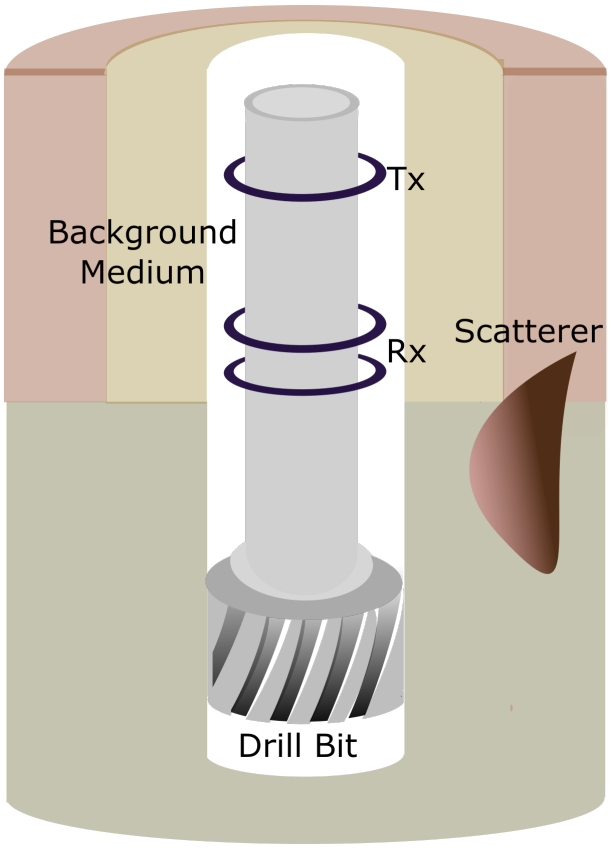

Figure 3.1: Geometry of a prospecting well drilled in a soil formation with a buried scatterer.

with the number of discretization cells [33,34]. As presented in [34], to simulate a typical scattering problem via MoM, with the assumption of 1 million discretization cells, the matrix filling step requires 231 days at the cost of 33 GB of memory. These data were obtained in the year 2003; nowadays, computers have better characteristics that would provide less computational time. However, the computational cost is still extremely high.

Several authors present numerical improvements to decrease the computational requirements of the problem. In [33], a method for electromagnetic modeling of 3D structures inhomogeneous and anisotropic media was presented. The solution is given by an iterative method for solving integral equations. In [35], a numerical technique based on MoM for modeling 3D dielectric objects embedded inside a unique layer was presented. The medium was modeled as a set of planar uniaxial layers; the authors proposed to use a fast Fourier transform (FFT) to accelerate the integral-equation computational time. In [36], a model for electromagnetic scattering of large-size 3D buried-objects was proposed by using the conjugate gradient method combined with a FFT.

Numerical methods presented in [33 – 36] are flexible since they can be

adapted to any geometry, but the computational cost for inversion problems is dramatically high. The MMT proposed in Chapter 2 is not a viable option for modeling scatterers that do not have cylindrical geometry. Some alternative approximated solutions have been explored for computing the associated integral equation problem: the Born approximation (BA), Extended Born Approximation (EBA), High-Order Extended Born, Quasi-Linear, Rytov, distorted Born approximation [29,41,57], among others. These approximations are extensively used to compute the scattering field because of their relatively low computational cost [39].

Some of the techniques mentioned above based on Born approximation (EBA, high-order EBA, Distorted Born approximation) have already been explored for some geophysical applications. In [39], the authors use EBA for computing electromagnetic fields in inhomogeneous media formed by vertically stacked homogeneous layers. They calculate the plane-wave representation of Green's function for homogeneous media in each layer to obtain the electromagnetic fields in the whole problem domain. In [58], a hybrid EBA method associated with spectral-domain methods, was used to solve the electromagnetic problems of axis-symmetric media. In [29], the authors present a hybrid method by using the distorted Born approximation to simulate 3D hydraulic fractures under different operational scenarios. The higher-order Born-based formulations are the most accurate, but they demand more computational resources [39, 42] as will be observed in the formulation developed along this chapter. We will address the problem at hand by using two different BA-based solutions: the conventional BA and EBA on the grounds of the theory in [38, 40].

BA and EBA require the computation of dyadic Green's functions. Obtaining the dyadics is not a trivial task for complex background media because only a limited set of closed-form solutions are known for some particular homogeneous geometries. Besides that, the numerical computation of such dyadics is associated with sizable computational complexity. One of the scientific contributions of this thesis is to obtain the dyadic Green's functions for inhomogeneous and stratified media we have analyzed in Chapter 2. The standard BA approach requires several volumetric integrals over the metallic cylindrical mandrel, the borehole, each vertical and radial layer in addition to the scatterer. The strategy proposed here only requires the computation of volumetric integrals over the scatterer zone.

Other approaches use Cartesian coordinates to represent the vertical layers, e.g, the work in [59]. In these solutions, a tensor approximation (DTA) is first employed to simplify the computation of the dyadic Green's functions for

an inhomogeneous background. There is also available alternative methods that does not require closed-form dyadics, as for example, the work presented in [60], where the scattering fields are obtained in view of a perturbation series. In this theory, the Born approximation is derived as a consequence of the Reciprocity theorem and the conservation of the Reaction of the fields. In a recent report, the authors in [28] proposed a complete hybrid study of electromagnetic propagation through oil wells hydraulic fractures. The procedure presented in that work is complementary to our research and offers a rigorous method that is worth to be mentioned here. The differences in the medium representation, concerning our modeling are: 1) they represent the geophysical formation by planar stratified media (Cartesian coordinates) with a cased borehole, 2) they assume that the fractures are in a single layer of the formation and, 3) the fractures and the background medium have the same magnetic properties. Another recent work in [28] employs a similar methodology for computing the background electromagnetic fields, but the authors have used a numerical mode-matching method (NMM). Then, they determine the Green's functions by using a stabilized biconjugate gradient fast Fourier transform (BCGS-FFT) in planar stratified media. It should be observed that, in our work, the associated Green's functions are obtained via an analytical MMT that does not require any finite-element auxiliary method as that required in the NMM used in [28]. Details of this method can be found in [29]. Note that the dyadic used in this thesis is accurate and describes vertical and radial layers, unlike that specified by the authors referenced in the preceding paragraphs. In their works, the dyadic is calculated only for horizontal layers.

3.2 Theory

The mathematical formalism developed in this section will allow us to obtain the electromagnetic field response of a TX source in the presence of 3D scatterers immersed in complex cylindrical stratified media. Once the scatterer fields have been calculated, we can then obtain the induced voltage at the RXs of a typical LWD sensor.

3.2.1
Dyadic Green's Function in a Cylindrically-Layered Medium

According to the formulation in Chapter 2, the Maxwell's equations in a uniaxial cylindrically-layered medium satisfy

$$\boldsymbol{\nabla} \times \bar{\bar{\mu}}^{-1}(\mathbf{r}) \cdot \boldsymbol{\nabla} \times \mathbf{E}(\mathbf{r}) - \omega^2 \bar{\bar{\epsilon}}(\mathbf{r}) \cdot \mathbf{E}(\mathbf{r}) = i\omega \mathbf{J}(\mathbf{r}) - \boldsymbol{\nabla} \times \bar{\bar{\mu}}^{-1}(\mathbf{r}) \cdot \mathbf{M}(\mathbf{r}) \quad (3\text{-}1)$$

$$\boldsymbol{\nabla} \times \bar{\bar{\epsilon}}^{-1}(\mathbf{r}) \cdot \boldsymbol{\nabla} \times \mathbf{H}(\mathbf{r}) - \omega^2 \bar{\bar{\mu}}(\mathbf{r}) \cdot \mathbf{H}(\mathbf{r}) = i\omega \mathbf{M}(\mathbf{r}) + \boldsymbol{\nabla} \times \bar{\bar{\epsilon}}^{-1}(\mathbf{r}) \cdot \mathbf{J}(\mathbf{r}), \quad (3\text{-}2)$$

the field solution can by expressed as

$$\mathbf{E}(\mathbf{r}) = \int_V \bar{\bar{G}}^{ee}(\mathbf{r}, \mathbf{r}') \cdot \mathbf{J}(\mathbf{r}')\, d\mathbf{r}' + \int_V \bar{\bar{G}}^{eh}(\mathbf{r}, \mathbf{r}') \cdot \mathbf{M}(\mathbf{r}')\, d\mathbf{r}', \quad (3\text{-}3)$$

$$\mathbf{H}(\mathbf{r}) = \int_V \bar{\bar{G}}^{he}(\mathbf{r}, \mathbf{r}') \cdot \mathbf{J}(\mathbf{r}')\, d\mathbf{r}' + \int_V \bar{\bar{G}}^{hh}(\mathbf{r}, \mathbf{r}') \cdot \mathbf{M}(\mathbf{r}')\, d\mathbf{r}', \quad (3\text{-}4)$$

where the electric dyadic Green's function due to an impulsive spatial electric current excitation is given by $\bar{\bar{G}}^{ee}$. All other remaining dyadics are defined according to their superscripts. The first one defines the field, and the second defines the type of excitation current (impulsive electric current or impulsive magnetic current).

3.2.2
Electromagnetic Field Scattered by a 3D Anisotropic Object

Let $\bar{\bar{\epsilon}}(\mathbf{r})$ and $\bar{\bar{\mu}}(\mathbf{r})$ be the electrical permittivity and the magnetic permeability tensors of the geophysical formation depicted in Figure 3.1. We represent the medium as two sub-domains: the soil formation which we will call the background composed by cylindrical conforming layers (with $\bar{\bar{\epsilon}}_b(\mathbf{r})$ and $\bar{\bar{\mu}}_b(\mathbf{r})$), and the volume enclosing the scattering object. The constitutive tensors can now be written as

$$\bar{\bar{\epsilon}}(\mathbf{r}) = \bar{\bar{\epsilon}}_b(\mathbf{r}) + \Delta\bar{\bar{\epsilon}}(\mathbf{r}), \quad (3\text{-}5)$$

$$\bar{\bar{\mu}}(\mathbf{r}) = \bar{\bar{\mu}}_b(\mathbf{r}) + \Delta\bar{\bar{\mu}}(\mathbf{r}), \quad (3\text{-}6)$$

where $\Delta\bar{\bar{\epsilon}}(\mathbf{r})$ and $\Delta\bar{\bar{\mu}}(\mathbf{r})$ describe respectively the permittivity and permeability variations inside the scatterer.

The background electromagnetic problem can be solved appropriately by using the semi-analytic method proposed in [21] and presented in Chapter 2. The scattered fields will be evaluated here employing the induction theorem [51, pp. 113–116], that is, these fields can be thought as the generated by electric or magnetic currents in the obstacle. The electromagnetic fields in the geophysical formation are described by Maxwell's curl equations in the

frequency domain as

$$\nabla \times \mathbf{E}(\mathbf{r}) = i\omega \left[\bar{\bar{\mu}}_b(\mathbf{r}) + \Delta\bar{\bar{\mu}}(\mathbf{r})\right] \cdot \mathbf{H}(\mathbf{r}) - \mathbf{M}_i(\mathbf{r}) \tag{3-7}$$

$$= i\omega\bar{\bar{\mu}}_b(\mathbf{r}) \cdot \mathbf{H}(\mathbf{r}) - \mathbf{M}_i(\mathbf{r}) - \mathbf{M}_s(\mathbf{r}), \tag{3-8}$$

$$\nabla \times \mathbf{H}(\mathbf{r}) = -i\omega \left[\bar{\bar{\epsilon}}_b(\mathbf{r}) + \Delta\bar{\bar{\epsilon}}(\mathbf{r})\right] \cdot \mathbf{E}(\mathbf{r}) + \mathbf{J}_i(\mathbf{r}) \tag{3-9}$$

$$= -i\omega\bar{\bar{\epsilon}}_b(\mathbf{r}) \cdot \mathbf{E}(\mathbf{r}) + \mathbf{J}_i(\mathbf{r}) + \mathbf{J}_s(\mathbf{r}), \tag{3-10}$$

where

$$\mathbf{M}_s(\mathbf{r}) = -i\omega\Delta\bar{\bar{\mu}}(\mathbf{r}) \cdot \mathbf{H}(\mathbf{r}), \tag{3-11}$$

$$\mathbf{J}_s(\mathbf{r}) = -i\omega\Delta\bar{\bar{\epsilon}}(\mathbf{r}) \cdot \mathbf{E}(\mathbf{r}), \tag{3-12}$$

and the impressed sources are given by $\mathbf{J}_i(\mathbf{r})$ and $\mathbf{M}_i(\mathbf{r})$.

By taking the dot product of $\nabla \times \bar{\bar{\mu}}^{-1}(\mathbf{r})$ in both sides of (3-7), we get

$$\nabla \times \bar{\bar{\mu}}^{-1}(\mathbf{r}) \cdot \nabla \times \mathbf{E}(\mathbf{r}) = i\omega\nabla \times \mathbf{H}(\mathbf{r}) - \nabla \times \bar{\bar{\mu}}^{-1}(\mathbf{r}) \cdot \mathbf{M}_i(\mathbf{r}), \tag{3-13}$$

then, substituting (3-13) in (3-9), we obtain

$$\nabla \times \bar{\bar{\mu}}^{-1}(\mathbf{r}) \cdot \nabla \times \mathbf{E}(\mathbf{r}) - \omega^2\, \bar{\bar{\epsilon}}(\mathbf{r}) \cdot \mathbf{E}(\mathbf{r}) = i\omega\mathbf{J}_i(\mathbf{r}) - \nabla \times \bar{\bar{\mu}}^{-1}(\mathbf{r}) \cdot \mathbf{M}_i(\mathbf{r}). \tag{3-14}$$

Similarly, by taking the dot product of $\nabla \times \bar{\bar{\epsilon}}^{-1}(\mathbf{r})$ in (3-9) we can find a dual result, i.e.,

$$\nabla \times \bar{\bar{\epsilon}}^{-1}(\mathbf{r}) \cdot \nabla \times \mathbf{H}(\mathbf{r}) - \omega^2\, \bar{\bar{\mu}}(\mathbf{r}) \cdot \mathbf{H}(\mathbf{r}) = i\omega\mathbf{M}_i(\mathbf{r}) + \nabla \times \bar{\bar{\epsilon}}^{-1}(\mathbf{r}) \cdot \mathbf{J}_i(\mathbf{r}), \tag{3-15}$$

subtracting $\nabla \times \bar{\bar{\mu}}_b^{-1}(\mathbf{r}) \cdot \nabla \times \mathbf{E}(\mathbf{r}) - \omega^2\bar{\bar{\epsilon}}_b(\mathbf{r}) \cdot \mathbf{E}(\mathbf{r})$ from both sides in (3-14), we have

$$\nabla \times \left[\bar{\bar{\mu}}^{-1}(\mathbf{r}) - \bar{\bar{\mu}}_b^{-1}(\mathbf{r})\right] \cdot \nabla \times \mathbf{E}(\mathbf{r}) - \omega^2 \left[\bar{\bar{\epsilon}}(\mathbf{r}) - \bar{\bar{\epsilon}}_b(\mathbf{r})\right] \cdot \mathbf{E}(\mathbf{r}) =$$
$$i\omega\mathbf{J}_i(\mathbf{r}) - \nabla \times \bar{\bar{\mu}}^{-1}(\mathbf{r}) \cdot \mathbf{M}_i(\mathbf{r}) - \nabla \times \bar{\bar{\mu}}_b^{-1}(\mathbf{r}) \cdot \nabla \times \mathbf{E}(\mathbf{r}) + \omega^2\bar{\bar{\epsilon}}_b(\mathbf{r}) \cdot \mathbf{E}(\mathbf{r}). \tag{3-16}$$

Subtracting $\nabla \times \bar{\bar{\epsilon}}_b^{-1}(\mathbf{r}) \cdot \nabla \times \mathbf{H}(\mathbf{r}) - \omega^2\bar{\bar{\mu}}_b(\mathbf{r}) \cdot \mathbf{H}(\mathbf{r})$ from both sides of (3-15) results in

$$\nabla \times \left[\bar{\bar{\epsilon}}^{-1}(\mathbf{r}) - \bar{\bar{\epsilon}}_b^{-1}(\mathbf{r})\right] \cdot \nabla \times \mathbf{H}(\mathbf{r}) - \omega^2 \left[\bar{\bar{\mu}}(\mathbf{r}) - \bar{\bar{\mu}}_b(\mathbf{r})\right] \cdot \mathbf{H}(\mathbf{r}) =$$
$$i\omega\mathbf{M}_i(\mathbf{r}) + \nabla \times \bar{\bar{\epsilon}}^{-1}(\mathbf{r}) \cdot \mathbf{J}_i(\mathbf{r}) - \nabla \times \bar{\bar{\epsilon}}_b^{-1}(\mathbf{r}) \cdot \nabla \times \mathbf{H}(\mathbf{r}) + \omega^2\bar{\bar{\mu}}_b(\mathbf{r}) \cdot \mathbf{H}(\mathbf{r}), \tag{3-17}$$

by using the definitions in (3-5) and (3-6) in equations (3-16) and (3-17), and

rearranging the expressions we obtain:

$$\nabla \times \bar{\bar{\mu}}_b^{-1}(\mathbf{r}) \cdot \nabla \times \mathbf{E}(\mathbf{r}) - \omega^2 \bar{\bar{\epsilon}}_b(\mathbf{r}) \cdot \mathbf{E}(\mathbf{r}) = i\omega \mathbf{J}_i(\mathbf{r}) - \nabla \times \bar{\bar{\mu}}^{-1}(\mathbf{r}) \cdot \mathbf{M}_i(\mathbf{r}) + \omega^2 \, \Delta\bar{\bar{\epsilon}}(\mathbf{r}) \cdot \mathbf{E}(\mathbf{r}) - \nabla \times \left[\bar{\bar{\mu}}^{-1}(\mathbf{r}) - \bar{\bar{\mu}}_b^{-1}(\mathbf{r})\right] \cdot \nabla \times \mathbf{E}(\mathbf{r}), \quad (3\text{-}18)$$

$$\nabla \times \bar{\bar{\epsilon}}_b^{-1}(\mathbf{r}) \cdot \nabla \times \mathbf{H}(\mathbf{r}) - \omega^2 \bar{\bar{\mu}}_b(\mathbf{r}) \cdot \mathbf{H}(\mathbf{r}) = i\omega \mathbf{M}_i(\mathbf{r}) + \nabla \times \bar{\bar{\epsilon}}^{-1}(\mathbf{r}) \cdot \mathbf{J}_i(\mathbf{r}) + \omega^2 \, \Delta\bar{\bar{\mu}}(\mathbf{r}) \cdot \mathbf{H}(\mathbf{r}) - \nabla \times \left[\bar{\bar{\epsilon}}^{-1}(\mathbf{r}) - \bar{\bar{\epsilon}}_b^{-1}(\mathbf{r})\right] \cdot \nabla \times \mathbf{H}(\mathbf{r}). \quad (3\text{-}19)$$

To compute the scattered field notice the wave equations in (3-18) and (3-19). Particularly, the latter terms in both expression can by rewritten via the following dyadic identities:

$$\left[\bar{\bar{p}}^{-1}(\mathbf{r}) - \bar{\bar{p}}_b^{-1}(\mathbf{r})\right] = \bar{\bar{p}}_b^{-1}(\mathbf{r}) \cdot \bar{\bar{p}}_b(\mathbf{r}) \cdot \left[\bar{\bar{p}}^{-1}(\mathbf{r}) - \bar{\bar{p}}_b^{-1}(\mathbf{r})\right] \cdot \bar{\bar{p}}(\mathbf{r}) \cdot \bar{\bar{p}}^{-1}(\mathbf{r}) \quad (3\text{-}20)$$

$$= \bar{\bar{p}}_b^{-1}(\mathbf{r}) \cdot \left[\bar{\bar{p}}_b(\mathbf{r}) - \bar{\bar{p}}(\mathbf{r})\right] \cdot \bar{\bar{p}}^{-1}(\mathbf{r}) \quad (3\text{-}21)$$

$$= -\bar{\bar{p}}_b^{-1}(\mathbf{r}) \cdot \Delta\bar{\bar{p}}(\mathbf{r}) \cdot \bar{\bar{p}}^{-1}(\mathbf{r}), \quad \text{where } p = \{\epsilon, \mu\}, \quad (3\text{-}22)$$

now, the vector wave equations become

$$\nabla \times \bar{\bar{\mu}}_b^{-1}(\mathbf{r}) \cdot \nabla \times \mathbf{E}(\mathbf{r}) - \omega^2 \bar{\bar{\epsilon}}_b(\mathbf{r}) \cdot \mathbf{E}(\mathbf{r}) = i\omega \mathbf{J}_i(\mathbf{r}) - \nabla \times \bar{\bar{\mu}}^{-1}(\mathbf{r}) \cdot \mathbf{M}_i(\mathbf{r}) + \omega^2 \, \Delta\bar{\bar{\epsilon}}(\mathbf{r}) \cdot \mathbf{E}(\mathbf{r}) + \nabla \times \bar{\bar{\mu}}_b^{-1}(\mathbf{r}) \cdot \Delta\bar{\bar{\mu}}(\mathbf{r}) \cdot \bar{\bar{\mu}}^{-1}(\mathbf{r}) \cdot \nabla \times \mathbf{E}(\mathbf{r}), \quad (3\text{-}23)$$

$$\nabla \times \bar{\bar{\epsilon}}_b^{-1}(\mathbf{r}) \cdot \nabla \times \mathbf{H}(\mathbf{r}) - \omega^2 \bar{\bar{\mu}}_b(\mathbf{r}) \cdot \mathbf{H}(\mathbf{r}) = i\omega \mathbf{M}_i(\mathbf{r}) + \nabla \times \bar{\bar{\epsilon}}^{-1}(\mathbf{r}) \cdot \mathbf{J}_i(\mathbf{r}) + \omega^2 \, \Delta\bar{\bar{\mu}}(\mathbf{r}) \cdot \mathbf{H}(\mathbf{r}) + \nabla \times \bar{\bar{\epsilon}}_b^{-1}(\mathbf{r}) \cdot \Delta\bar{\bar{\epsilon}}(\mathbf{r}) \cdot \bar{\bar{\epsilon}}^{-1}(\mathbf{r}) \cdot \nabla \times \mathbf{H}(\mathbf{r}). \quad (3\text{-}24)$$

The last equations can be further simplified by means of the Ampere and Faraday laws, since

$$\nabla \times \bar{\bar{\mu}}_b^{-1}(\mathbf{r}) \cdot \Delta\bar{\bar{\mu}}(\mathbf{r}) \cdot \bar{\bar{\mu}}^{-1}(\mathbf{r}) \cdot \nabla \times \mathbf{E}(\mathbf{r})$$

$$= \nabla \times \bar{\bar{\mu}}_b^{-1}(\mathbf{r}) \cdot \Delta\bar{\bar{\mu}}(\mathbf{r}) \cdot \left[i\omega \mathbf{H}(\mathbf{r}) - \bar{\bar{\mu}}^{-1}(\mathbf{r}) \cdot \mathbf{M}_i(\mathbf{r})\right] \quad (3\text{-}25)$$

$$= i\omega \nabla \times \bar{\bar{\mu}}_b^{-1}(\mathbf{r}) \cdot \Delta\bar{\bar{\mu}}(\mathbf{r}) \cdot \mathbf{H}(\mathbf{r}) - \nabla \times \left[\bar{\bar{\mu}}_b^{-1}(\mathbf{r}) - \bar{\bar{\mu}}^{-1}(\mathbf{r})\right] \cdot \mathbf{M}_i \quad (3\text{-}26)$$

$$\nabla \times \bar{\bar{\epsilon}}_b^{-1}(\mathbf{r}) \cdot \Delta\bar{\bar{\epsilon}}(\mathbf{r}) \cdot \bar{\bar{\epsilon}}^{-1}(\mathbf{r}) \cdot \nabla \times \mathbf{H}(\mathbf{r})$$

$$= \nabla \times \bar{\bar{\epsilon}}_b^{-1}(\mathbf{r}) \cdot \Delta\bar{\bar{\epsilon}}(\mathbf{r}) \cdot \left[-i\omega \mathbf{E}(\mathbf{r}) + \bar{\bar{\epsilon}}^{-1}(\mathbf{r}) \cdot \mathbf{J}_i\right] \quad (3\text{-}27)$$

$$= -i\omega \nabla \times \bar{\bar{\epsilon}}_b^{-1}(\mathbf{r}) \cdot \Delta\bar{\bar{\epsilon}}(\mathbf{r}) \cdot \mathbf{E}(\mathbf{r}) + \nabla \times \left[\bar{\bar{\epsilon}}_b^{-1} - \bar{\bar{\epsilon}}^{-1}\right] \cdot \mathbf{J}_i, \quad (3\text{-}28)$$

that allows us to obtain

$$\boldsymbol{\nabla}\times\bar{\bar{\mu}}_b^{-1}(\mathbf{r})\cdot\boldsymbol{\nabla}\times\mathbf{E}(\mathbf{r})-\omega^2\bar{\bar{\epsilon}}_b(\mathbf{r})\cdot\mathbf{E}(\mathbf{r})=i\omega\mathbf{J}_i(\mathbf{r})-\boldsymbol{\nabla}\times\bar{\bar{\mu}}_b^{-1}(\mathbf{r})\cdot\mathbf{M}_i(\mathbf{r})$$
$$+\omega^2\,\Delta\bar{\bar{\epsilon}}(\mathbf{r})\cdot\mathbf{E}(\mathbf{r})+i\omega\boldsymbol{\nabla}\times\bar{\bar{\mu}}_b^{-1}(\mathbf{r})\cdot\Delta\bar{\bar{\mu}}(\mathbf{r})\cdot\mathbf{H}(\mathbf{r}),\quad(3\text{-}29)$$

$$\boldsymbol{\nabla}\times\bar{\bar{\epsilon}}_b^{-1}(\mathbf{r})\cdot\boldsymbol{\nabla}\times\mathbf{H}(\mathbf{r})-\omega^2\bar{\bar{\mu}}_b(\mathbf{r})\cdot\mathbf{H}(\mathbf{r})=i\omega\mathbf{M}_i(\mathbf{r})+\boldsymbol{\nabla}\times\bar{\bar{\epsilon}}_b^{-1}\cdot\mathbf{J}_i$$
$$+\omega^2\,\Delta\bar{\bar{\mu}}(\mathbf{r})\cdot\mathbf{H}(\mathbf{r})-i\omega\boldsymbol{\nabla}\times\bar{\bar{\epsilon}}_b^{-1}(\mathbf{r})\cdot\Delta\bar{\bar{\epsilon}}(\mathbf{r})\cdot\mathbf{E}(\mathbf{r}).\quad(3\text{-}30)$$

Then, on comparing (3-29) and (3-30) with (3-1) and (3-2), we deduce that, they are equivalent to each other when the source currents are

$$\mathbf{J}=\mathbf{J}_i-i\omega\Delta\bar{\bar{\epsilon}}(\mathbf{r})\cdot\mathbf{E}(\mathbf{r}),\quad(3\text{-}31)$$
$$\mathbf{M}=\mathbf{M_i}-i\omega\Delta\bar{\bar{\mu}}(\mathbf{r})\cdot\mathbf{H}(\mathbf{r}).\quad(3\text{-}32)$$

As a result, the fields due to these sources can be finally computed via (3-3) and (3-4), i.e.,

$$\mathbf{E}(\mathbf{r})=\mathbf{E}_b(\mathbf{r})-i\omega\int_V\bar{\bar{G}}^{ee}(\mathbf{r},\mathbf{r}_0)\cdot\Delta\bar{\bar{\epsilon}}\cdot\mathbf{E}(\mathbf{r}_0)\,d\mathbf{r}_0-i\omega\int_V\bar{\bar{G}}^{eh}(\mathbf{r},\mathbf{r}_0)\cdot\Delta\bar{\bar{\mu}}\cdot\mathbf{H}(\mathbf{r}_0)\,d\mathbf{r}_0,\quad(3\text{-}33)$$

$$\mathbf{H}(\mathbf{r})=\mathbf{H}_b(\mathbf{r})-i\omega\int_V\bar{\bar{G}}^{he}(\mathbf{r},\mathbf{r}_0)\cdot\Delta\bar{\bar{\epsilon}}\cdot\mathbf{E}(\mathbf{r}_0)\,d\mathbf{r}_0-i\omega\int_V\bar{\bar{G}}^{hh}(\mathbf{r},\mathbf{r}_0)\cdot\Delta\bar{\bar{\mu}}\cdot\mathbf{H}(\mathbf{r}_0)\,d\mathbf{r}_0,\quad(3\text{-}34)$$

where

$$\mathbf{E}_b(\mathbf{r})=\int_V\bar{\bar{G}}^{ee}(\mathbf{r},\mathbf{r}_0)\cdot\mathbf{J}_i\,d\mathbf{r}_0+\int_V\bar{\bar{G}}^{eh}(\mathbf{r},\mathbf{r}_0)\cdot\mathbf{M}_i\,d\mathbf{r}_0,\quad(3\text{-}35)$$
$$\mathbf{H}_b(\mathbf{r})=\int_V\bar{\bar{G}}^{he}(\mathbf{r},\mathbf{r}_0)\cdot\mathbf{J}_i\,d\mathbf{r}_0+\int_V\bar{\bar{G}}^{hh}(\mathbf{r},\mathbf{r}_0)\cdot\mathbf{M}_i\,d\mathbf{r}_0,\quad(3\text{-}36)$$

$$\mathbf{E}_s(\mathbf{r})=-i\omega\int_V\bar{\bar{G}}^{ee}(\mathbf{r},\mathbf{r}_0)\cdot\Delta\bar{\bar{\epsilon}}\cdot\mathbf{E}(\mathbf{r}_0)\,d\mathbf{r}_0-i\omega\int_V\bar{\bar{G}}^{eh}(\mathbf{r},\mathbf{r}_0)\cdot\Delta\bar{\bar{\mu}}\cdot\mathbf{H}(\mathbf{r}_0)\,d\mathbf{r}_0,\quad(3\text{-}37)$$

$$\mathbf{H}_s(\mathbf{r})=-i\omega\int_V\bar{\bar{G}}^{he}(\mathbf{r},\mathbf{r}_0)\cdot\Delta\bar{\bar{\epsilon}}\cdot\mathbf{E}(\mathbf{r}_0)\,d\mathbf{r}_0-i\omega\int_V\bar{\bar{G}}^{hh}(\mathbf{r},\mathbf{r}_0)\cdot\Delta\bar{\bar{\mu}}\cdot\mathbf{H}(\mathbf{r}_0)\,d\mathbf{r}_0.\quad(3\text{-}38)$$

3.2.2.1 Born Approximation

If $\Delta\bar{\bar{\epsilon}}$ and $\Delta\bar{\bar{\mu}}$ are relatively small, in order that the second and third terms in (3-33) and (3-34) are small compared with the first term ($\mathbf{E}_b$ or $\mathbf{H}_b$), we can approximate the fields inside the volume as the ones of the background, i.e.,:

$$\mathbf{E}(\mathbf{r}_0) \approx \mathbf{E}_b(\mathbf{r}_0), \tag{3-39}$$

$$\mathbf{H}(\mathbf{r}_0) \approx \mathbf{H}_b(\mathbf{r}_0), \tag{3-40}$$

therefore, the total fields can be computed substituting (3-39) and (3-40) into (3-33) and (3-34), i.e.

$$\mathbf{E}(\mathbf{r}) = \mathbf{E}_b(\mathbf{r}) - i\omega \int_V \bar{\bar{G}}^{ee}(\mathbf{r},\mathbf{r}_0)\cdot\Delta\bar{\bar{\epsilon}}\cdot\mathbf{E}_b(\mathbf{r}_0)\, d\mathbf{r}_0 - i\omega \int_V \bar{\bar{G}}^{eh}(\mathbf{r},\mathbf{r}_0)\cdot\Delta\bar{\bar{\mu}}\cdot\mathbf{H}_b(\mathbf{r}_0)\, d\mathbf{r}_0, \tag{3-41}$$

$$\mathbf{H}(\mathbf{r}) = \mathbf{H}_b(\mathbf{r}) - i\omega \int_V \bar{\bar{G}}^{he}(\mathbf{r},\mathbf{r}_0)\cdot\Delta\bar{\bar{\epsilon}}\cdot\mathbf{E}_b(\mathbf{r}_0)\, d\mathbf{r}_0 - i\omega \int_V \bar{\bar{G}}^{hh}(\mathbf{r},\mathbf{r}_0)\cdot\Delta\bar{\bar{\mu}}\cdot\mathbf{H}_b(\mathbf{r}_0)\, d\mathbf{r}_0. \tag{3-42}$$

3.2.2.2 Extended Born Approximation

Expressions (3-33) and (3-34) form a system of coupled inhomogeneous Fredholm vector-equation of the second kind, and finding the field solutions $\mathbf{E}(\mathbf{r})$ and $\mathbf{H}(\mathbf{r})$ is not an easy task. The main difficult here, compared to other methods presented in literature [28, 32, 37 – 41], is the analysis of magneto-dielectric scatterers, i.e. the simultaneous presence of the contrasts $\Delta\bar{\bar{\epsilon}}(\mathbf{r})$ and $\Delta\bar{\bar{\mu}}(\mathbf{r})$. The particular case of $\Delta\bar{\bar{\mu}}(\mathbf{r}) = \bar{\bar{0}}$, however, leads to a well-establish problem with solution typically obtained by expanding the unknown field $\mathbf{E}(\mathbf{r})$ in terms of appropriate vector-basis functions [37, Sec. 8.9.3]. The Galerkin's method can then be employed to convert the problem into a matrix equation, and its solution will determine $\mathbf{E}(\mathbf{r})$. A similar approach can be used for solving $\mathbf{H}(\mathbf{r})$ in a direct fashion, or Faraday's law can also provide us such a field if we have solved $\mathbf{E}(\mathbf{r})$ for first. In what follows, we presents a decoupling methodology for the solution of the system in (3-33) and (3-34).

At this point, it is convenient to evaluate Taylor series of $\mathbf{E}(\mathbf{r}_0)$ in the vicinity of observation point $\mathbf{r}$ [53], i.e

$$\mathbf{E}(\mathbf{r}_0)\cdot\hat{\alpha} = \mathbf{E}(\mathbf{r})\cdot\hat{\alpha} + (\mathbf{r}_0-\mathbf{r})\cdot\nabla[\mathbf{E}(\mathbf{r})\cdot\hat{\alpha}] + \frac{1}{2}(\mathbf{r}_0-\mathbf{r})\cdot\nabla\nabla[\mathbf{E}(\mathbf{r})\cdot(\mathbf{r}_0-\mathbf{r})\cdot\hat{\alpha}] + ... \tag{3-43}$$

if the scatterer and the observation point are close to each other, we could approximate $(\mathbf{r}_0 - \mathbf{r}) \approx \mathbf{0}$. Consequently, the expression (3-43) can be approximated by the first term of the series

$$\mathbf{E}(\mathbf{r}_0) \approx \mathbf{E}(\mathbf{r}). \tag{3-44}$$

From the above approximation, we can express the fields inside the scatterer as

$$\mathbf{E}(\mathbf{r}_0) \approx \mathbf{E}(\mathbf{r}), \tag{3-45}$$

$$\mathbf{H}(\mathbf{r}_0) \approx \mathbf{H}(\mathbf{r}), \tag{3-46}$$

therefore, the system in (3-33) and (3-34) can be calculated as the following matrix equation

$$\begin{bmatrix}\mathbf{E}(\mathbf{r})\\ \mathbf{H}(\mathbf{r})\end{bmatrix} = \begin{bmatrix}\mathbf{E}_b(\mathbf{r})\\ \mathbf{H}_b(\mathbf{r})\end{bmatrix} + \begin{bmatrix}\bar{\bar{S}}^{ee}(\mathbf{r}) & \bar{\bar{S}}^{eh}(\mathbf{r})\\ \bar{\bar{S}}^{he}(\mathbf{r}) & \bar{\bar{S}}^{hh}(\mathbf{r})\end{bmatrix} \cdot \begin{bmatrix}\mathbf{E}(\mathbf{r})\\ \mathbf{H}(\mathbf{r})\end{bmatrix}, \tag{3-47}$$

where was introduced four new scattering tensors:

$$\bar{\bar{S}}^{ee}(\mathbf{r}) = -i\omega \int_V \bar{\bar{G}}^{ee}(\mathbf{r}, \mathbf{r}_0) \cdot \Delta\bar{\bar{\epsilon}}\, d\mathbf{r}_0, \tag{3-48}$$

$$\bar{\bar{S}}^{eh}(\mathbf{r}) = -i\omega \int_V \bar{\bar{G}}^{eh}(\mathbf{r}, \mathbf{r}_0) \cdot \Delta\bar{\bar{\mu}}\, d\mathbf{r}_0, \tag{3-49}$$

$$\bar{\bar{S}}^{he}(\mathbf{r}) = -i\omega \int_V \bar{\bar{G}}^{he}(\mathbf{r}, \mathbf{r}_0) \cdot \Delta\bar{\bar{\epsilon}}\, d\mathbf{r}_0, \tag{3-50}$$

$$\bar{\bar{S}}^{hh}(\mathbf{r}) = -i\omega \int_V \bar{\bar{G}}^{hh}(\mathbf{r}, \mathbf{r}_0) \cdot \Delta\bar{\bar{\mu}}\, d\mathbf{r}_0. \tag{3-51}$$

Now, we can relate $[\mathbf{E}(\mathbf{r})\ \mathbf{H}(\mathbf{r})]^t$ in (3-47) as a function of the background field counterparts:

$$\begin{bmatrix}\mathbf{E}(\mathbf{r})\\ \mathbf{H}(\mathbf{r})\end{bmatrix} = \begin{bmatrix}\bar{\bar{I}} - \bar{\bar{S}}^{ee}(\mathbf{r}) & -\bar{\bar{S}}^{eh}(\mathbf{r})\\ -\bar{\bar{S}}^{he}(\mathbf{r}) & \bar{\bar{I}} - \bar{\bar{S}}^{hh}(\mathbf{r})\end{bmatrix}^{-1} \cdot \begin{bmatrix}\mathbf{E}_b(\mathbf{r})\\ \mathbf{H}_b(\mathbf{r})\end{bmatrix} \tag{3-52}$$

$$= \begin{bmatrix}\bar{\bar{\Lambda}}^{ee}(\mathbf{r}) & \bar{\bar{\Lambda}}^{eh}(\mathbf{r})\\ \bar{\bar{\Lambda}}^{he}(\mathbf{r}) & \bar{\bar{\Lambda}}^{hh}(\mathbf{r})\end{bmatrix} \cdot \begin{bmatrix}\mathbf{E}_b(\mathbf{r})\\ \mathbf{H}_b(\mathbf{r})\end{bmatrix} \tag{3-53}$$

$$= \bar{\bar{\Lambda}}(\mathbf{r}) \cdot \begin{bmatrix}\mathbf{E}_b(\mathbf{r})\\ \mathbf{H}_b(\mathbf{r})\end{bmatrix}. \tag{3-54}$$

The above generalized scattering tensor $\bar{\bar{\Lambda}}(\mathbf{r})$ is composed by the sub-elements:

$$\bar{\bar{\Lambda}}^{ee}(\mathbf{r}) = \left[\bar{\bar{I}} - \bar{\bar{S}}^{ee}(\mathbf{r})\right]^{-1} + \left[\bar{\bar{I}} - \bar{\bar{S}}^{ee}(\mathbf{r})\right]^{-1} \cdot \bar{\bar{S}}^{eh}(\mathbf{r}) \cdot \bar{\bar{M}}_1(\mathbf{r}) \cdot \bar{\bar{S}}^{he}(\mathbf{r}) \cdot \left[\bar{\bar{I}} - \bar{\bar{S}}^{ee}(\mathbf{r})\right]^{-1}, \tag{3-55}$$

$$\bar{\bar{\Lambda}}^{hh}(\mathbf{r}) = \left[\bar{\bar{I}} - \bar{\bar{S}}^{hh}(\mathbf{r})\right]^{-1} + \left[\bar{\bar{I}} - \bar{\bar{S}}^{hh}(\mathbf{r})\right]^{-1} \cdot \bar{\bar{S}}^{he}(\mathbf{r}) \cdot \bar{\bar{M}}_2(\mathbf{r}) \cdot \bar{\bar{S}}^{eh}(\mathbf{r}) \cdot \left[\bar{\bar{I}} - \bar{\bar{S}}^{hh}(\mathbf{r})\right]^{-1}, \tag{3-56}$$

$$\bar{\bar{\Lambda}}^{eh}(\mathbf{r}) = \bar{\bar{\Lambda}}^{ee} \cdot \bar{\bar{S}}^{eh}(\mathbf{r}) \cdot \left[\bar{\bar{I}} - \bar{\bar{S}}^{hh}(\mathbf{r})\right]^{-1}, \tag{3-57}$$

$$\bar{\bar{\Lambda}}^{he}(\mathbf{r}) = \bar{\bar{\Lambda}}^{hh} \cdot \bar{\bar{S}}^{he}(\mathbf{r}) \cdot \left[\bar{\bar{I}} - \bar{\bar{S}}^{ee}(\mathbf{r})\right]^{-1}, \tag{3-58}$$

where

$$\bar{\bar{M}}_1(\mathbf{r}) = \left\{\bar{\bar{I}} - \bar{\bar{S}}^{hh}(\mathbf{r}) - \bar{\bar{S}}^{he}(\mathbf{r}) \cdot \left[\bar{\bar{I}} - \bar{\bar{S}}^{ee}(\mathbf{r})\right]^{-1} \cdot \bar{\bar{S}}^{eh}(\mathbf{r})\right\}^{-1}, \tag{3-59}$$

$$\bar{\bar{M}}_2(\mathbf{r}) = \left\{\bar{\bar{I}} - \bar{\bar{S}}^{ee}(\mathbf{r}) - \bar{\bar{S}}^{eh}(\mathbf{r}) \cdot \left[\bar{\bar{I}} - \bar{\bar{S}}^{hh}(\mathbf{r})\right]^{-1} \cdot \bar{\bar{S}}^{he}(\mathbf{r})\right\}^{-1}. \tag{3-60}$$

The final fields $\mathbf{E}(\mathbf{r})$ and $\mathbf{H}(\mathbf{r})$ in (3-52) are valid approximations for points around or inside the scatterer ($\mathbf{r}_0 - \mathbf{r} \approx \mathbf{0}$). To get a solution at any point, we should re-radiate the approximated field solution. The expression (3-54) in (3-33) and (3-34) results in

$$\begin{aligned}\mathbf{E}(\mathbf{r}) =& \mathbf{E}_b(\mathbf{r}) - i\omega \int_V \bar{\bar{G}}^{ee}(\mathbf{r}, \mathbf{r}_0) \cdot \Delta\bar{\bar{\epsilon}} \cdot \bar{\bar{\Lambda}}(\mathbf{r}_0) \cdot \mathbf{E}_b(\mathbf{r}_0)\, d\mathbf{r}_0 \\ & - i\omega \int_V \bar{\bar{G}}^{eh}(\mathbf{r}, \mathbf{r}_0) \cdot \Delta\bar{\bar{\mu}} \cdot \bar{\bar{\Lambda}}(\mathbf{r}_0) \cdot \mathbf{H}_b(\mathbf{r}_0)\, d\mathbf{r}_0,\end{aligned} \tag{3-61}$$

$$\begin{aligned}\mathbf{H}(\mathbf{r}) =& \mathbf{H}_b(\mathbf{r}) - i\omega \int_V \bar{\bar{G}}^{he}(\mathbf{r}, \mathbf{r}_0) \cdot \Delta\bar{\bar{\epsilon}} \cdot \bar{\bar{\Lambda}}(\mathbf{r}_0) \cdot \mathbf{E}_b(\mathbf{r}_0)\, d\mathbf{r}_0 \\ & - i\omega \int_V \bar{\bar{G}}^{hh}(\mathbf{r}, \mathbf{r}_0) \cdot \Delta\bar{\bar{\mu}} \cdot \bar{\bar{\Lambda}}(\mathbf{r}_0) \cdot \mathbf{H}_b(\mathbf{r}_0)\, d\mathbf{r}_0.\end{aligned} \tag{3-62}$$

From a computational point of view, the re-radiation process demands additional resources than required via BA. It is due to the that the term $\bar{\bar{\Lambda}}(\mathbf{r}_0)$ in the EBA approach, requires the computation of multiple integrals (one for each scatterer discretization point).

3.2.3 Electric Current Source

According to Figure 3.1, when the scatterer is absent, the fields at an observation point are given by $\mathbf{E}_b(\mathbf{r})$ and $\mathbf{H}_b(\mathbf{r})$. This is the solution obtained

by the semi-analytic mode-matching technique presented in Chapter 2. If the scatterer is present, the field solution will be approximated by the BA or EBA. These methods require to calculate the dyadic Green's functions for the background media. Such dyadics admit closed-form solutions just for a limited number of cases [37, Ch. 7]. The dyadic Green's functions we employ in this study are an original contribution when compared with other approaches where is used homogeneous dyadics for solving similar cases [39, 40, 42]. Those approaches require the numerical calculation of volumetric integrals throughout the whole domain (background and scatterer) to compute the total fields, demanding additional computational effort. The solution method proposed herein employs the analytical fields in cylindrically stratified media, with both radial and axial stratifications as a base for the BA or EBA, hence only one integral is needed to obtain the total fields.

In cylindrical coordinates, for a impulsive-electric current source, we can write the electric dyadic as:

$$\bar{\bar{G}}^{ee}(\mathbf{r},\mathbf{r}_0)=\begin{bmatrix} G^{ee}_{\rho\rho} & G^{ee}_{\rho\phi} & G^{ee}_{\rho z} \\ G^{ee}_{\phi\rho} & G^{ee}_{\phi\phi} & G^{ee}_{\phi z} \\ G^{ee}_{z\rho} & G^{ee}_{z\phi} & G^{ee}_{zz} \end{bmatrix}, \tag{3-63}$$

where $G^{ee}_{\alpha\beta}$ is the component α of electric field at the point of observation $\mathbf{r}$ due to an electric point excitation at $\mathbf{r}_0$ with polarization in the β direction, i.e.,

$$G^{ee}_{\alpha\beta}=\mathbf{E}\Big[\mathbf{r};\,\mathbf{J}_i=\hat{\beta}\delta(\mathbf{r}-\mathbf{r}_0)\Big]\cdot\hat{\alpha}. \tag{3-64}$$

It is important to stress that the scatterer acts as an equivalent source and its field convergence, and dyadics should be evaluated independently of the primary one radiated by the coil TX. For example, for a horizontal TX coil, we can show that only modal fields associated with the azimuthal harmonic $n=0$ contributes to $\mathbf{E}_b(\mathbf{r})$ because of the symmetry of the problem [21, 61, 62]. However, the asymmetric geometry of the scatterer requires high order harmonics $n=\{0,\pm1,\pm2,\pm3,...\}$ for computing $\mathbf{E}_s(\mathbf{r})$.

For obtaining the dyadic coefficients due to the electric source $\mathbf{J}_i=\hat{\beta}\,\delta(\mathbf{r}-\mathbf{r}_0)$, $\hat{\beta}=\{\hat{\rho},\hat{\phi},\hat{z}\}$ via MMT, we need to calculate the modal amplitudes $\bar{A}_r$ due to each component of the impulsive source by using (2-80)-(2-83) and (2-94)-(2-97). The matrices $\bar{\bar{P}},\bar{\bar{T}},\bar{\bar{M}},\bar{\bar{U}}$ required to calculate $\bar{A}_r$ can be reused from the expressions presented in Section 2.3. However, we have to redefine the modal source amplitudes $\bar{A}_{r_0}$. To distinguish the source amplitudes due to each impulsive component, we define $\bar{A}^{\pm}_{r_0}\rightarrow\bar{A}^{\pm}_{r_0,\beta}$ that represents the modal source amplitudes due to the β component of the impulsive source. We compute these amplitudes with the aid of the coefficients $S^{\pm}_{np}$ and $N^{\pm}_{np}$ given in (2-100); i.e.,

$$A^{\pm}_{r_0,\beta} = \frac{S^{\pm}_{np}}{N^{\pm}_{np}}, \tag{3-65}$$

where

$$S^{\pm}_{np} = (-1)^n \int_V \Big[(-s_n e_{\rho,np}\hat{\rho} + e_{\phi,np}\hat{\phi} \pm s_n e_{z,np}\hat{z}) \cdot \mathbf{J}_i \pm (h_{\rho,np}\hat{\rho} - s_n h_{\phi,np}\hat{\phi} \mp h_{z,np}\hat{z}) \cdot \mathbf{M}_i\Big] e^{-in\phi} e^{\mp ik_{z,np}z}\, dv, \tag{3-66}$$

$$s_n = 1 - 2\,\delta_{0,n}, \tag{3-67}$$

$$\begin{aligned} N_{np} &= 4\pi(-1)^n \int (s_n e_{\rho,np} h_{\phi,np} + e_{\phi,np} h_{\rho,np})\rho\, d\rho \\ &= -2\,Q_{np}. \end{aligned} \tag{3-68}$$

$\mathbf{J}_i$ and $\mathbf{M}_i$ are the space impulsive vectors, and their volumetric integral in (3-66) becomes trivial. We can define $S^{\pm}_{np}$ for each source component as follows.

3.2.3.1 Electric Current Source for ρ Polarization

Considering $\beta = \rho$, we get

$$\begin{aligned} S^{(\rho)\pm}_{np} &= (-1)^n \int_V (-s_n e_{\rho,np})\delta(\rho-\rho_0)\delta(z-z_0)\frac{\delta(\phi-\phi_0)}{\rho} e^{-in\phi} e^{\mp ik_{z,np}z}\, dv \\ &= (-1)^n [-s_n e_{\rho,np}(\rho_0)] e^{-in\phi_0} e^{\mp ik_{z,np}z_0} \end{aligned}, \tag{3-69}$$

if $n = 0$, the above equation reduces to

$$S^{(\rho)\pm}_{0p} = e_{\rho,0p}(\rho_0) e^{\mp ik_{z,0p}z_0}. \tag{3-70}$$

3.2.3.2 Electric Current Source for ϕ Polarization

Considering $\beta = \phi$, we get

$$\begin{aligned} S^{(\phi)\pm}_{np} &= (-1)^n \int_V (e_{\phi,np})\delta(\rho-\rho_0)\delta(z-z_0)\frac{\delta(\phi-\phi_0)}{\rho} e^{-in\phi} e^{\mp ik_{z,np}z}\, dv \\ &= (-1)^n [e_{\phi,np}(\rho_0)] e^{-in\phi_0} e^{\mp ik_{z,np}z_0} \end{aligned}, \tag{3-71}$$

if $n = 0$, the above solution reduces to

$$S^{(\phi)\pm}_{0p} = e_{\phi,0p}(\rho_0) e^{\mp ik_{z,0p}z_0}. \tag{3-72}$$

3.2.3.3
Electric Current Source for z Polarization

Considering $\beta = z$, we get

$$\begin{aligned} S_{np}^{(z)\pm} &= (-1)^n \int_V (\pm\, s_n e_{z,np})\delta(\rho-\rho_0)\delta(z-z_0)\frac{\delta(\phi-\phi_0)}{\rho}e^{-in\phi}e^{\mp ik_{z,np}z}\,dv \\ &= (-1)^n[\pm\, s_n e_{z,np}(\rho_0)]e^{-in\phi_0}e^{\mp ik_{z,np}z_0} \end{aligned}, \tag{3-73}$$

if $n = 0$, the above equation reduces to

$$S_{0p}^{(z)\pm} = \mp e_{z,0p}(\rho_0)e^{\mp ik_{z,0p}z_0}. \tag{3-74}$$

3.2.3.4
The Electric Dyadic Green's Functions

Once the parameter $S_{np}^{(\beta)\pm}$ was computed, we can calculate N_{np} by using (3-68). With these quantities, can finally complete the amplitude excitation coefficients $A_{r_0,\beta}^{\pm}$ by replacing (3-69)-(3-74) into (3-65). Then, we can obtain the modal amplitudes at the observation point via (2-80)-(2-83). As a final step, the dyadic Green's functions coefficients for the electric field due to an electric dipole source can be computed by using

$$G_{\alpha\beta}^{ee} = \sum_n \sum_p (A_{r,\beta}^{+} + A_{r,\beta}^{-})e_{\alpha,np}(\rho)e^{in\phi} \quad \text{for } \alpha = \{\rho,\phi\}, \tag{3-75}$$

and

$$G_{\alpha\beta}^{ee} = \sum_n \sum_p (A_{r,\beta}^{+} - A_{r,\beta}^{-})e_{\alpha,np}(\rho)e^{in\phi} \quad \text{for } \alpha = \{z\}. \tag{3-76}$$

The coefficients $A_{r,\beta}^{\pm}$ depend on the positions of the source and observation point. We can construct a matrix of modal source amplitudes as

$$\bar{\bar{A}}_{np}(\rho_0, z_0, \phi_0, z) = \begin{bmatrix} A_{np,\rho} & A_{np,\phi} & A_{np,z} \\ A_{np,\rho} & A_{np,\phi} & A_{np,z} \\ A_{np,\rho} & A_{np,\phi} & A_{np,z} \end{bmatrix}, \tag{3-77}$$

in the same way, we define a matrix that include only of the ρ-dependent component as

$$\bar{\bar{e}}_{np}(\rho) = \begin{bmatrix} e_{np,\rho} & e_{np,\rho} & e_{np,\rho} \\ e_{np,\phi} & e_{np,\phi} & e_{np,\phi} \\ e_{np,z} & e_{np,z} & e_{np,z} \end{bmatrix}. \tag{3-78}$$

In a compact, matrix-friendly format, the electric dyadic can be written as

$$\begin{aligned}\bar{\bar{G}}^{ee}(\mathbf{r},\mathbf{r}_0) &= \sum_n \sum_p \left[\bar{\bar{A}}^{+}_{np}(\rho_0,z_0,\phi_0,z) + \bar{\bar{A}}^{-}_{np}(\rho_0,z_0,\phi_0,z)\right]\cdot \bar{\bar{e}}_{np}(\rho)e^{in(\phi)} \\ &= \sum_n \sum_p \bar{\bar{A}}_{np}(\rho_0,z_0,\phi_0,z)\cdot \bar{\bar{e}}_{np}(\rho)e^{in(\phi)}.\end{aligned} \tag{3-79}$$

Following a procedure equivalent for the magnetic field, we show that the dyadic Green's function for the magnetic field due to an electric dipole source is given by

$$G^{he}_{\alpha\beta} = \sum_n \sum_p (A^{+}_{r,\beta} - A^{-}_{r,\beta}) h_{\alpha,np}(\rho)e^{in\phi} \quad \text{for } \alpha = \{\rho,\phi\}, \tag{3-80}$$

and

$$G^{he}_{\alpha\beta} = \sum_n \sum_p (A^{+}_{r,\beta} + A^{-}_{r,\beta}) h_{\alpha,np}(\rho)e^{in\phi} \quad \text{for } \alpha = \{z\}. \tag{3-81}$$

Again, in a compact fashion, the magnetic dyadic can be written as

$$\bar{\bar{G}}^{he}(\mathbf{r},\mathbf{r}_0) = -\sum_n \sum_p \bar{\bar{A}}_{np}(\rho_0,z_0,\phi_0,z)\cdot \bar{\bar{h}}_{np}(\rho)e^{in(\phi)}. \tag{3-82}$$

3.2.4 Magnetic Current Source

For a magnetic current source, the electromagnetic fields can be written in terms of the dyadic Green's functions

$$\mathbf{E}(\mathbf{r}) = \int \bar{\bar{G}}^{eh}(\mathbf{r},\mathbf{r}')\cdot \mathbf{M}_i(\mathbf{r}')\, d\mathbf{r}', \tag{3-83}$$

$$\mathbf{H}(\mathbf{r}) = \int \bar{\bar{G}}^{hh}(\mathbf{r},\mathbf{r}')\cdot \mathbf{M}_i(\mathbf{r}')\, d\mathbf{r}'. \tag{3-84}$$

In this way, we need to excite a magnetic point source to obtain the electric/magnetic Green's function. Following the procedure presented in the last subsections, we define $\mathbf{M}_i$ as an impulsive vector that describes a magnetic point source $\mathbf{M}_i = \hat{\beta}\delta(\mathbf{r}-\mathbf{r}_0)$, $\hat{\beta} = \{\hat{\rho},\hat{\phi},\hat{z}\}$. We compute $S^{\pm}_{np}$ for each component of the impulsive magnetic source substituting $\mathbf{M}_i$ in (3-66). Thus, we have:

3.2.4.1 Magnetic Current Source for ρ Polarization

$$\begin{aligned}S^{(\rho)\pm}_{np} &= \pm(-1)^n \int_V (h_{\rho,np})\delta(\rho-\rho_0)\delta(z-z_0)\frac{\delta(\phi-\phi_0)}{\rho}e^{-in\phi}e^{\mp ik_{z,np}z}\, dv \\ &= \pm(-1)^n h_{\rho,np}(\rho_0)e^{-in\phi_0}e^{\mp ik_{z,np}z_0}\end{aligned}, \tag{3-85}$$

if $n = 0$, the above equation reduces to

$$S_{0p}^{(\rho)\pm} = \pm h_{\rho,0p}(\rho_0) e^{\mp i k_{z,0p} z_0}. \tag{3-86}$$

3.2.4.2 Magnetic Current Source for ϕ Polarization

$$\begin{aligned} S_{np}^{(\phi)\pm} &= \mp(-1)^n \int_V (s_n h_{\phi,np}) \delta(\rho-\rho_0)\delta(z-z_0)\frac{\delta(\phi-\phi_0)}{\rho} e^{-in\phi} e^{\mp i k_{z,np} z}\, dv \\ &= \mp(-1)^n [s_n h_{\phi,np}(\rho_0)] e^{-in\phi_0} e^{\mp i k_{z,np} z_0} \end{aligned}, \tag{3-87}$$

if $n = 0$, the above expression reduces to

$$S_{0p}^{(\phi)\pm} = \pm h_{\phi,0p}(\rho_0) e^{\mp i k_{z,0p} z_0}. \tag{3-88}$$

3.2.4.3 Magnetic Current Source for z Polarization

$$\begin{aligned} S_{np}^{(z)\pm} &= (-1)^n \int_V (-h_{z,np}) \delta(\rho-\rho_0)\delta(z-z_0)\frac{\delta(\phi-\phi_0)}{\rho} e^{-in\phi} e^{\mp i k_{z,np} z}\, dv \\ &= (-1)^n [-h_{z,np}] e^{-in\phi_0} e^{\mp i k_{z,np} z_0} \end{aligned}, \tag{3-89}$$

if $n = 0$, the above solution reduces to

$$S_{0p}^{(z)\pm} = -h_{z,0p} e^{\mp i k_{z,0p} z_0}. \tag{3-90}$$

3.2.4.4 The Magnetic Dyadic Green's Functions

Finally, from the above results for the magnetic current source, we can use the equivalent equations (3-75)-(3-82) to calculate the dyadic electric/magnetic Green's functions due to a magnetic point source.

Once all dyadics $\bar{\bar{G}}^{ee}(\mathbf{r},\mathbf{r}_0)$, $\bar{\bar{G}}^{he}(\mathbf{r},\mathbf{r}_0)$, $\bar{\bar{G}}^{eh}(\mathbf{r},\mathbf{r}_0)$, and $\bar{\bar{G}}^{hh}(\mathbf{r},\mathbf{r}_0)$ are determined for all the discrete points $\mathbf{r}_0$ inside the scatterer volume, we can compute the fields at $\mathbf{r}$ via BA by using (3-41) and (3-42). For a EBA aproach we should calculate the scattering tensors $\bar{\bar{\Lambda}}^{\alpha\beta}(\mathbf{r})$ defined in (3-55) and (3-58). The computation of these tensors requires a volumetric (3D) integral for arbitrary scatterers. However, some simplifications can be considered for specific symmetric examples, as it will be shown in the next section.

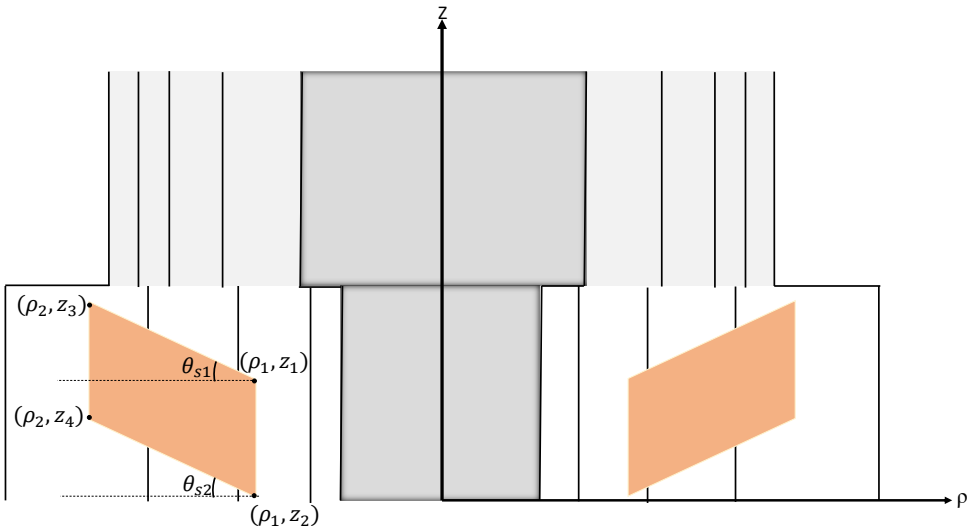

Figure 3.2: Scatterer with azimuthal symmetry.

3.2.4.5 EBA for Objects with Azimuthal Symmetry

Consider a tilted scatterer with azimuthal symmetry, as illustrated in Figure 3.2. The volume integrals in (3-48)-(3-51) become surface integrals, i.e.,

$$\bar{\bar{S}}^{ee}(\mathbf{r}) = -2i\pi\omega \int_{\rho_1}^{\rho_2} \int_{z_{start}}^{z_{end}} \bar{\bar{G}}^{ee}(\mathbf{r}, \mathbf{r}_0) \cdot \Delta\bar{\bar{\epsilon}}\, \rho\, d\rho\, dz_0, \tag{3-91}$$

$$\bar{\bar{S}}^{eh}(\mathbf{r}) = -2i\pi\omega \int_{\rho_1}^{\rho_2} \int_{z_{start}}^{z_{end}} \bar{\bar{G}}^{eh}(\mathbf{r}, \mathbf{r}_0) \cdot \Delta\bar{\bar{\mu}}\, \rho\, d\rho\, dz_0, \tag{3-92}$$

$$\bar{\bar{S}}^{he}(\mathbf{r}) = -2i\pi\omega \int_{\rho_1}^{\rho_2} \int_{z_{start}}^{z_{end}} \bar{\bar{G}}^{he}(\mathbf{r}, \mathbf{r}_0) \cdot \Delta\bar{\bar{\epsilon}}\, \rho\, d\rho\, dz_0, \tag{3-93}$$

$$\bar{\bar{S}}^{hh}(\mathbf{r}) = -2i\pi\omega \int_{\rho_1}^{\rho_2} \int_{z_{start}}^{z_{end}} \bar{\bar{G}}^{hh}(\mathbf{r}, \mathbf{r}_0) \cdot \Delta\bar{\bar{\mu}}\, \rho\, d\rho\, dz_0, \tag{3-94}$$

where

$$z_{start} = z_1 - (\rho - \rho_1)\tan(\theta_{s1}), \tag{3-95}$$

$$z_{end} = z_2 - (\rho - \rho_1)\tan(\theta_{s2}), \tag{3-96}$$

$$\theta_{s1} = \arctan\left(\frac{z_1 - z_3}{\rho_2 - \rho_1}\right), \tag{3-97}$$

$$\theta_{s2} = \arctan\left(\frac{z_2 - z_4}{\rho_2 - \rho_1}\right), \tag{3-98}$$

by using (3-79) in (3-91) we get the scattering coefficients

$$S^{ee}_{\alpha\beta}(\mathbf{r}) = -2i\pi\omega e^{in\phi}\int_{\rho_1}^{\rho_2} e_{\alpha,np}(\rho)\int_{z_{start}}^{z_{end}}\sum_n\sum_p (A^+_{r,np,\beta} + A^-_{r,np,\beta})\Delta\epsilon_{\alpha\beta}\,\rho\,d\rho\,dz_0. \tag{3-99}$$

In order to simplify the surface integral in (3-99) as a line integral we substitute (2-89) in (2-80) and we obtain

$$\begin{aligned}\bar{A}^+_r = {} & \bar{\bar{P}}^{\pm}_{\tilde{n}}(z^{\mp}_{\tilde{n}}, z_r)\bar{\bar{\bar{T}}}_{m\tilde{n}}\bar{\bar{\bar{M}}}^{\pm}_m(z^{\pm}_m) \\ & [\bar{\bar{P}}^+_m(z_0, z^+_m)\bar{A}^+_{r_0} + \bar{\bar{P}}^+_m(z^+_{m-1}, z^+_m)\bar{\bar{\bar{R}}}_{m,m-1}\bar{\bar{P}}^-_m(z_0, z^+_{m-1})\bar{A}^-_{r_0}],\end{aligned} \tag{3-100}$$

or what is the same

$$\begin{aligned}\bar{A}^+_r = {} & \bar{\bar{P}}^{\pm}_{\tilde{n}}(z^{\mp}_{\tilde{n}}, z_r)\bar{\bar{\bar{T}}}_{m\tilde{n}}\bar{\bar{\bar{M}}}^{\pm}_m(z^{\pm}_m)\bar{\bar{e}}^{\,ik_{zm}(z^+_m - z_0)}\bar{A}^+_{r_0} \\ & + \bar{\bar{P}}^{\pm}_{\tilde{n}}(z^{\mp}_{\tilde{n}}, z_r)\bar{\bar{\bar{T}}}_{m\tilde{n}}\bar{\bar{\bar{M}}}^{\pm}_m(z^{\pm}_m)\bar{\bar{P}}^+_m(z^+_{m-1}, z^+_m)\bar{\bar{\bar{R}}}_{m,m-1}\bar{\bar{e}}^{\,ik_{zm}(z^+_{m-1} - z_0)}\bar{A}^-_{r_0},\end{aligned} \tag{3-101}$$

where $\bar{\bar{e}}$ is a diagonal matrix whose ith diagonal element corresponds to the ith eigenvalue (k_z value). The double integral for the vector $\bar{A}^+_r$ is given by

$$\begin{aligned}\int_{\rho_1}^{\rho_2}\int_{z_{start}}^{z_{end}} \bar{A}^+_r\,\rho\,d\rho\,dz_0 = {} & \bar{\bar{P}}^{\pm}_{\tilde{n}}(z^{\mp}_{\tilde{n}}, z_r)\int_{\rho_1}^{\rho_2}\rho\,\bar{\bar{\bar{T}}}_{m\tilde{n}}\bar{\bar{\bar{M}}}^{\pm}_m(z^{\pm}_m) \\ & \int_{z_{start}}^{z_{end}}\bar{\bar{e}}^{ik_{zm}(z^+_m - z_0)}\bar{A}^+_{r_0}\,d\rho\,dz_0 + \\ & \bar{\bar{P}}^{\pm}_{\tilde{n}}(z^{\mp}_{\tilde{n}}, z_r)\int_{\rho_1}^{\rho_2}\rho\,\bar{\bar{\bar{T}}}_{m\tilde{n}}\bar{\bar{\bar{M}}}^{\pm}_m(z^{\pm}_m)\bar{\bar{P}}^+_m(z^+_{m-1}, z^+_m)\bar{\bar{\bar{R}}}_{m,m-1} \\ & \int_{z_{start}}^{z_{end}}\bar{\bar{e}}^{\,ik_{zm}(z^+_{m-1} - z_0)}\bar{A}^-_{r_0}\,d\rho\,dz_0.\end{aligned} \tag{3-102}$$

The arguments of the integrals over z are given by

$$\bar{\bar{e}}^{\,ik_{zm}(z^+_m - z_0)}\bar{A}^+_{r_0} = \bar{D}_1\cdot\bar{D}_2\cdot\bar{A}^+_{r_0}, \tag{3-103}$$

$$\bar{D}_1 = \mathrm{diag}\,[\bar{\bar{e}}^{\,ik_{zm}z^+_m}], \tag{3-104}$$

$$\bar{D}_2 = \mathrm{diag}\,[\bar{\bar{e}}^{\,ik_{zm}(-z_0)}], \tag{3-105}$$

$$\bar{\bar{e}}^{\,ik_{zm}(z^+_{m-1} - z_0)}\bar{A}^-_{r_0} = \bar{D}_3\cdot\bar{D}_2\cdot\bar{A}^-_{r_0}, \tag{3-106}$$

$$\bar{D}_3 = \mathrm{diag}\,[\bar{\bar{e}}^{\,ik_{zm}z^+_{m-1}}], \tag{3-107}$$

$$\tag{3-108}$$

substituting (3-103) and (3-106) in (3-102) we get

$$\int_{\rho_1}^{\rho_2}\int_{z_{start}}^{z_{end}} \bar{A}_r^+\,\rho\,d\rho\,dz_0 = \bar{\bar{P}}_{\tilde{n}}^{\pm}(z_{\tilde{n}}^{\mp},z_r)\int_{\rho_1}^{\rho_2}\rho\,\bar{\bar{\bar{T}}}_{m\tilde{n}}\bar{\bar{\bar{M}}}_m^{\pm}(z_m^{\pm})\bar{A}_{r_0}^+\cdot\bar{D}_1\cdot \int_{z_{start}}^{z_{end}}\bar{D}_2\,d\rho\,dz_0 + \bar{\bar{P}}_{\tilde{n}}^{\pm}(z_{\tilde{n}}^{\mp},z_r)\int_{\rho_1}^{\rho_2}\rho\,\bar{\bar{\bar{T}}}_{m\tilde{n}}\bar{\bar{\bar{M}}}_m^{\pm}(z_m^{\pm})\bar{\bar{P}}_m^{+}(z_{m-1}^{+},z_m^{+})\bar{\bar{\bar{R}}}_{m,m-1}\bar{A}_{r_0}^-\cdot\bar{D}_3\cdot \int_{z_{start}}^{z_{end}}\bar{D}_2\,d\rho\,dz_0. \quad (3\text{-}109)$$

The z integral is analytic, and it is given by

$$\int_{z_{start}}^{z_{end}}\bar{D}_2\,dz_0 = \frac{\bar{e}^{\,-ik_z z_0}\big|_{z_{start}}^{z_{end}}}{-i\bar{k}_z}, \quad (3\text{-}110)$$

finally (3-109) is simplified by the following linear integral

$$\int_{\rho_1}^{\rho_2}\int_{z_{start}}^{z_{end}} \bar{A}_r^+\,\rho\,d\rho\,dz_0 = \frac{\bar{\bar{P}}_{\tilde{n}}^{\pm}(z_{\tilde{n}}^{\mp},z_r)}{-i\bar{k}_z}\int_{\rho_1}^{\rho_2}\rho\,\bar{\bar{\bar{T}}}_{m\tilde{n}}\bar{\bar{\bar{M}}}_m^{\pm}(z_m^{\pm})\bar{A}_{r_0}^+\cdot\bar{D}_1\cdot \left(\bar{e}^{\,-ik_z(z_2-(\rho-\rho_1)\tan(\theta_{s2}))}-\bar{e}^{\,-ik_z(z_1-(\rho-\rho_1)\tan(\theta_{s1}))}\right)d\rho + \frac{\bar{\bar{P}}_{\tilde{n}}^{\pm}(z_{\tilde{n}}^{\mp},z_r)}{-i\bar{k}_z}\int_{\rho_1}^{\rho_2}\rho\,\bar{\bar{\bar{T}}}_{m\tilde{n}}\bar{\bar{\bar{M}}}_m^{\pm}(z_m^{\pm})\bar{\bar{P}}_m^{+}(z_{m-1}^{+},z_m^{+})\bar{\bar{\bar{R}}}_{m,m-1}\bar{A}_{r_0}^-\cdot\bar{D}_3\cdot \left(\bar{e}^{\,-ik_z(z_2-(\rho-\rho_1)\tan(\theta_{s2}))}-\bar{e}^{\,-ik_z(z_1-(\rho-\rho_1)\tan(\theta_{s1}))}\right)d\rho. \quad (3\text{-}111)$$

An equivalent procedure can be followed to find $\int_{\rho_1}^{\rho_2}\int_{z_{start}}^{z_{end}} A_r^-\,\rho\,d\rho\,dz_0$.

3.2.5 Induced Voltage at the Receivers

The induced voltage at the RXs can be calculated by the expression (2-112). If the total fields have a contribution of a scattered field by an asymmetric body, an analytical solution similar to that of coil antennas immersed in symmetric cylindrical layers in (2-120) is not possible [5]. Thereby the coil perimeter must be discretized for solving (2-112) numerically.

3.3 Summary of Chapter 3

The BA, EBA-based methods proposed in this chapter to compute the induced voltages at the receiver can be summarized by the following procedure:

1. Calculate the background electromagnetic fields at the RX ($\mathbf{E}_b(\mathbf{r})$) applying MMT-based method presented in Chapter 2.

2. Discretize the scatterer and then to compute the electric dyadics $\bar{\bar{G}}^{ee}(\mathbf{r}, \mathbf{r}_0)$ and $\bar{\bar{G}}^{eh}(\mathbf{r}, \mathbf{r}_0)$ for each point describing the scatterer volume.

3. For BA approach:

   – Calculate the background field at each discrete scatterer point ($\mathbf{E}_b(\mathbf{r}_0)$) using MMT-based method, and then compute the total electric field at RX ($\mathbf{E}(\mathbf{r})$) via (3-41).
   – Calculate the received voltage at the RX LWD sensor via (2-112).

4. For EBA approach:

   – Calculate the scattering tensors $\bar{\bar{\Lambda}}^{ee}(\mathbf{r})$ and $\bar{\bar{\Lambda}}^{eh}(\mathbf{r})$ with the aid of the volumetric integration in (3-48)-(3-51)
   – Compute the total electromagnetic fields at each point of the volumetric scatterer ($\mathbf{r} \rightarrow \mathbf{r_0}$) via (3-52).
   – Calculate the total electric fields at RX re-radiating the field computed inside the scatterer with help of (3-61).
   – Calculate the voltage received (at the LWD sensor) in view of both background and scattered electromagnetic fields.

4
Analysis of Well-Logging Sensors in Non-Symmetric Formations

A numerical algorithm of the Born approximation formalism presented in Chapter 3 was implement in a Fortran 90 code. As a validation procedure, in a first step, we will model objects with azimuthal symmetry. In this way, we can compare the BA-based versus the MMT results. Notice that the model using the MMT presented in Chapter 2 is considered as the *exact* solution for LWD tools inside ϕ-symmetric media. The validation will allow us to explore our formulation by studying its accuracy as a function of the scatterer conductivity and size. Later, we will use the BA formalist to modeling asymmetric and anisotropic scenarios. For all the cases presented in this chapter, the LWD tool operates at 2 MHz, and it consists of one transmitting (TX) and one receiving (RX) coil antennas, that move axially through the formations inside a borehole. The mandrel radius is fixed in $\rho_m = 4$ in (where 1 in= 0.0254 m), and the borehole radius is equal to $\rho_b = 5$ in. The TX is carrying 1 A current, and the geophysical formations are truncated radially by a perfect electric conductor boundary condition at $\rho = 60$ in. This allows us to mimic a radially-unbounded domain effectively.

4.1
Isotropic and Symmetric Invasion

4.1.1
Case Study 1 - Electric Conductivity Variations

First, consider an isotropic geophysical formation comprising a cylindrical layered background medium with two vertical and two radial layers, as illustrated in Figure 4.1. TX is placed at $z = z_T$, while RX at $z = z_T + 30$ in. The borehole is filled with a material characterized by a conductivity of $\sigma = 5 \times 10^{-4}$ S/m and the formations 1 and 2 with $\sigma = 5$ S/m and $\sigma = 1$ S/m respectively. The whole media present relative permittivity $\epsilon_r = 1$ and relative permeability $\mu_r = 1$. Consider now that the formation two is invaded by a symmetric and isotropic layer with a conductivity of σ_s, thickness $z_s = 10$ in, and radius $\rho_s = 10$ in. We will calculate the received voltage at RX for

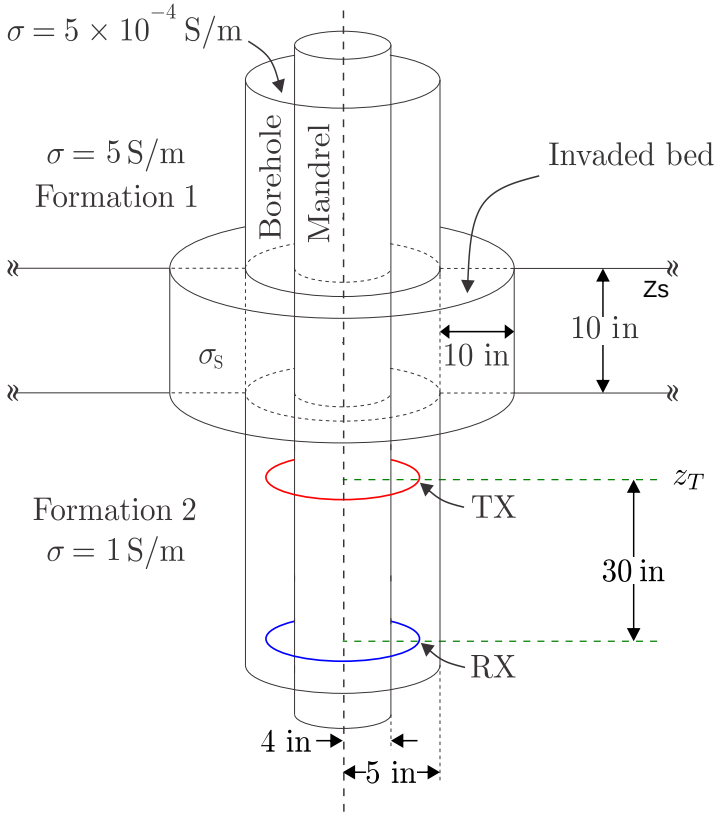

Figure 4.1: Symmetric invasion inside a layered cylindrical medium.

variations from $\sigma_s = 0.1$ S/m to $\sigma_s = 5$ S/m. Note that in symmetric invasion problems, only the azimuthal harmonic $n = 0$ is required for getting the complete field solution.

The Figure 4.2 and Figure 4.3 show the phase and amplitude of the voltage at RX. The results are compared with the MMT-based method presented in [21]. Figure 4.2 shows that σ_s has a significant effect on the RX phase voltage, since we get variations of until $\Delta_{|V_{RX}|} \approx 50°$ when we compare the cases $\sigma_s = 0.1$ S/m and $\sigma_s = 5$ S/m. Contrary to phase, in terms of amplitude, σ_s does not imply a critical variation. Observing BA results, we perceive that our method better performs in terms of phase. The phase starts to diverge from the reference method when $\sigma_s = 5$ S/m, while in terms of amplitude, it begins to diverge when $\sigma_s = 2.5$ S/m.

4.1.2 Case Study 2 - Size Variations

Subsequently, we will evaluate the voltage at RX perturbed by a ticker invasion of $z_s = 20$ in, for the cases $\sigma_s = 0.1$ S/m and $\sigma = 1.5$ S/m. We maintain all the remaining parameters, as presented in the above example.

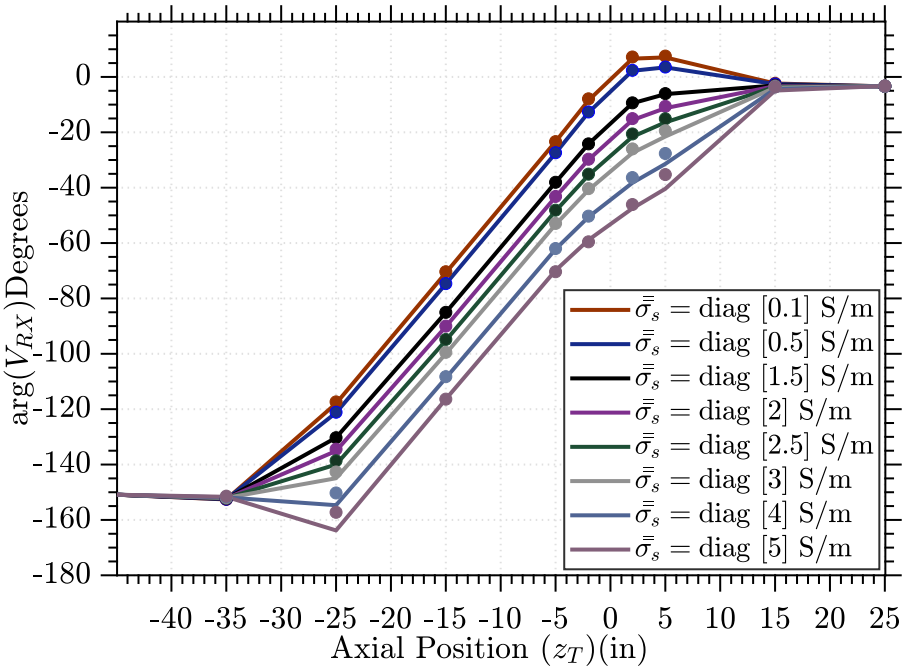

Figure 4.2: Phase voltage at RX for σ_s variations. The lines represent the results obtained by BA approximation and the symbols by the MMT-based method.

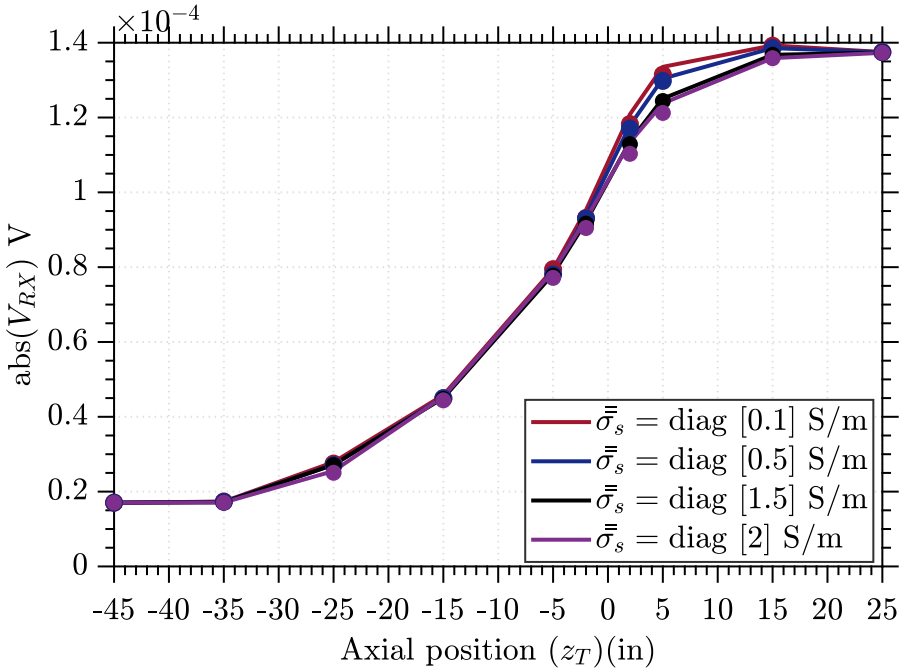

Figure 4.3: Amplitude voltage at RX for σ_s variations. The lines represent the results obtained by BA approximation and the symbols by the MMT-based method.

Figure 4.4 and Figure 4.5 show the phase and amplitude of the received voltage, respectively. Even doubling the invasion thickness, we got a very accurate phase result. Concerning to the amplitude, we can see a slight deviation when $\sigma_s = 0.1$ S/m. It was not observed when we synthesized the smaller invasion, then this result is due to the increase in the scatterer dimension, as expected in

the perturbational theory. In the case $\sigma_s = 1.5$ S/m we have a good convergence in amplitude and phase. This is due to that the medium where the invasion is embedded has a conductivity $\sigma = 1$ S/m therefore the difference between the background medium and the invaded zone is less than in the case $\sigma_s = 0.1$ S/m.

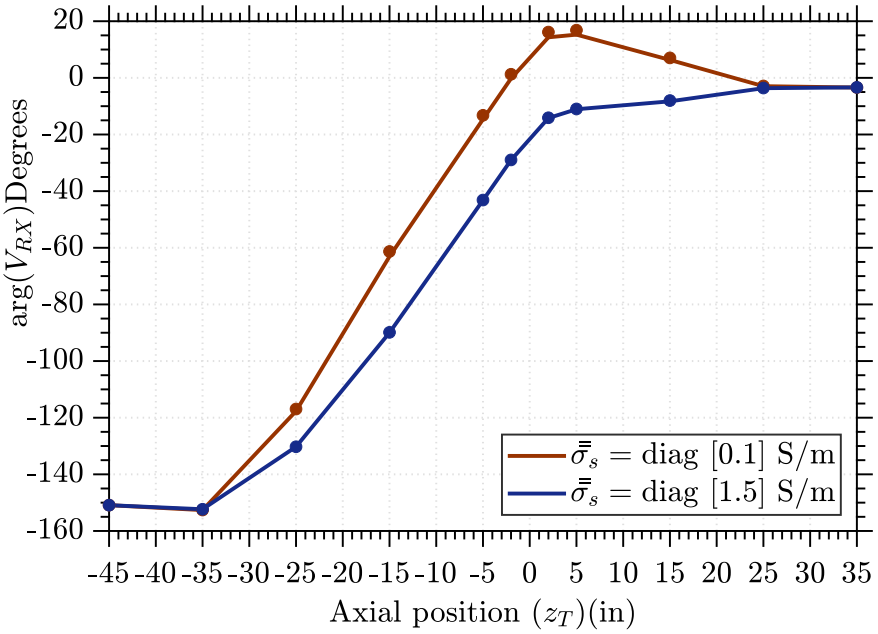

Figure 4.4: Phase voltage at RX due to a symmetric invasion with $z_s = 20$ in. The lines represent the results obtained by BA approximation and the symbols by the MMT-based method.

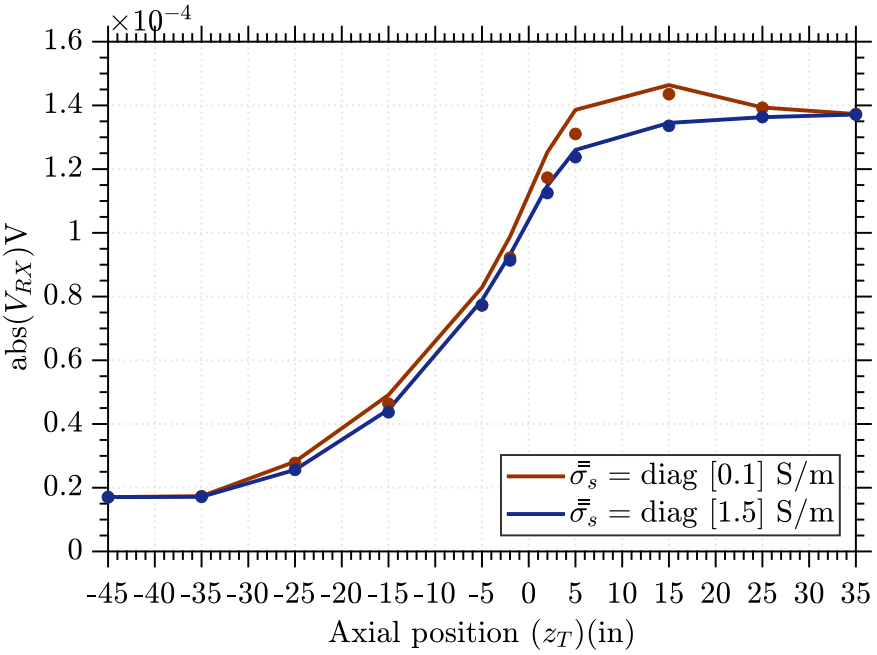

Figure 4.5: Amplitude voltage at RX due to a symmetric invasion with $z_s = 20$ in. The lines represent the results obtained by BA approximation and the symbols by the MMT-based method.

4.1.3
Case Study 3 - Magnetic Permeability Variations

Referring to variations in the scatterer magnetic profile, consider now that the formation two is invaded by a symmetric and isotropic layer with relative permeability μ_s, conductivity $\sigma_s = 1$ S/m, and thickness $z_s = 10$ in. We will compute the received voltage at RX for two cases: $\mu_s = 1.2$, and $\mu_s = 1.3$. The background parameters are similar to those of the cases above. Figure 4.6 and Figure 4.7 illustrate the voltage behaviour at RX. Like showed in Figure 4.7, the amplitude voltage is more sensitive to permeability variations than to conductivity variations. Since a difference of 20% in μ_s concerning to the background media implies a considerable variation in terms of amplitude. We can observe too that the horn effect is more accentuated. BA approximation is not much efficient for modeling scatterer magnetic profiles with large $\Delta\mu$, as shown in Figure 4.7, a difference of 30% makes the amplitude voltage-solution begins to diverge from the reference technique. This difficulty is because the method is more precise in terms of phase, as stated above.

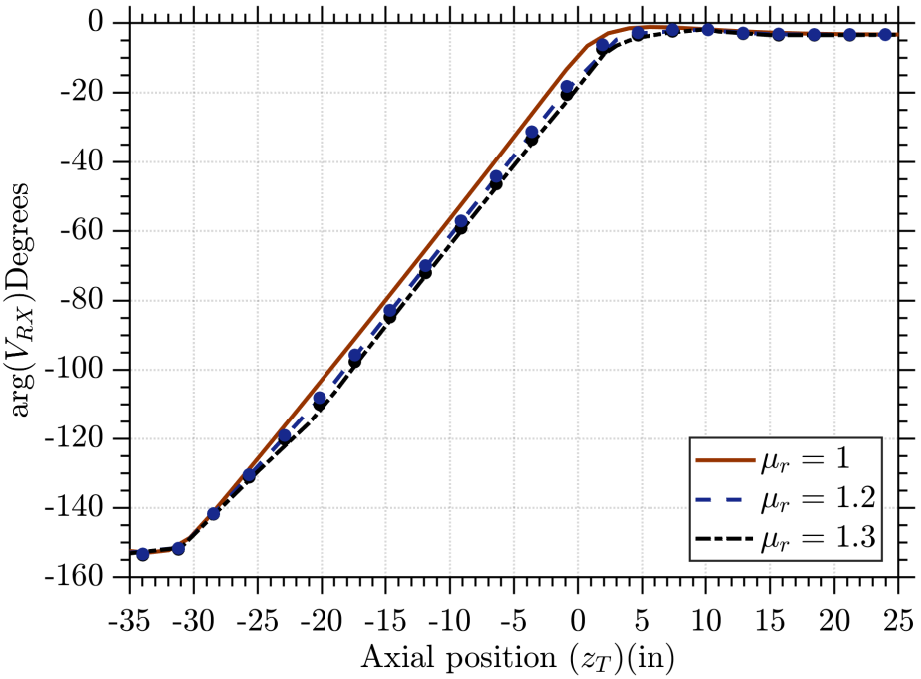

Figure 4.6: Phase voltage at RX due to permeability variations. The lines represent the results obtained by BA approximation and the symbols by the MMT-based method.

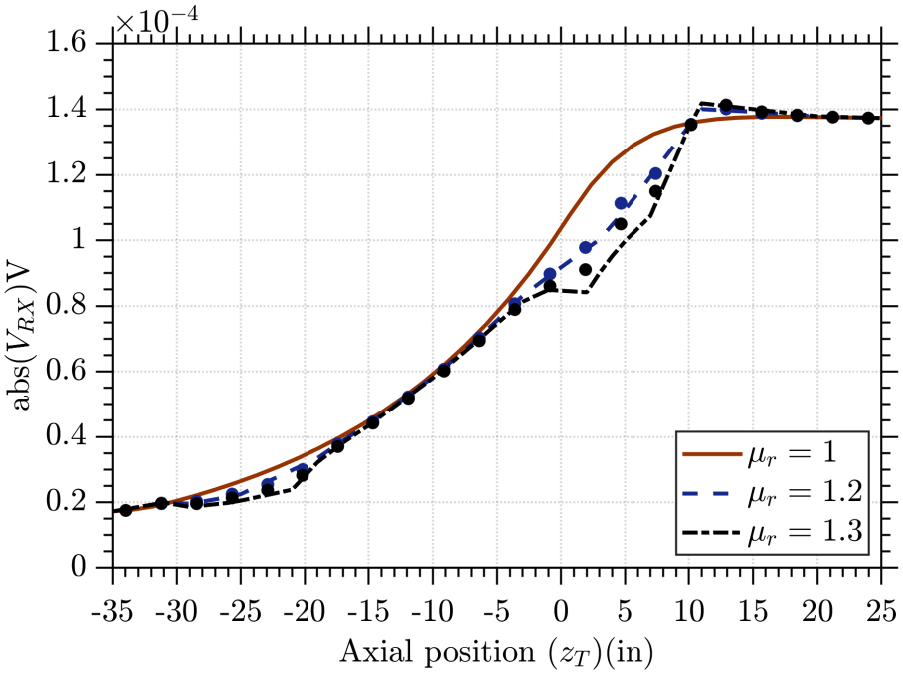

Figure 4.7: Amplitude voltage at RX due to permeability variations. The lines represent the results obtained by BA approximation and the symbols by the MMT-based method.

4.2 Anisotropic and Symmetric Invasion

In the next step, the geophysical formation is invaded by anisotropic-symmetric scatterers. The BA-based method does not have any restriction of scatterer isotropy, unlike the reference method, which is restricted to uni-axial materials. Therefore, for validation purpose, we evaluate two uniaxial-symmetric scatterers with $\bar{\bar{\sigma}}_s = \text{diag}\,[0.5, 0.5, 2]$ S/m and $\bar{\bar{\sigma}}_s = \text{diag}\,[2, 2, 0.5]$ S/m. All the background parameters are maintained as in Section 4.1. Then, we include a biaxial material with a conductivity slightly different from uniaxial cases, i.e. $\bar{\bar{\sigma}}_s = \text{diag}\,[0.5, 1.5, 2]$ S/m. Figure 4.8 and Figure 4.9 show the amplitude and phase of the received voltages at RX perturbed by the described scatterers. The uniaxial results show good accuracy with respect to the reference method, and the biaxial result is between the uniaxial cases like expected theoretically.

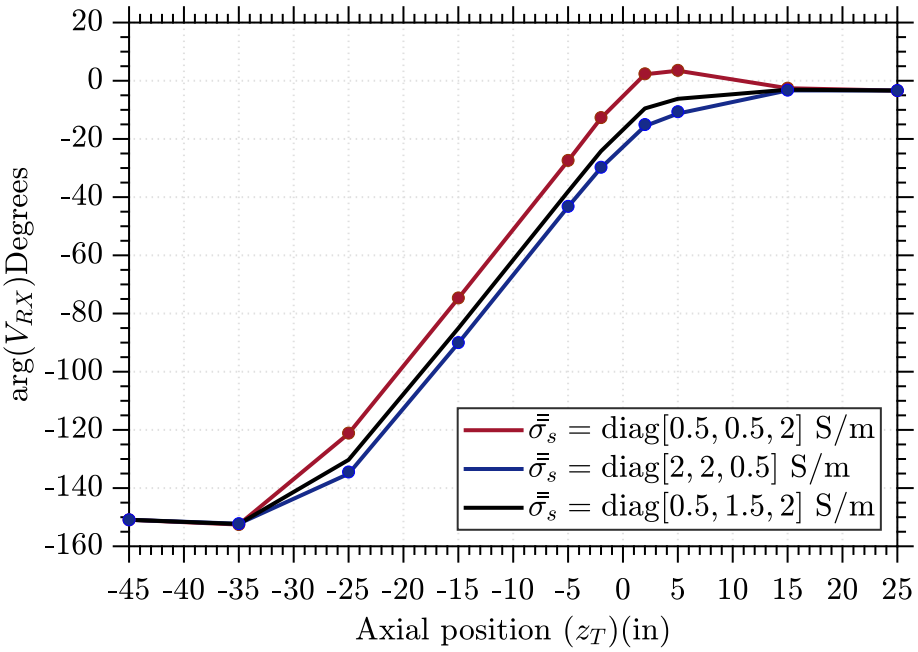

Figure 4.8: Phase voltage at RX due to anisotropic symmetric scatterers. The lines represent the results obtained by BA approximation and the symbols by the MMT-based method.

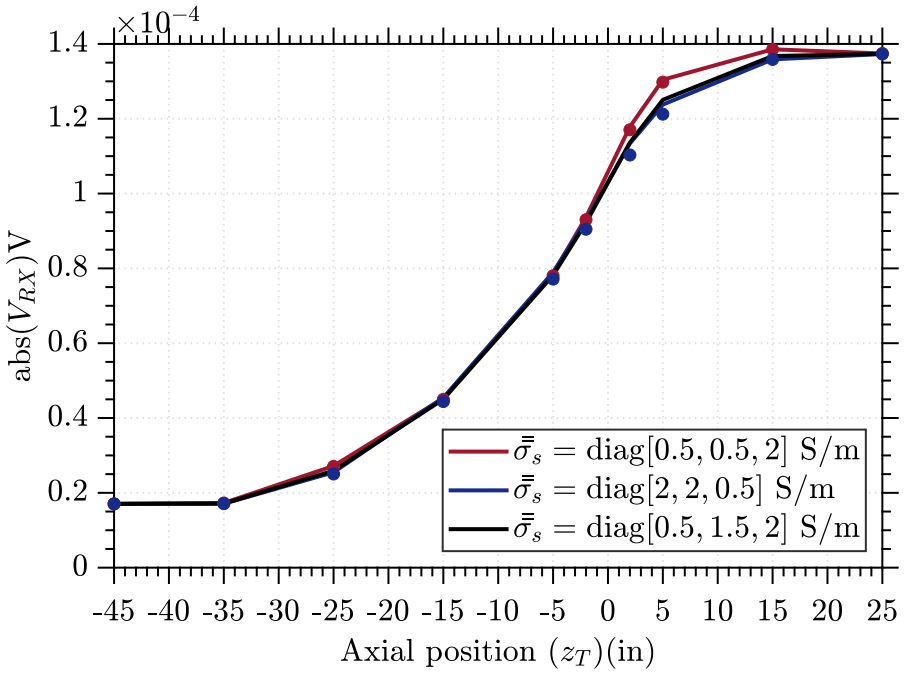

Figure 4.9: Amplitude voltage at RX due to anisotropic symmetric scatterers. The lines represent the results obtained by BA approximation and the symbols by the MMT-based method.

4.3 Non-Symmetrical Invasion

In the following, we explore the field behavior and the induced voltage at the RXs due to an asymmetric invasions around the borehole.

4.3.1 Case Study 1

Consider a geophysical formation formed by a cylindrical layered background medium and an asymmetric invasion. The background medium has two vertical and three radial layers similar to that illustrated in Figure 4.10. This axis-symmetric configuration was considered before in [21,63,64] for modeling a LWD tool operating at 2 MHz. This tool consists of one TX and two RXs horizontal coil antennas. RX_1 and RX_2 are placed 30 in and 24 in away from TX, respectively.

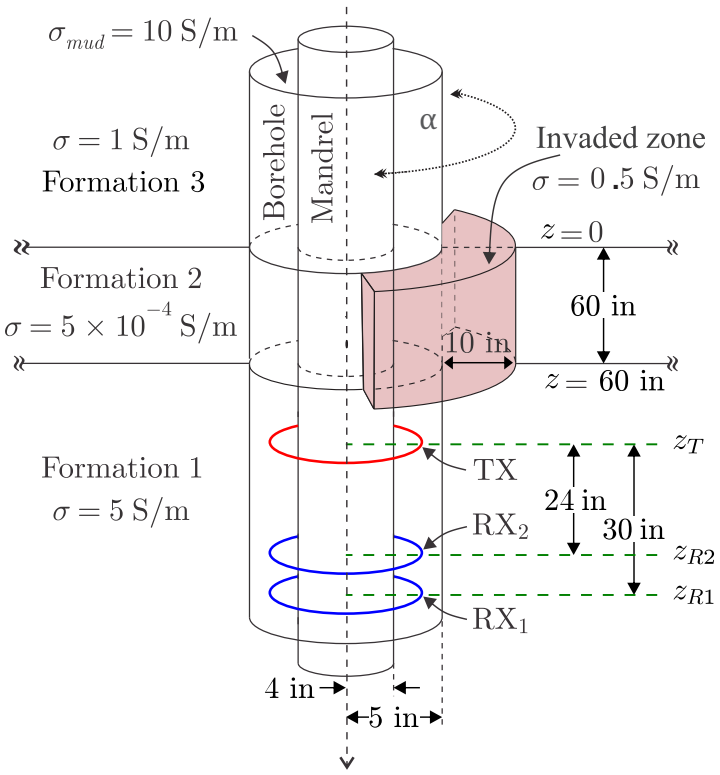

Figure 4.10: Asymmetric invasion inside a layered cylindrical medium.

We present a scenario where the borehole is filled with saltwater with a conductivity of $\sigma = 10$ S/m, and the array of antennas moves through a 60-in bed layer (formation 2) with $\sigma = 5 \times 10^{-4}$ S/m. The formations below and above the bed layer are characterized by the conductivities $\sigma = 5$ S/m and $\sigma = 1$ S/m, respectively. The whole media presents relative permittivity $\epsilon_r = 1$ and relative permeability of $\mu_r = 1$. As said before, due to the antenna geometry, only fields with azimuthal harmonic index $n = 0$ will be excited by the TX. Consider now that the formation 2 presents a non-symmetric invasion zone with a conductivity of $\sigma = 0.5$ S/m, extending over a cylindrical sector of 10-in in the radial direction and defined by the azimuthal angle α as depicted in Figure 4.10. The Figure 4.11 and Figure 4.12 show the amplitude

and phase ratio of the received voltages at RX_1 and RX_2 for three invasion cases: $\alpha = 0°, 180°, 360°$. For $\alpha = 0°$ there is no invasion, and the total voltage correspond only to the background field counterpart i.e., $\mathbf{E}_s = \mathbf{0}$. For $\alpha = 360°$, the problem becomes symmetrical again, but now we have $\mathbf{E}_s \neq \mathbf{0}$.

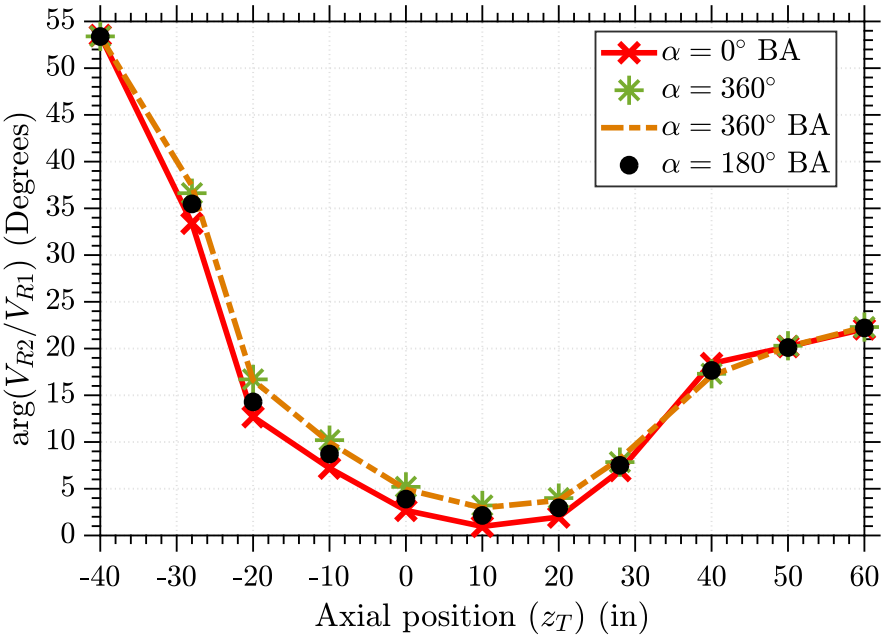

Figure 4.11: Phase difference for a moving LWD tool traversing a bed layer with a non-invaded, a symmetrical, and a non-symmetrical invaded zones. Our results are indicated by the label BA.

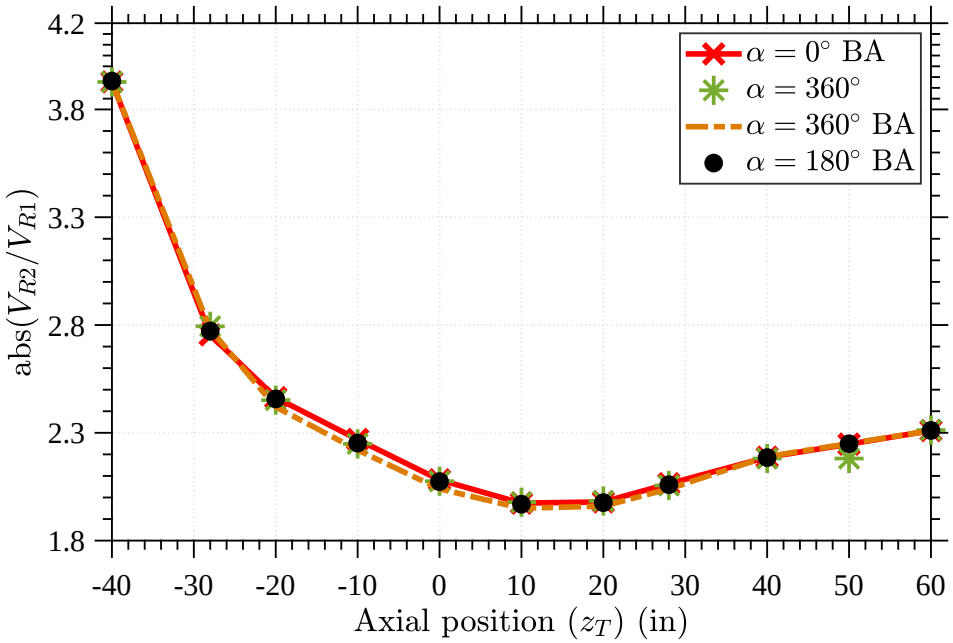

Figure 4.12: Voltage ratio amplitude for a moving LWD tool traversing a bed layer with a non-invaded, a symmetrical, and a non-symmetrical invaded zones. Our results are indicated by the label BA.

We compare this case with the results presented in [21,63,64], and we have observed very good agreement. For $\alpha = 180°$, the problem is non-symmetrical, as presented in Figure 4.10. Our voltage results in Figure 4.11 and Figure 4.12 are between the extrema $\alpha = 0°$ and 360°, as expected, and this indicates the correctness of presented formulation. Our method has employed $P = 45$ radial modes and $N = 1$ azimuthal modes (the sum of $n = 0, -1, 1$) for the case $\alpha = 180°$. For the cases $\alpha = 0°$ and $\alpha = 360°$ we considered $P = 45$ and $N = 0$. Note that in those symmetric invasions only the azimuthal harmonic $n = 0$ is required.

Although the analyzed scenarios present high conductivity contrasts between the invaded zone ($\sigma = 0.5$ S/m) and the background ($\sigma = 5 \times 10^{-4}$ S/m) in formation 2, it does not imply large variations for the amplitude of V_{R1}/V_{R2}. Then, we focus on the analysis of phase voltage variation. At $z_T = -10$ in, phase results are shown in Figure 4.13 as a function of the azimuthal invasion angle α. In Figure 4.14 we show the corresponding voltage phases at RX_1 and RX_2, where a variation in the range from 16° to 30°, and 8° to 20° are observed, respectively. Note that for $\alpha = 0°$ the invasion is absent, while for $\alpha = 360°$ the invasion becomes symmetric.

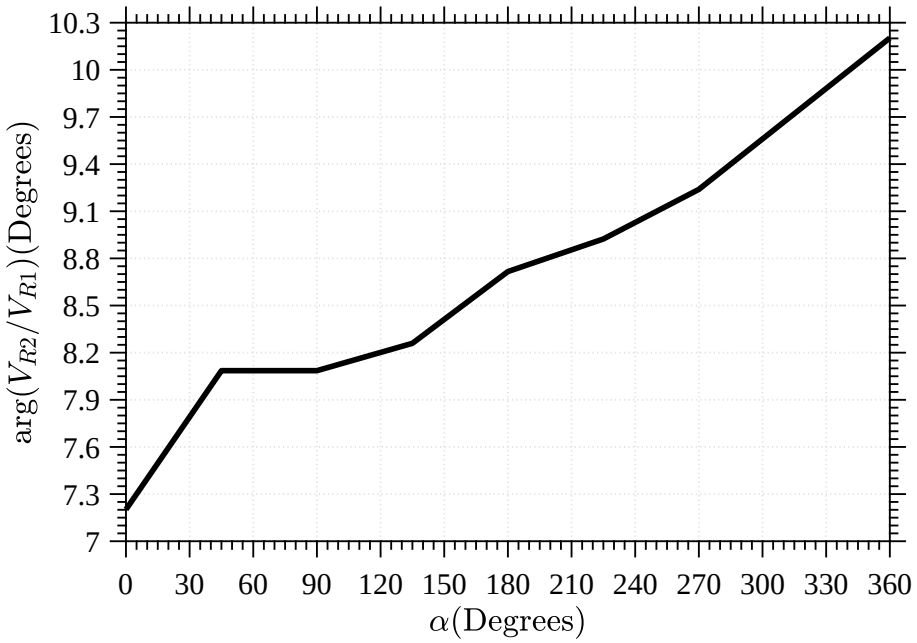

Figure 4.13: Phase difference for triaxial LWD tool at $z_T = -10$ in as function of the azimuthal invasion angle α.

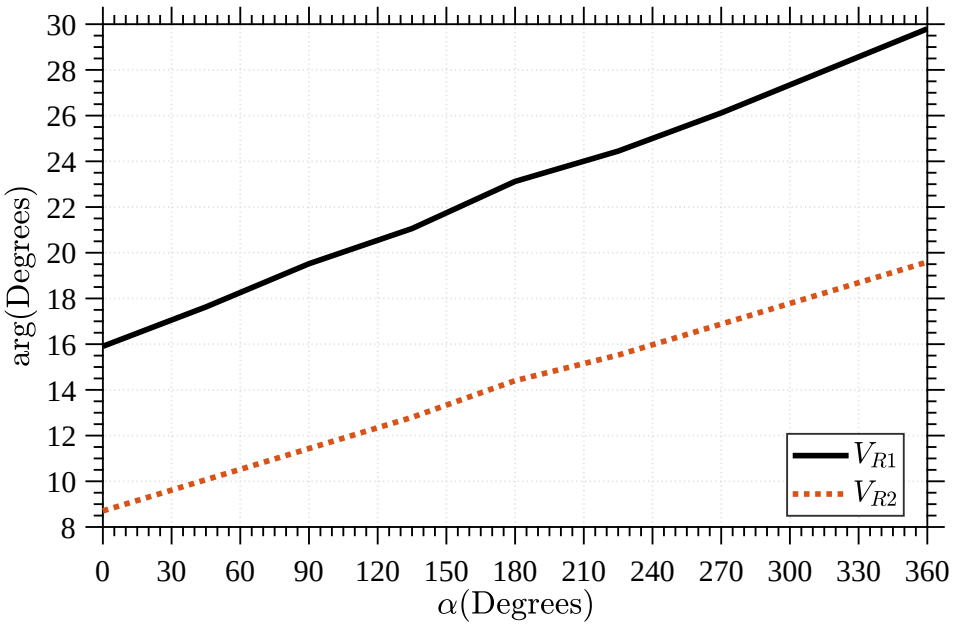

Figure 4.14: Phase voltage at RX_1 and RX_2 for $z_T = -10$ in as function of the azimuthal invasion angle α.

In order to obtain a deeper knowledge about the electric field behavior along the coil antennas ($0° < \phi < 360°$) and its relation with α, Figure 4.15 and Figure 4.16 show the phase and amplitude of E_ϕ for different invasions at $z_T = -10$ in.

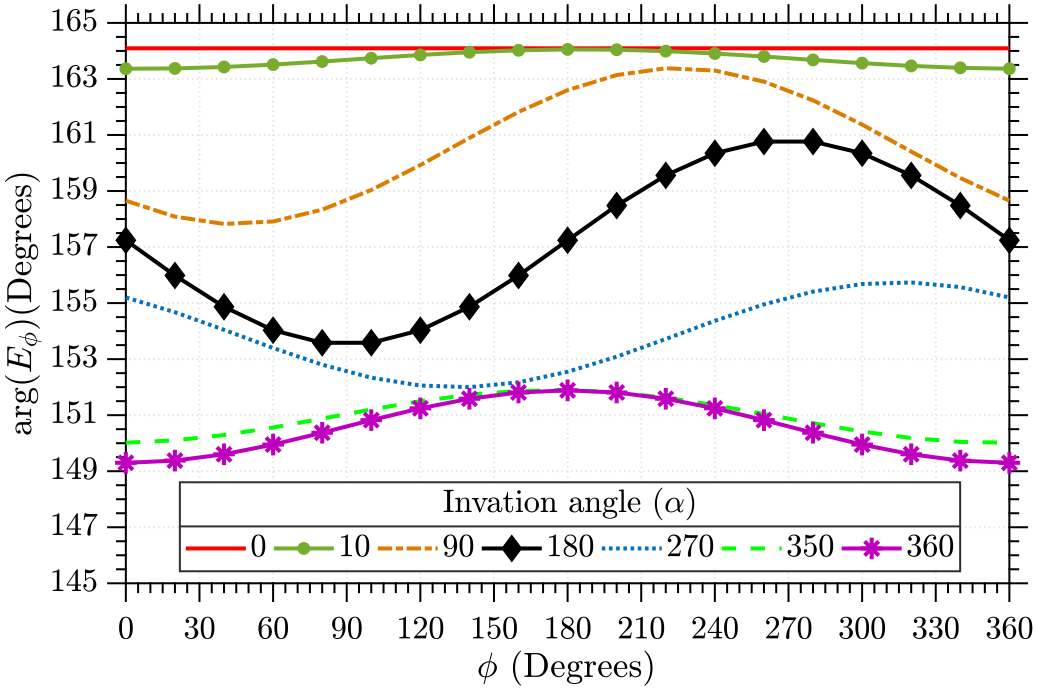

Figure 4.15: E_ϕ phase for different invaded zones at the axial position $z_T = -10$ in.

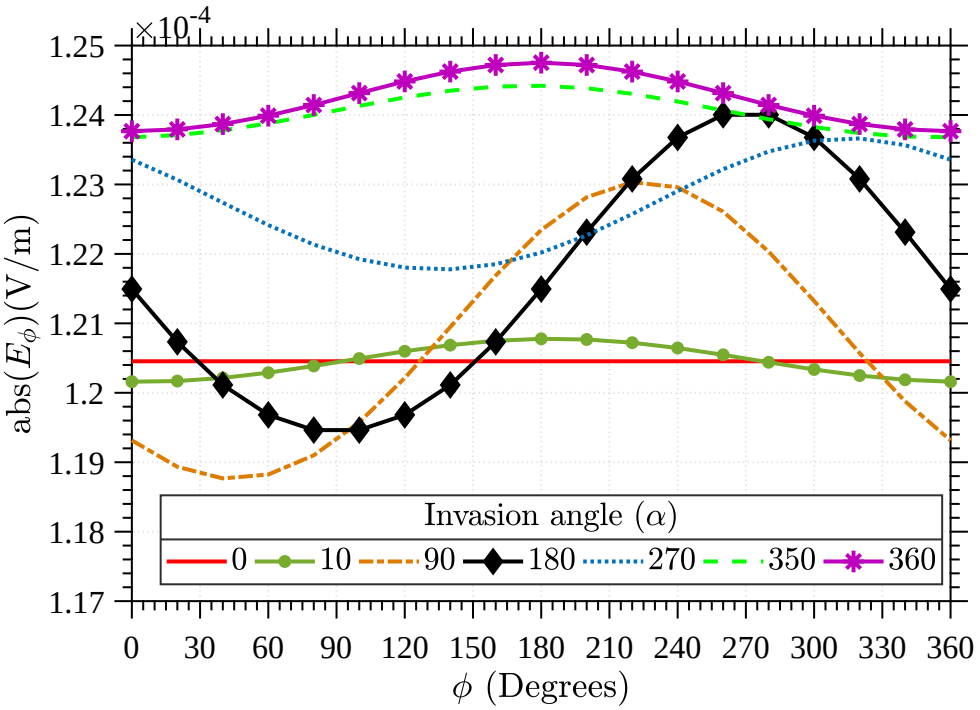

Figure 4.16: E_ϕ amplitude for different invaded zones at the axial position $z_T = -10$ in.

As said above, we use the azimuthal modes $n = 0$ and ± 1, but it is worth noting that when the invasion is symmetric, we only need the harmonic $n = 0$ to calculate in a precise fashion the induced voltages at RX_1 and RX_2. In this case, the integral along ϕ showed in (2-112) must be identical for the electric fields exited by different quantities of azimuthal modes. For proving the theory we illustrate in Figure 4.17 and Figure 4.18 the field E_ϕ at RX_1, when $\alpha = 360°$ for $z = -10$ in. As can be seen in the figures, the area under the curve (the integral) of the electric field is the same for all cases, as expected theoretically.

4.3.2 Case Study 2

Sequentially, we increase the conductivity of the invaded zone to $\sigma = 1$ S/m for accentuating $\Delta\bar{\bar{\epsilon}}$. The Figure 4.19 and Figure 4.20 show the phase and amplitude voltages relation of RX_2 and RX_1 for this configuration. We evaluate the effects of this higher contrast in the BA accuracy, we note that the error increases, as expected theoretically.

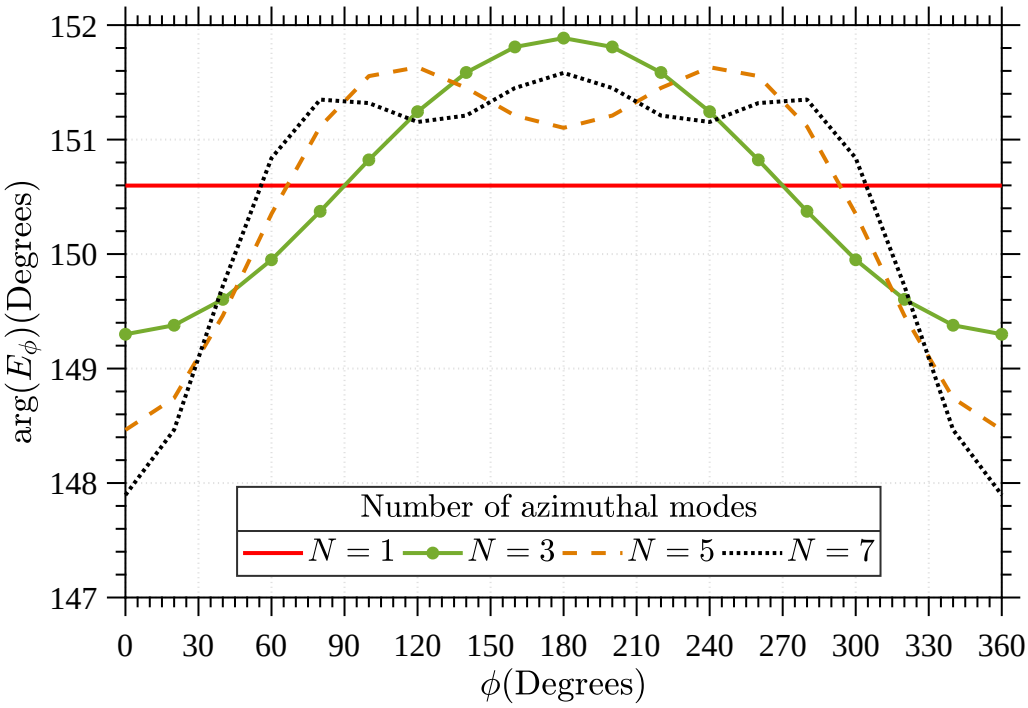

Figure 4.17: E_ϕ phase for a symmetric invasion at $z_T = -10$ exited by different number of azimuthal modes.

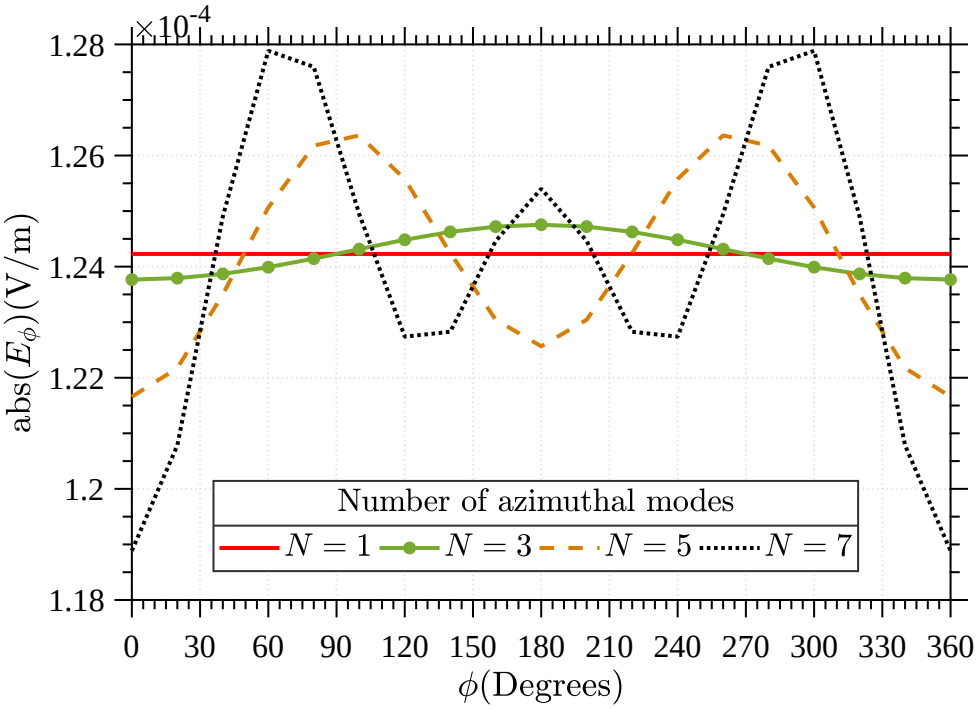

Figure 4.18: E_ϕ amplitude for a symmetric invasion at $z_T = -10$ exited by different number of azimuthal modes.

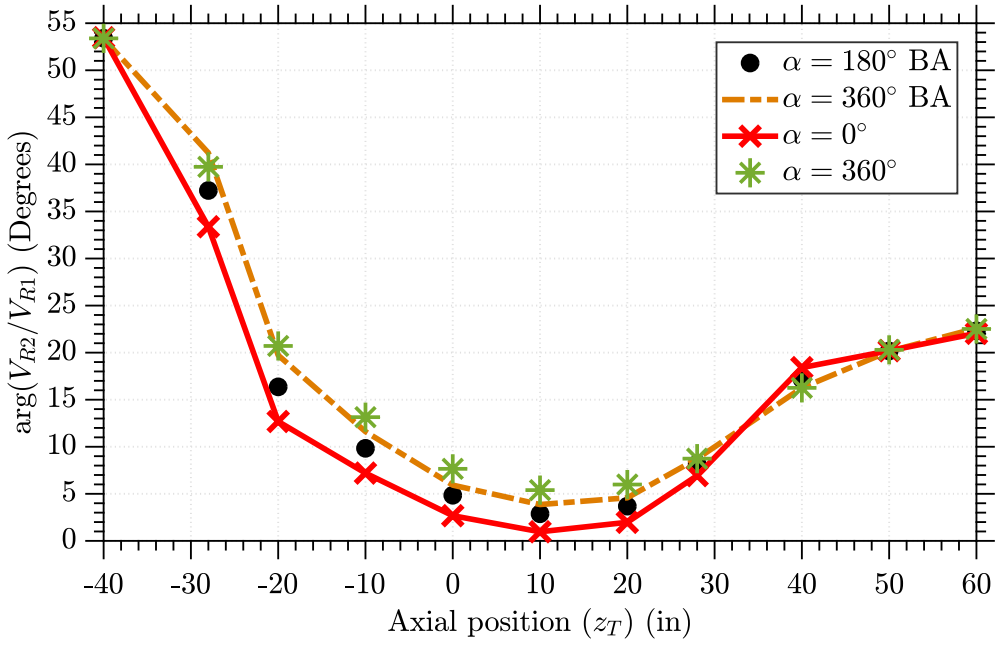

Figure 4.19: Phase difference for a moving LWD tool traversing a bed layer (formation 2) with a non-invaded ($\alpha = 0°$), a symmetrical ($\alpha = 360°$), and a non-symmetrical ($\alpha = 180°$) invaded zones. Our results are indicated by the label BA. The abscissa represents the axial position of the TX antenna.

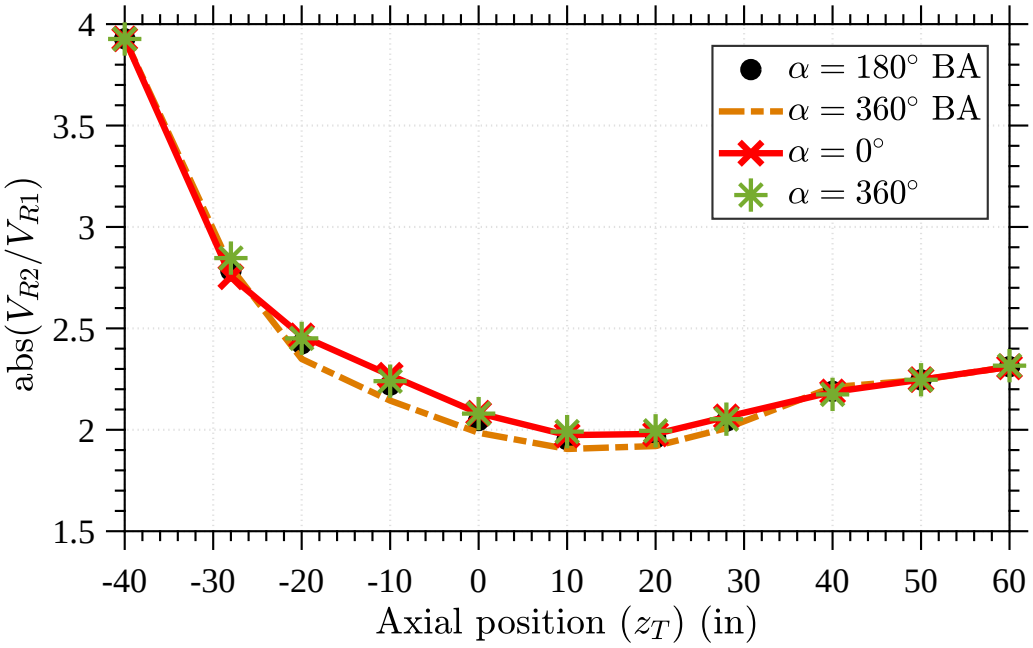

Figure 4.20: Amplitude difference for a moving LWD tool traversing a bed layer (formation 2) with a non-invaded ($\alpha = 0°$), a symmetrical ($\alpha = 360°$), and a non-symmetrical ($\alpha = 180°$) invaded zones. Our results are indicated by the label BA. The abscissa represents the axial position of the TX antenna.

4.3.3 Case Study 3

Consider now that the formation 2 in Figure 4.21 is invaded by a non-symmetric scatterer with $\sigma = 2$ S/m, the dimension and constitutive

parameters are kept as presented in Section 4.1.Figure 4.22 and Figure 4.23 show the amplitude and phase of the received voltages at RX for three invasion cases: $\alpha = \{0°, 180°, 360°\}$.

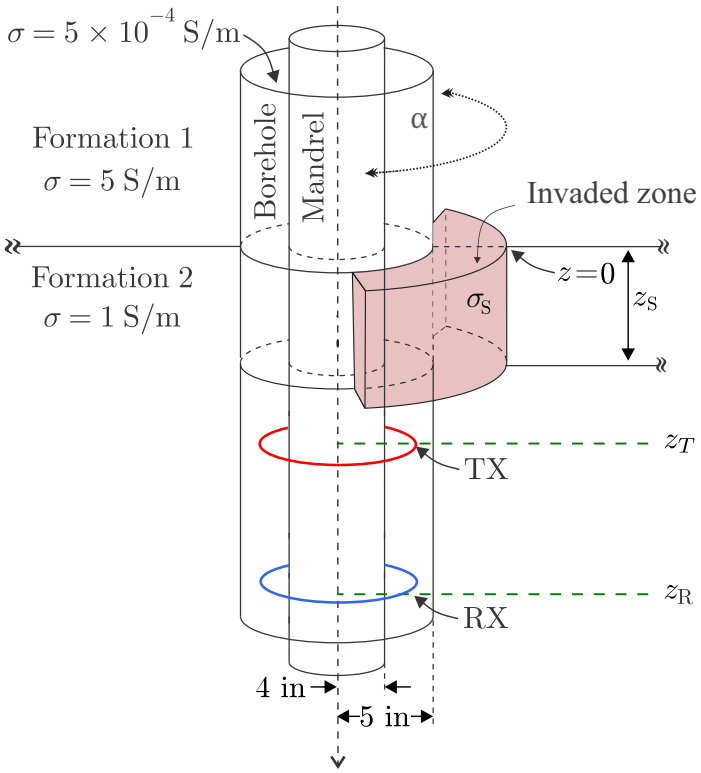

Figure 4.21: Asymmetric invasion inside a layered cylindrical medium.

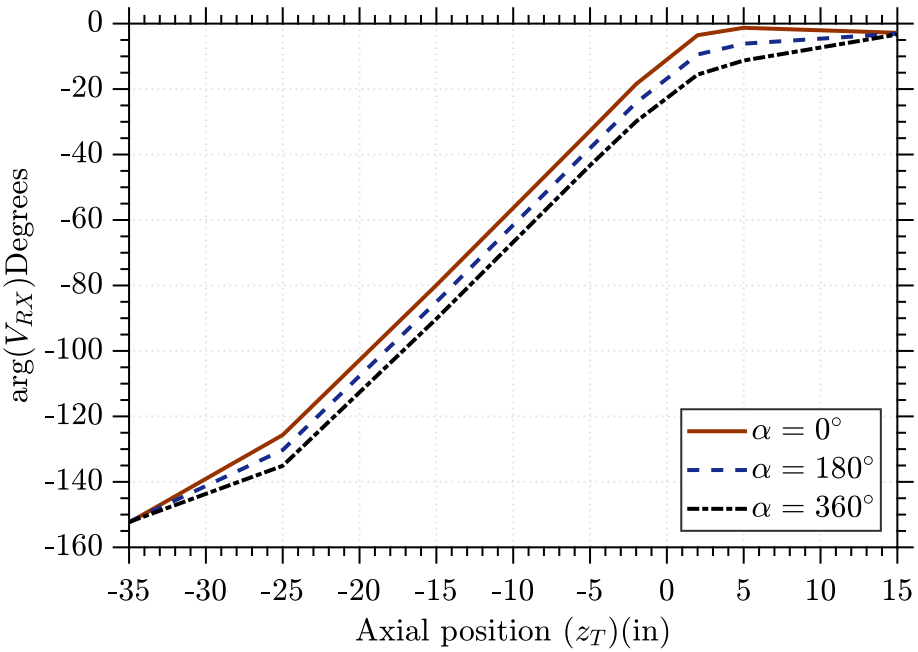

Figure 4.22: Phase voltage at RX due to a symmetric and non-symmetric invasions.

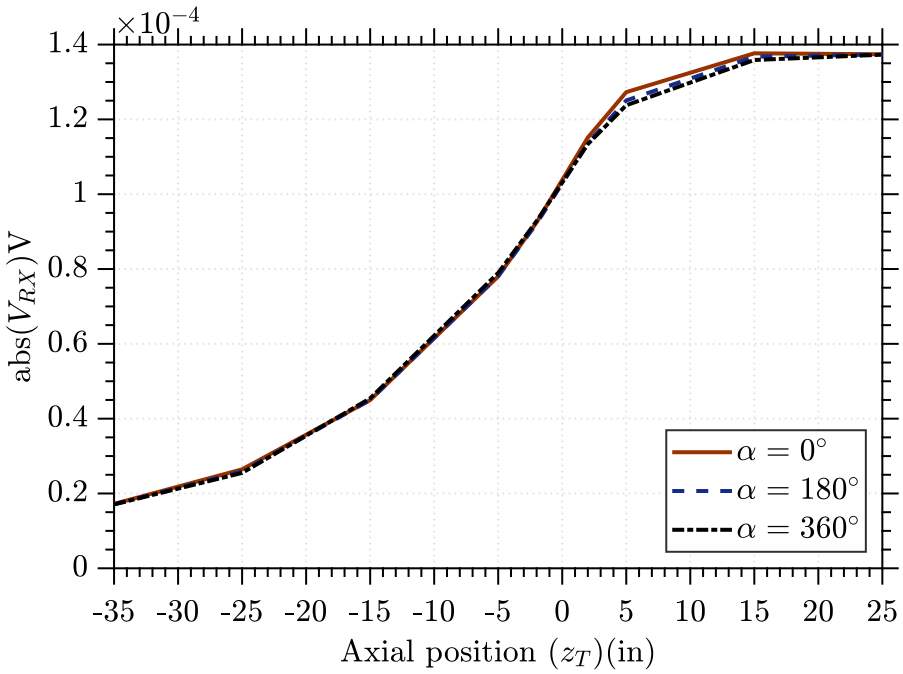

Figure 4.23: Amplitude voltage at RX due to a symmetric and non-symmetric invasions.

The voltage for the cases $\alpha = 0°$ and $\alpha = 360°$ was validated using the MMT-based method, as illustrated in Figure 4.2 and Figure 4.3. The voltage for the case $\alpha = 180°$ is between the other two cases, as expected.

4.4 Anisotropic Dipping Layer

Figure 4.24 shows the geometry of a layered earth formation with a dipping bed. These cases commonly exist when the formation presents a directional soil fracture or during a deviated drilling [15] (deviation of a wellbore from the natural vertical path). The dipping layer inclination is defined by the dipping angle θ_s, as illustrated in Figure 4.24. The dipping angle is related to the axial layer position z_a as follows

$$z_a = z'_a - \rho_s \tan\theta_s \cos\phi \tag{4-1}$$

where ϕ is the invasion azimuthal angle and z'_a is the axial layer position when $\theta_s = 0°$.

Consider a tilted layer of thickness $z_s = 10$ in, characterized by a uniaxial conductivity $\bar{\bar{\sigma}}_s = \text{diag}\,[1.2, 1.2, 0.8]$ S/m. The bed is radially unbounded; then, we simulate it with a radius $\rho_s = 50$ in, which guarantees that the solution is adequate since the chosen radius is sufficient to represent the unbounded radial medium. The geophysical formation is composed by a uniaxial material that posses a conductivity of $\bar{\bar{\sigma}}_b = \text{diag}\,[1, 1, 0.5]$ S/m. The borehole is filled

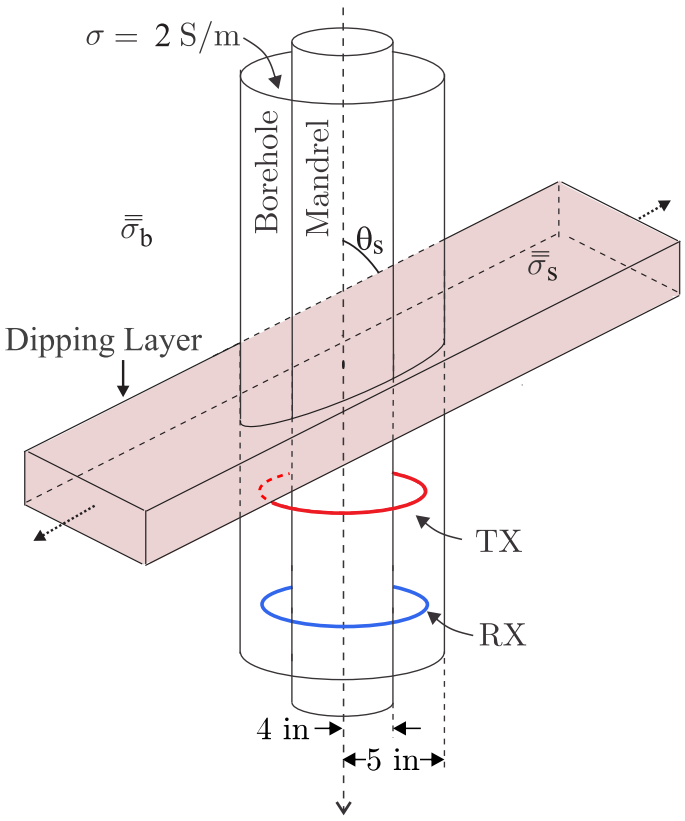

Figure 4.24: Well-logging tool traversing a dipping bed layer.

with isotropic material with a conductivity of $\sigma = 2$ S/m. The whole media present relative permittivity $\epsilon_r = 1$, relative permeability $\mu_r = 1$, and the receiver RX is placed at $z = z_T + 24$ in. We evaluate the phase voltage for three dipping angles $\theta_s = \{0°, 30°, 50°\}$, as illustrated in Figure 4.25. For the case, $\theta_s = 0°$, we compare our solution with the reference method, the two sets of results agree very well. We can see in the figure that as the tilted angle increases the voltage response becomes more open, and the minimum value of the amplitude increase. We can expect this response because tilting the layer will produce reflections at points above and below the original horizontal layer.

Consider now a totally anisotropic dipping bed with a fully filled conductivity tensor. As presented in [15, 30], this tensor can be function of the layer position, i.e.,

$$\bar{\bar{\sigma}}_s = \begin{bmatrix} \sigma^s_{\rho\rho} & \sigma^s_{\rho\phi} & \sigma^s_{\rho z} \\ \sigma^s_{\phi\rho} & \sigma^s_{\phi\phi} & \sigma^s_{\phi z} \\ \sigma^s_{z\rho} & \sigma^s_{z\phi} & \sigma^s_{zz} \end{bmatrix}, \tag{4-2}$$

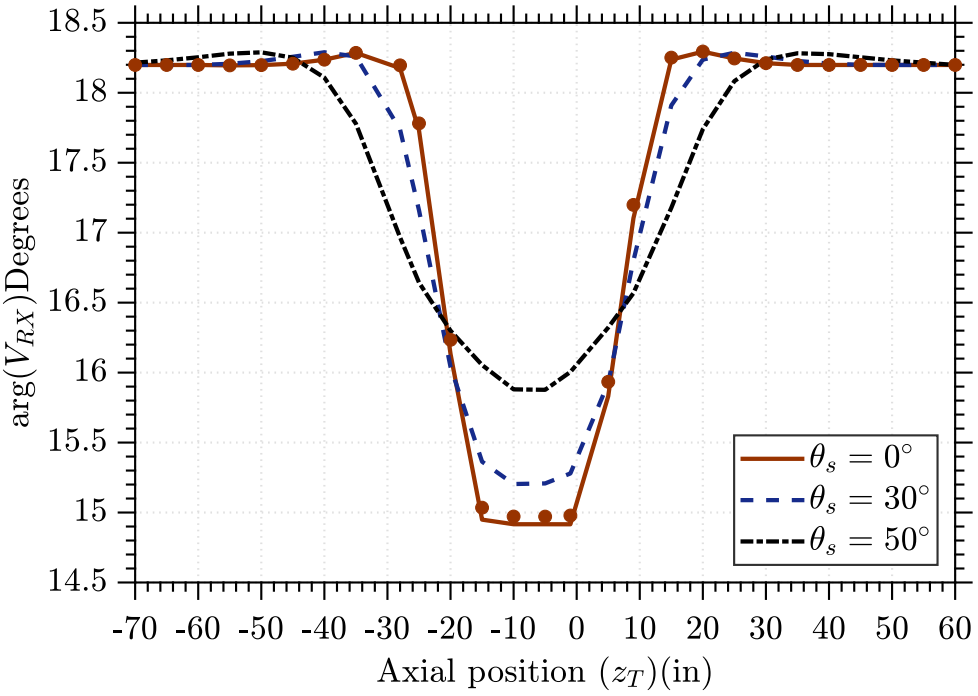

Figure 4.25: Phase voltage at RX due to dipping beds characterized by the angle θ_s. The lines represent the results obtained by BA approximation and the symbols by the MMT-based method.

where

$$\sigma^s_{\rho\rho} = \sigma_\rho \cos^2\phi + \sigma_\phi \sin^2\phi, \tag{4-3}$$

$$\sigma^s_{\rho\phi} = -\sigma_\rho \sin\phi\cos\phi + \sigma_\phi \sin\phi\cos\phi, \tag{4-4}$$

$$\sigma^s_{\rho z} = (\sigma_v - \sigma_h)\cos\phi \sin\theta_s \cos\theta_s, \tag{4-5}$$

$$\sigma^s_{\phi\rho} = -\sigma_\rho \cos\phi\sin\phi + \sigma_\phi \sin\phi\cos\phi, \tag{4-6}$$

$$\sigma^s_{\phi\phi} = \sigma_\rho \sin^2\phi + \sigma_\phi \cos^2\phi, \tag{4-7}$$

$$\sigma^s_{\phi z} = -(\sigma_v - \sigma_h)\sin\phi \sin\theta_s \cos\theta_s, \tag{4-8}$$

$$\sigma^s_{z\rho} = (\sigma_v - \sigma_h)\cos\phi \sin\theta_s \cos\theta_s, \tag{4-9}$$

$$\sigma^s_{z\phi} = -(\sigma_v - \sigma_h)\sin\phi \sin\theta_s \cos\theta_s, \tag{4-10}$$

$$\sigma^s_{zz} = \sigma_h \sin^2\theta_s + \sigma_v \cos^2\theta_s, \tag{4-11}$$

$$\sigma_\rho = \sigma_h \cos^2\theta_s + \sigma_v \sin^2\theta_s, \tag{4-12}$$

$$\sigma_\phi = \sigma_h. \tag{4-13}$$

The conductivities σ_h and σ_v are the vertical and radial conductivities, respectively. We will calculate the induce voltage at RX perturbed by two totally anisotropic layers with inclination $\theta_s = 30°$ and of conductivity $\bar{\bar{\sigma}}_{s1}$ and $\bar{\bar{\sigma}}_{s2}$, respectively. We assume $\sigma_h = 1.2$ S/m and $\sigma_v = 0.8$ S/m for the first case, and $\sigma_h = 0.8$ S/m and $\sigma_v = 0.3$ S/m for the second. These cases are compared

with their uniaxial counterpart of $\bar{\bar{\sigma}}_{s1}(\text{uniaxial}) = \text{diag}\,[1.2, 1.2, 0.8]$ S/m, and $\bar{\bar{\sigma}}_{s2}(\text{uniaxial}) = \text{diag}\,[0.8, 0.8, 0.3]$ S/m. Figure 4.26 illustrates the differences between the phase voltage for the uniaxial and the anisotropic tilted layer cases. We can observe that the anisotropy varies substantially the behavior of the voltage. BA allows us to model objects with complex anisotropies immersed in complex layered media.

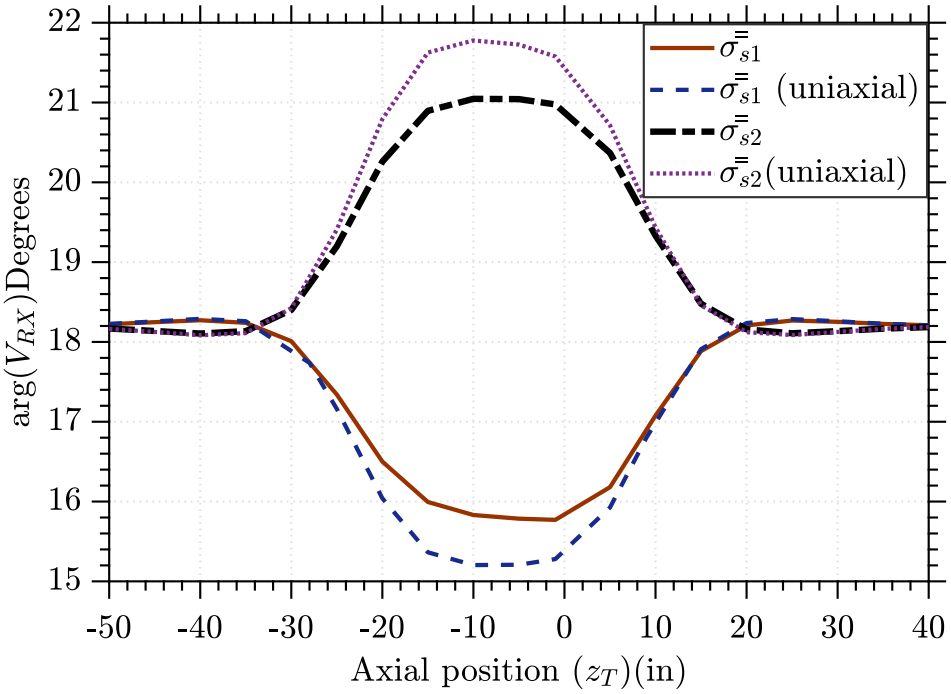

Figure 4.26: Phase voltage at RX due to anisotropoic dipping beds.

4.5 Borehole Failures

When a hole is bored in porous soil formations, the borehole cross-section format can lose its circular symmetry, and that will result in a geometrical failure as a consequence of the non-regular invasion around the borehole. This phenomenon is related to the heterogeneity of the formations and the distribution of strain as well as the stress [65]. An increase in the risky factors are given mainly for the multilateral well prospecting, a proficient technology for improving the production for oil and gas wells [65]. Taking advantage of the versatility of the BA, we can simulate different borehole geometries, as a case study, and for modeling a recurrent geometry presented in borehole failures, we evaluate an oval-shaped borehole, as illustrated in Figure 4.27.

The borehole considered in this cases posses a conductivity of $\sigma = 2$ S/m, the background media has $\sigma = 1$ S/m, and RX is placed at $z = z_T + 24$ in. The remaining parameters are kept as those used in Section 4.1. We evaluate two

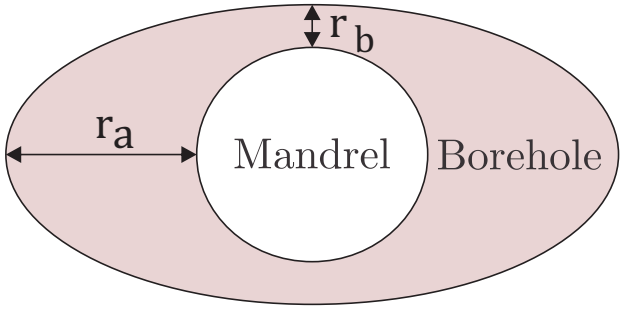

Figure 4.27: Oval-shaped borehole.

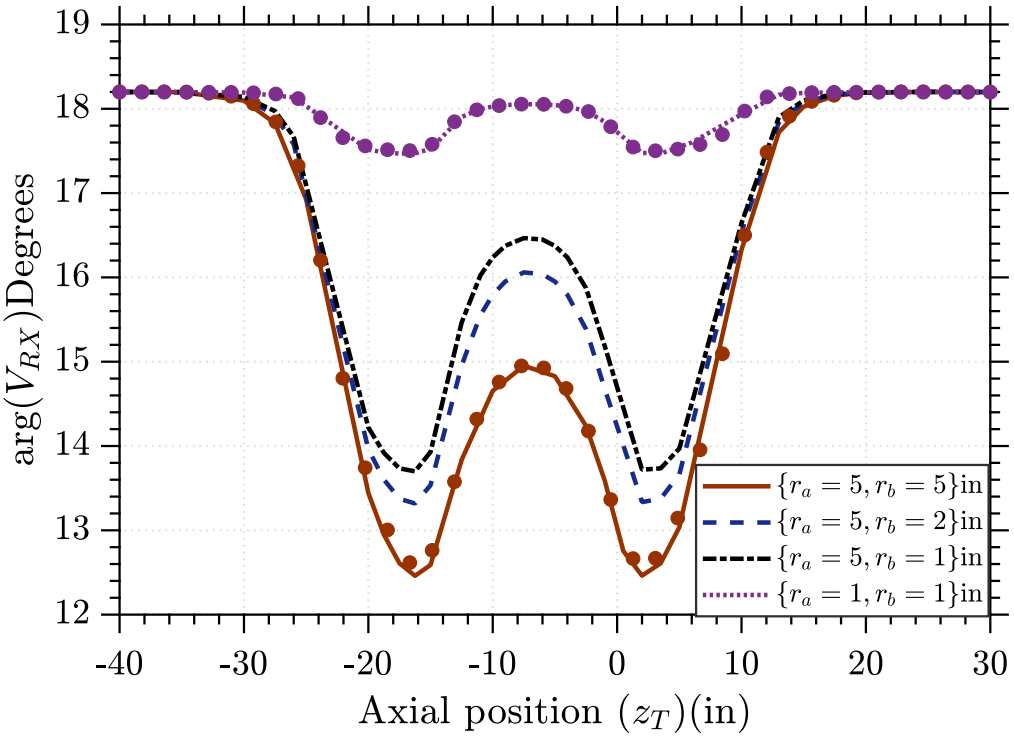

Figure 4.28: Phase voltage at RX due to oval-shaped borehole. The lines represent the results obtained by BA approximation and the symbols by the MMT-based method.

elliptical cases with the minor radii $r_b = \{2, 1\}$ in, and major radius $r_a = 5$ in. Then, we compute V_{RX} for the symmetric cases $r_b = r_a = 1$ and $r_b = r_a = 5$. Phase voltage results are illustrated in Figure 4.28. The symmetric examples results can be compared with the reference method, as shown in Figure 4.28. The asymmetric ones are between the extrema like expected. In the figure we can observe oscillations when $-20\,\text{in} < z_T < 10\,\text{in}$, this phenomenon is due to reflections produced in the borehole-background medium interface.

4.6 Tilted-Coil Antennas

In this section, we will calculate the induced voltage at the RX tilted-coil antennas due to tilted-coil transmitters. By cause of the antennas geometry, even if the scatterer is symmetric, the problem requires the modal voltage summation in (2-113) taking into consideration the azimuthal harmonic index $n = \{0, 1, -1, ...\}$. For tilted RX cases as well as when is considered an asymmetric scatterer, for a BA solution, the integral along the RX antenna in (2-112) must be solved numerically.

4.6.1 Case Study 1 - Symmetric Invasion

Consider a symmetric invasion characterized by a isotropic conductivity of $\sigma_s = 5.5$ S/m immerse in a background media with conductivity $\sigma = 5$ S/m. The well borehole has a conductivity of $\sigma = 2$ S/m, RX is placed 30 in away from TX. The RX and TX antennas are tilted-coil antennas described by (2-106), both have a tilted angle of $\theta_T = \theta_R = 10^{\circ}$. The scatterer and background dimension are kept as in Section 4.1. Figure 4.29 and Figure 4.30 show the phase and amplitude voltage, respectively. The two sets of results agree well in terms of phase, and they have a slight deviation in amplitude terms.

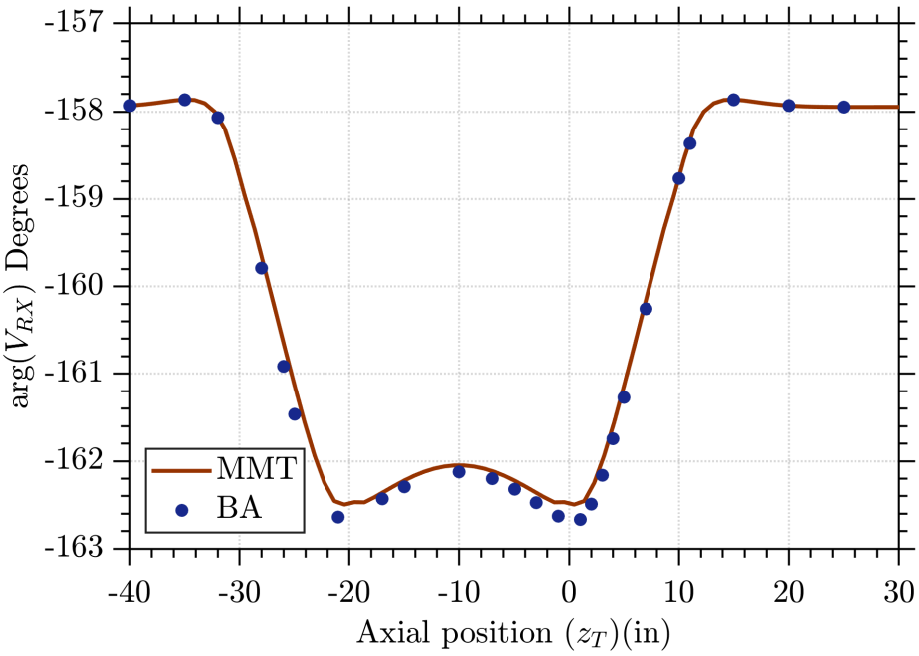

Figure 4.29: Phase voltage at tilted RX due to a symmetric invasion. The lines represent the results obtained by MMT approximation and the symbols by the BA-based method.

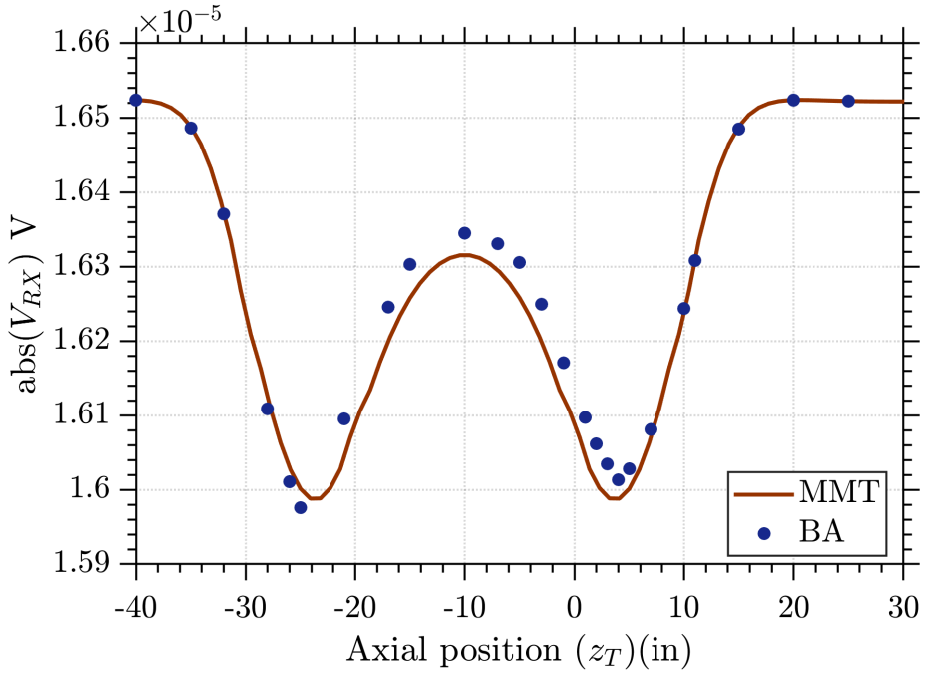

Figure 4.30: Amplitude voltage at tilted RX due to a symmetric invasion. The lines represent the results obtained by MMT approximation and the symbols by the BA-based method.

4.6.2
Case Study 2 - Oval-Shaped Borehole

Consider the example defined in Section 4.5 and examine now the induced voltage at a RX tilted-coil. Both TX and RX are described by a tilted angle of $\theta_T = \theta_R = 10^{\circ}$. We evaluate an elliptical case described by a minor radius of $r_b = 2$ in, and a major radius of $r_a = 5$ in. Then, we compute V_{RX} analytically for the symmetric cases $r_b = r_a = 2$ and $r_b = r_a = 5$. Phase voltage results are illustrated in Figure 4.31; as expected, the asymmetric case is between the symmetric ones.

4.7
Summary of Chapter 4

- The numerical integration along the tilted antenna in (2-112) converges rapidly for the cases presented in this section. To obtain the solution, we need very few points; in our examples, only 9 points around the loop were necessary for the field convergence.
- The MMT based method requires more electromagnetic modes to accurately model the propagation problem by using tilted antennas [5]. This fact added to that the scatterer and receiver coil are very close to each other, at some points in our setup, increases the computational effort.

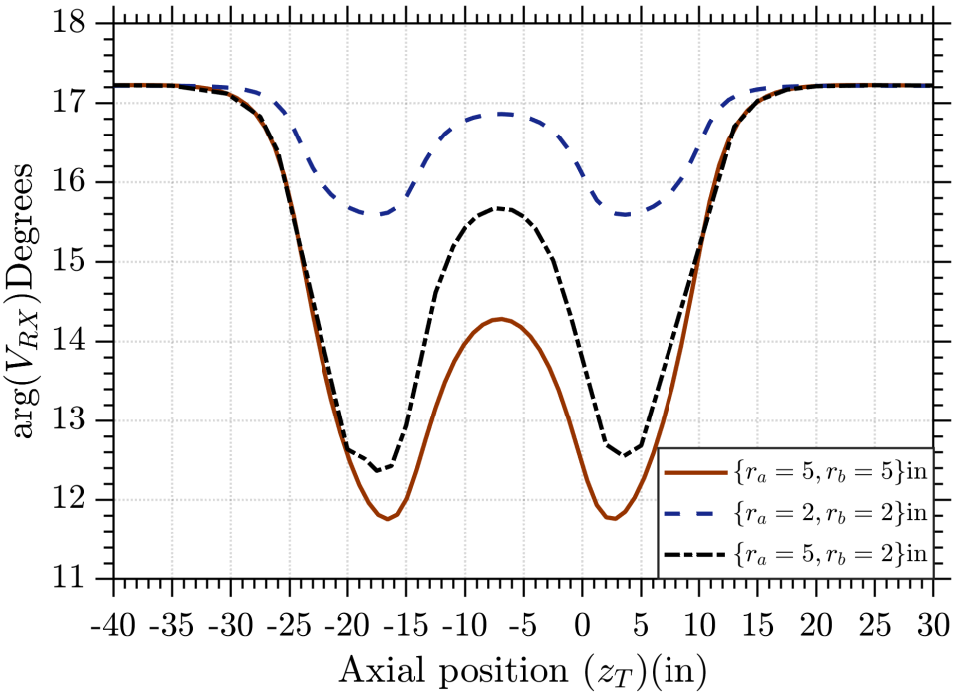

Figure 4.31: Amplitude voltage at tilted RX due to a perturbed by oval-shaped borehole.

In the examples above, for points near discontinuities, we required more than 200 radial modes ($p > 200$) until the convergence.

5
Comparison between EBA and BA

In this chapter, we will compare some aspects of BA and EBA algorithms for describing electromagnetic fields inside and in the vicinity of the scatterer. We will present several case studies to visualize the electric field behavior as a function of the observer position. We employed the prescriptions of (3-54) to compute the electric field via EBA and (3-41) for the BA. For all the case scenarios presented in this chapter, we considered that the LWD tool operates at 2 MHz, and the TX is carrying a constant current of 1 A. The mandrel radius is fixed to $\rho_m = 4$ in, the borehole has the radius $\rho_b = 5$ in, and the geophysical formations are radially-truncated by a perfect electric conductor boundary condition at $\rho = 60$ in.

5.1
Electric Profile Variations

In this case, we will fix the transmitter TX at $z_T = -10$ in, while the observation point RX is in axial movement crossing the scatterer from the point $z_R = -5$ in to $z_R = 5$ in. The radius of the TX coil is $\rho_T = 4.5$ in, as in the cases showed in Chapter 4, and the radial position for the observation point will be fixed at $\rho_R = 8$ in.

5.1.1
Case Study 1

First, consider an isotropic media formation characterized by a conductivity of $\sigma = 5$ s/m and a borehole of $\sigma = 2$ S/m. The medium is invaded by a symmetrical scatterer of $\sigma = 6$ S/m, and dimensions $z_S = 10$ in and $\rho_s = 10$ in located between 5 in $< \rho <$ 15 in. Figure 5.1 and Figure 5.2 show the phase and amplitude of E_ϕ, respectively. In the figures, the background line represents the field in the absence of the scatterer, and the analytic line stands for the analytical solution when the scatterer exists. In this example, we observe that the amplitude field variation is negligible for the cases with or without scatterer. In terms of the phase, we have a maximum difference of ten degrees between the background solution and the analytical. The BA technique reproduces the behavior of the field along all the domain very precisely. The

EBA technique presents an improvement to represent the total fields over the background results, but not as accurate as of the BA approach. We must keep in mind that the EBA is a valid approximation for points around or inside the scatterer ($\mathbf{r}_0 - \mathbf{r} \approx \mathbf{0}$). To get a solution at any point outside the scatterer, we should re-radiate the fields calculated inside the scatterer via (3-61) and (3-62). We would only expect an advantage of the EBA over the BA after the re-radiation process, and this can be explained considering a case with the variation of the electric profile as the case considered in this subsection. For an electric profile (3-61) is reduced to

$$\mathbf{E}(\mathbf{r}) = \mathbf{E}_b(\mathbf{r}) - i\omega \int_V \bar{\bar{G}}^{ee}(\mathbf{r}, \mathbf{r}_0) \cdot \Delta\bar{\bar{\epsilon}} \cdot \ \bar{\bar{\bar{\Lambda}}}(\mathbf{r}_0) \cdot \mathbf{E}_b(\mathbf{r}_0)\, d\mathbf{r}_0, \tag{5-1}$$

where

$$\bar{\bar{\bar{\Lambda}}}(\mathbf{r}) = \left[\bar{\bar{I}} - \bar{\bar{S}}^{ee}(\mathbf{r})\right]^{-1}, \tag{5-2}$$

$$\bar{\bar{S}}^{ee}(\mathbf{r}) = -i\omega \int_V \bar{\bar{G}}^{ee}(\mathbf{r}, \mathbf{r}_0) \cdot \Delta\bar{\bar{\epsilon}}\, d\mathbf{r}_0. \tag{5-3}$$

In case of $\bar{\bar{S}}^{ee}(\mathbf{r}) \ll \bar{\bar{I}}$, we can approximate (5-2) by

$$\bar{\bar{\bar{\Lambda}}}(\mathbf{r}_0) \approx \bar{\bar{I}} + \bar{\bar{S}}^{ee}(\mathbf{r}_0). \tag{5-4}$$

Substituting the above into (5-1) allows us to obtain

$$\begin{aligned} \mathbf{E}(\mathbf{r}) = \mathbf{E}_b(\mathbf{r}) &- i\omega \int_V \bar{\bar{G}}^{ee}(\mathbf{r}, \mathbf{r}_0) \cdot \Delta\bar{\bar{\epsilon}} \cdot \mathbf{E}_b(\mathbf{r}_0)\, d\mathbf{r}_0 \\ &- i\omega \int_V \bar{\bar{G}}^{ee}(\mathbf{r}, \mathbf{r}_0) \cdot \Delta\bar{\bar{\epsilon}} \cdot \bar{\bar{S}}^{ee}(\mathbf{r}_0) \cdot \mathbf{E}_b(\mathbf{r}_0)\, d\mathbf{r}_0, \end{aligned} \tag{5-5}$$

where the second term resemble the conventional BA scattering contribution to the background fields, i.e., a first-order correction in terms of $\Delta\bar{\bar{\epsilon}}$, while the last term can be seen as a second-order correction.

5.1.2 Case Study 2

Consider the background and scatterer dimension presented in Section 4.1 for a symmetric scatterer of $\sigma_s = 10$ S/m. Figure 5.3 and Figure 5.4 illustrate the phase and amplitude of the electric field component E_ϕ calculated via BA, EBA, and analytically by MMT-based technique. In this case, we observe amplitude and phase variations when compared to the analytic response and the background electric field. We have a $\Delta\epsilon$ greater than the limitations of the BA; this fact is illustrated clearly in the figures, where the analytical field could not be reproduced accurately by this technique. The EBA technique presents an improvement to represent the total fields over the background results. To compare the technique outside the scatterer region, we should re-radiate the fields to obtain a conclusion about EBA accuracy.

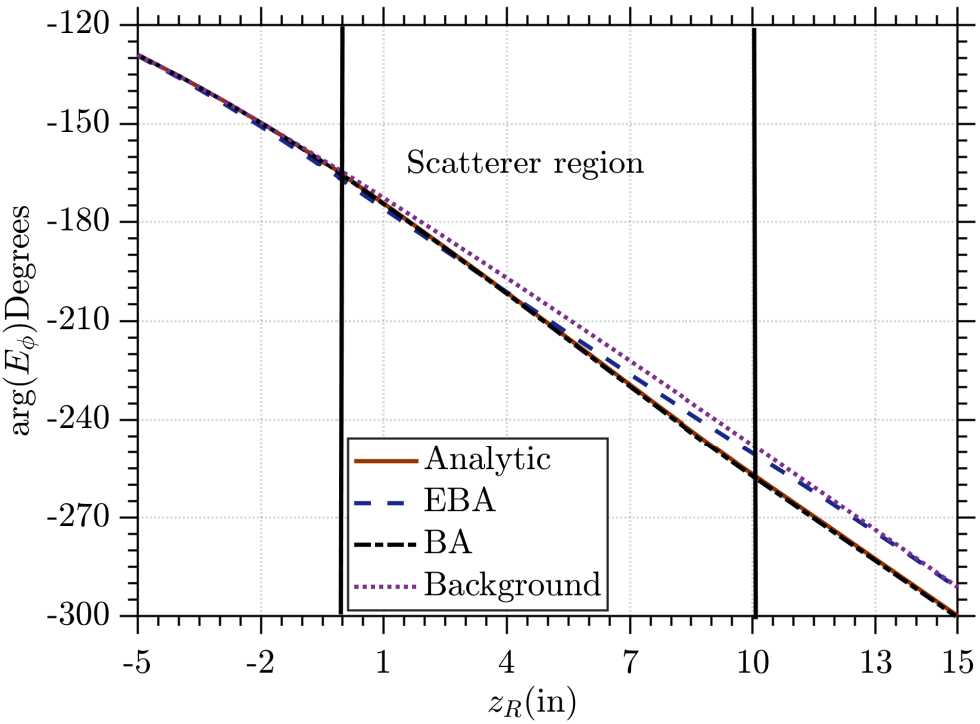

Figure 5.1: E_ϕ phase for a moving observation point traversing a layer with $\sigma_s = 6$ S/m. The abscissa represents the axial position of the RX.

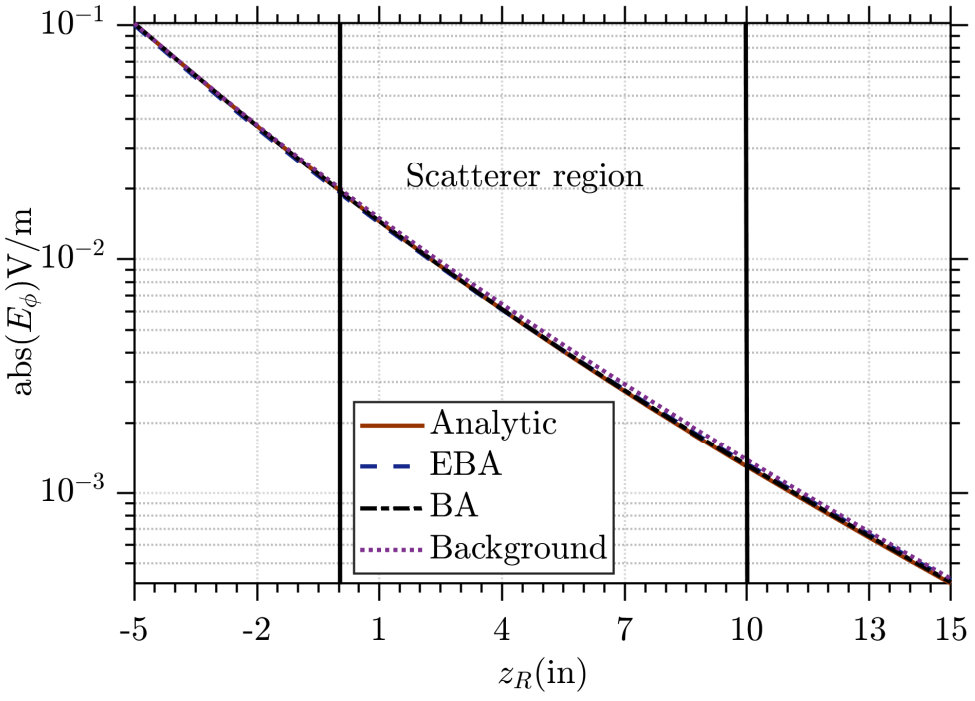

Figure 5.2: E_ϕ amplitude for a moving observation point traversing a layer with $\sigma_s = 6$ S/m. The abscissa represents the axial position of the RX.

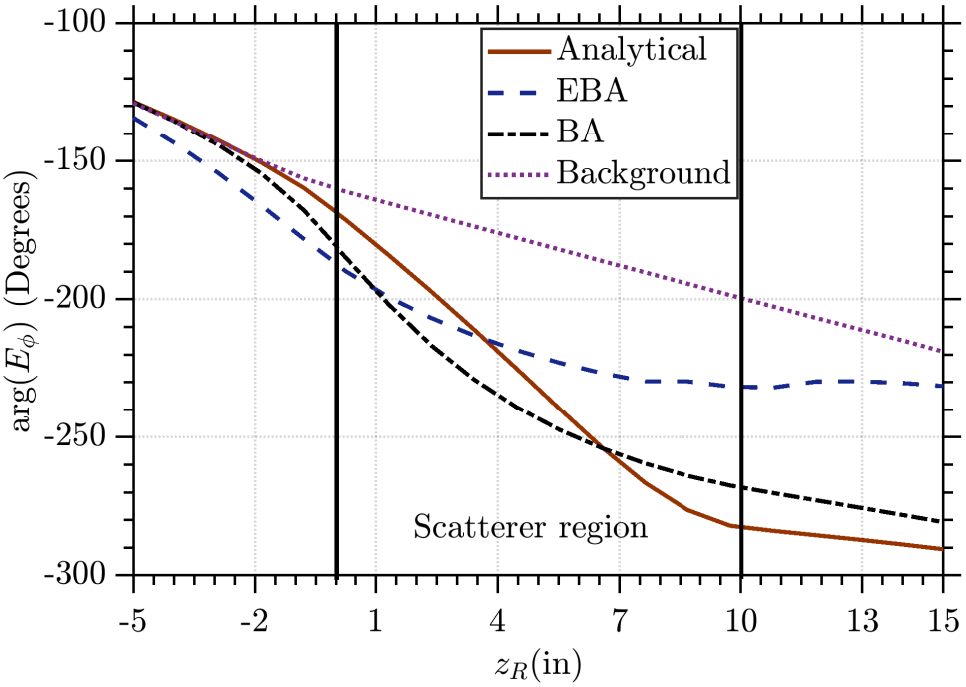

Figure 5.3: E_ϕ phase for a moving observation point traversing a layer with $\sigma_s = 10$ S/m. The abscissa represents the axial position of the RX.

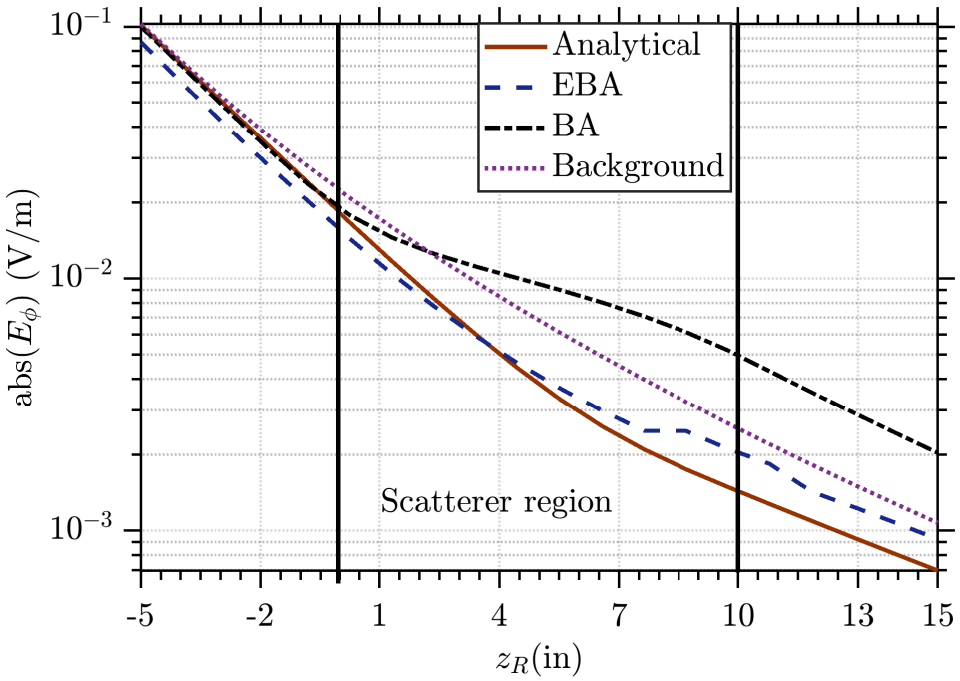

Figure 5.4: E_ϕ amplitude for a moving observation point traversing a layer with $\sigma_s = 10$ S/m. The abscissa represents the axial position of the RX.

5.2 Magnetic Profile Variations

Now, we will evaluate the E_ϕ variations due to a scatterer with $\mu_s = 3$ and $\sigma = 1$ S/m. The background medium and the remain parameters are kept

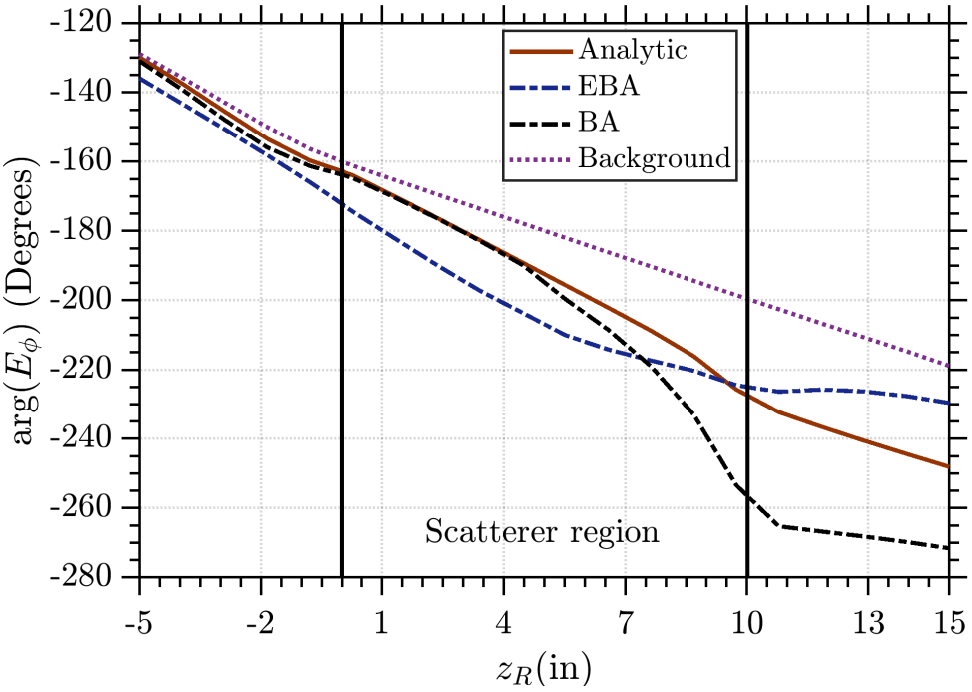

Figure 5.5: E_ϕ phase for a moving observation point traversing a layer with $\mu_s = 3$. The abscissa represents the axial position of the RX.

as in section 5.1. Figure 5.5 and Figure 5.6 show the phase and amplitude of E_ϕ calculated via BA, EBA and analytically. In this case, we observe amplitude and phase variations when compared to the analytic response and the background electric field. We have a $\Delta\mu$ greater than the limitations of the BA; the analytical field could not be reproduced accurately by this technique.

5.3 Electric and Magnetic Profile Variations

For a simultaneous electric and magnetic variation, we will evaluate a scatterer with $\mu_s = 3$ and $\sigma = 5$ S/m. The background and the other parameters are maintained as in section 5.1 and section 5.2. Figure 5.7 and Figure 5.8 illustrate the phase and amplitude of E_ϕ calculated via BA, EBA and MMT-based technique. The variations $\Delta\mu$ and $\Delta\epsilon$ are greater than the limitations of the BA, and the analytical field could not be simulated accurately by this technique.

5.4 Summary of Chapter 5

BA and EBA solutions provide corrections to the total fields of the background results. To get a conclusive result, we should compute the scattered

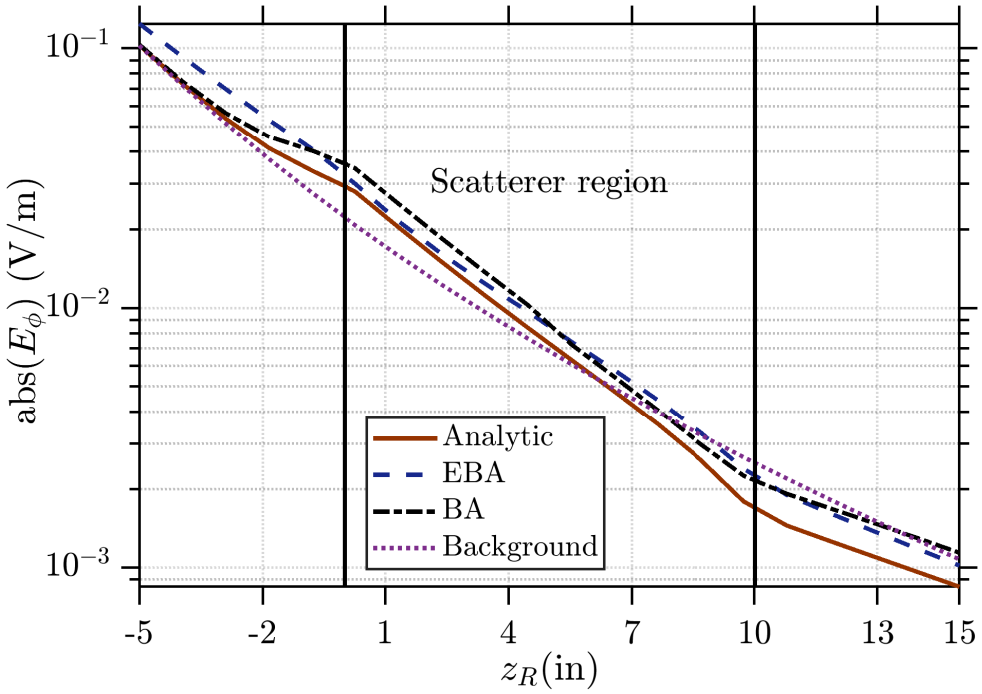

Figure 5.6: E_ϕ amplitude for a moving observation point traversing a layer with $\mu_s = 3$. The abscissa represents the axial position of the RX.

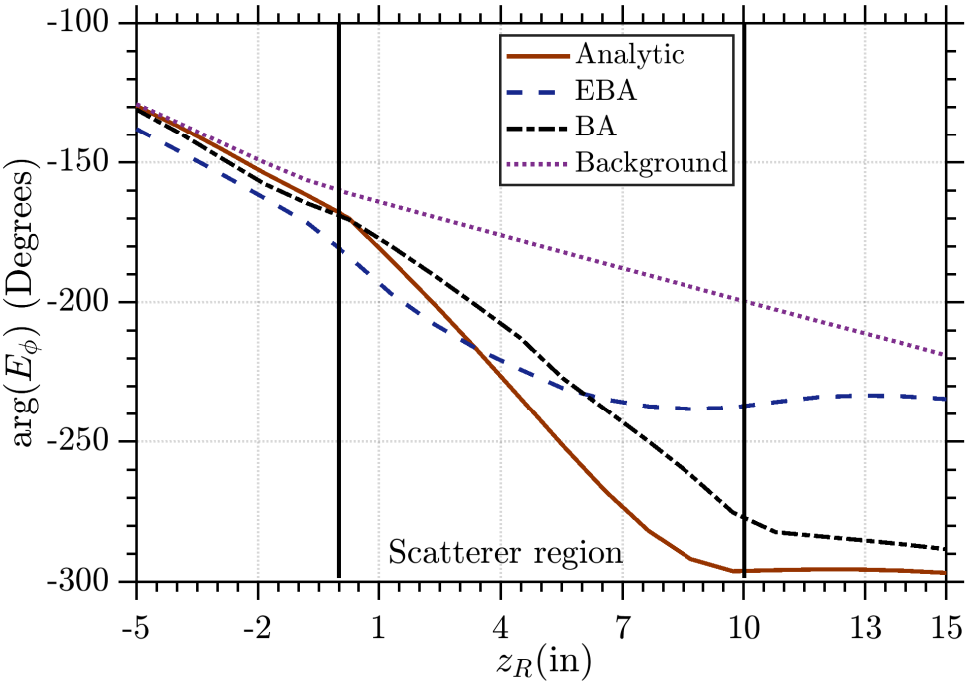

Figure 5.7: E_ϕ phase for a moving observation point traversing a layer with $\mu_s = 3$ and $\sigma = 5$ S/m. The abscissa represents the axial position of the RX.

field $\mathbf{E}_s$ at an observation point RX outside the scatterer region. For this calculation, the extended technique requires the re-radiation of the fields inside the scatterer as presented in (3-61) and (3-62). Moreover, the re-radiation

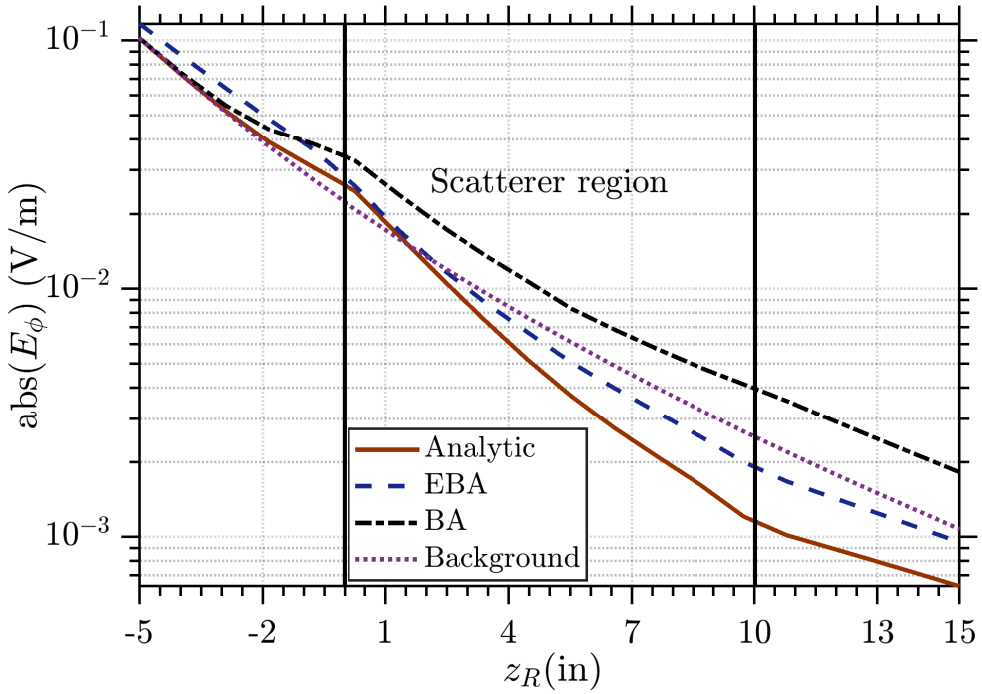

Figure 5.8: E_ϕ amplitude for a moving observation point traversing a layer with $\mu_s = 3$ and $\sigma = 5$ S/m. The abscissa represents the axial position of the RX.

process demands more computational resources than required by the BA algorithm. It is due to that in the BA algorithm, the dyadics are calculated once, while in the EBA approach, they are calculated once for each scatterer discretization point.

6
Realistic Antenna Modeling for Well-Logging Sensing

6.1
Introduction

The next generation of logging sensors for oil prospecting requires a realistic antenna modeling. Due to impedance mismatching that LWD sensors face between the feed and the coil antenna, the telemetry system decreases its performance [18, 19]. The modeling of the mutual- and self-impedance of antenna coil sensors allows the accurate characterization of these devices and avoids mismatching. The computation of the impedance for coil antennas immersed in complex-layered cylindrical media is a topic that was not addressed adequately in the literature because it demands high-cost CEM based on finite-differences (FD) or finite-elements (FEM).

In many mode-matching solutions for modeling LWD tools, such those in [37, 66, 67], the source is usually an infinitesimal magnetic dipole. More sophisticated approaches consider a delta-type coil current source [5, 21, 25, 68, 69]. To the best of our knowledge, there is no report of any analytical or semi-analytical methodology for computing the influence of the finite size of a realistic LWD antenna. The reflection effects induced by the mandrel that supports the LWD tools cannot be easily incorporated in standard NMM-based formulations. In this chapter, we present a novel semi-analytical mode-matching technique for modeling the antenna input impedance in a precise fashion. A distinguishing feature of our present approach is that the mode-matching does not rely on a numerical discretization of the space domain. In this way, we optimize the computational performance. Our objective is to calculate the input impedance of antennas used in practical LWD tools such as those implemented by many oilfield contractors [9 – 12]. We propose to study the behavior of these impedances in different scenarios.

We present numerical results of some case studies to validate our formulation versus that based on the finite-difference-time-domain (FDTD) provided by a commercial CEM software. Besides, we present a sensitivity analysis of the sensor impedance in terms of its physical dimension, operating frequency, and constitutive parameters of the surrounding medium. We show that our

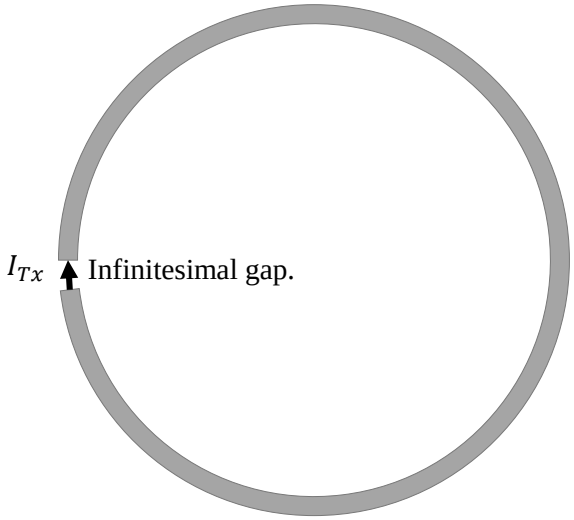

Figure 6.1: Coil antenna excited by the current I_{TX}.

technique is an excellent alternative method for modeling realistic LWD tools in inhomogeneous, anisotropic, and dissipative media.

6.2 Electromagnetic Modeling

6.2.1 Input Impedance

A perfect electric conducting (PEC) antenna excited by a current source I_{TX} as depicted in Figure 6.1 distributes the current on the antenna surface, so that tangential components of the total electric field vanish inside the PEC. If we consider the antenna terminals as an infinitesimal gap, the reaction of any field with the current source can be expressed as $-VI_{\mathrm{TX}}$. The relation between the voltage and the current at the gap terminals is defined as the input impedance. A finite-dimension coil antenna as its input impedance determined by integrating the electric field and the surface current density according to [51, Ch. 7], [70]

$$Z_{\mathrm{in}} = -\frac{\langle \mathbf{E}, \mathbf{J}_s \rangle}{I_{\mathrm{TX}}^2} \tag{6-1}$$

$$= -\frac{1}{I_{\mathrm{TX}}^2} \oiint \mathbf{E} \cdot \mathbf{J}_s \, ds, \tag{6-2}$$

where $\mathbf{J}_s$ is the current density distribution over the antenna surface.

The integral in (6-1) is calculated by using the radiated electric field by an infinitesimal antenna as showed in Chapter 2 on the antenna surface. In our model, this infinitesimal antenna is placed at the middle of the finite-

antenna. A similar technique was developed in [71, 72], where fields radiated by an infinitesimal antenna are used to calculate the impedance of antennas with finite dimensions. We consider an electrically small loop antenna with radius ρ_T. Since $\rho_T \ll \lambda$, we can approximate the current density distribution by a constant over the antenna surface [73, 74]. This approximation simplify the electromagnetic analysis and is suitable for modeling LWD sensors.

6.2.2 Mutual Impedance

The antenna impedance also depends on the current of neighboring elements. The impedance at a port a due to the current at port b is called mutual impedance. The variational formula that calculates the mutual impedance at the receiver antenna due to the current at the transmitter antenna is given by [51]

$$Z_{\mathrm{RX,TX}} = -\frac{\langle \mathbf{E}_{\mathrm{TX}}, \mathbf{J}_{s,\mathrm{RX}} \rangle}{I_{\mathrm{TX}} I_{\mathrm{RX}}} \tag{6-3}$$

$$= -\frac{1}{I_{\mathrm{TX}} I_{\mathrm{RX}}} \oiint \mathbf{E}_{\mathrm{TX}} \cdot \mathbf{J}_{s,\mathrm{RX}} \, ds. \tag{6-4}$$

Reciprocally, the impedance at the transmitter antenna due to the current at the receiver antenna is given by

$$Z_{\mathrm{TX,RX}} = -\frac{\langle \mathbf{E}_{\mathrm{RX}}, \mathbf{J}_{s,\mathrm{TX}} \rangle}{I_{\mathrm{TX}} I_{\mathrm{RX}}} \tag{6-5}$$

$$= -\frac{1}{I_{\mathrm{TX}} I_{\mathrm{RX}}} \oiint \mathbf{E}_{\mathrm{RX}} \cdot \mathbf{J}_{s,\mathrm{TX}} \, ds. \tag{6-6}$$

6.3 Horizontal Electric Coil with Rectangular Cross-Section

Several commercial LWD sensors use coil antennas with a rectangular cross-section similar to the illustrated in Figure 6.2. Horizontal coil excites only TM to z modes. Due to this feature equation (6-1) becomes

$$Z_{\mathrm{in}} = -\frac{1}{I_{\mathrm{TX}}^2} \oiint E_{\phi}^{\mathrm{TE}} \cdot \mathbf{J}_s \, ds. \tag{6-7}$$

Considering that E_{ϕ}^{TE} is independent of ϕ, and that the current is constant along the antenna surface, (6-7) can be solved by splitting the integral

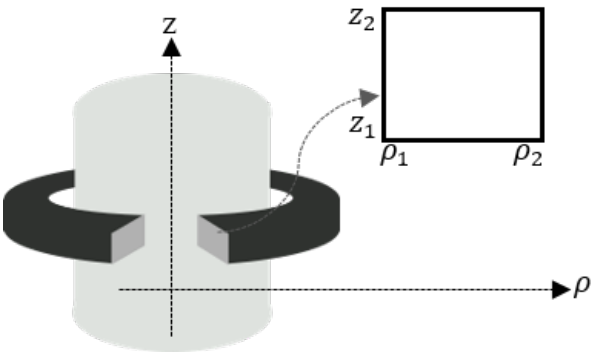

Figure 6.2: Coil antenna with a rectangular cross-section.

into four line integrals

$$Z_{\text{in}} = -\frac{J_s}{I_{\text{TX}}^2} 2\pi \Bigg[\int_{\rho_1}^{\rho_2} E_\phi^{\text{TE}}(\rho, z_1)\rho \; d\rho \; + \; \rho_2 \int_{z_1}^{z_2} E_\phi^{\text{TE}}(\rho_2, z) \; dz \\ - \; \int_{\rho_2}^{\rho_1} E_\phi^{\text{TE}}(\rho, z_2)\rho \; d\rho \; - \; \rho_1 \int_{z_2}^{z_1} E_\phi^{\text{TE}}(\rho_1, z) \; dz \Bigg], \quad (6\text{-}8)$$

where ρ_1, ρ_2, z_1 and z_2 are illustrated in Figure 6.2.

The same logic is applied for calculating the mutual impedance. We could divide the integral in expressions (6-3) and (6-5) into four integrals similar to those presented in (6-8).

6.3.1 Input Impedance Characteristics

To illustrate the application of the proposed method, we present some case studies that describe the operation of LWD tools in different representative scenarios. We compare our results with FDTD provided by the software CST Studio Suite [75]. The real dimensions of a typical logging-well could not be properly simulated in CST due to the considerable amount CPU time required, and due to severe convergence problems, we have faced. Due to this reason, we will present FDTD comparisons using only scaled versions of the original well. Despite that numerical issues, a comprehensive validation of our method will be possible. The input current was defined as $I_{\text{TX}} = 1$ A for all the cases presented here.

6.3.2 Case Study 1

In a first case study, we consider a problem with a 4-in-radius metallic mandrel inside a 7-in-radius borehole, where 1 in $= 2.54\times10^{-2}$ m. The borehole is filled with oil-based mud with 5×10^{-4} S/m, and the soil formation has 1 S/m.

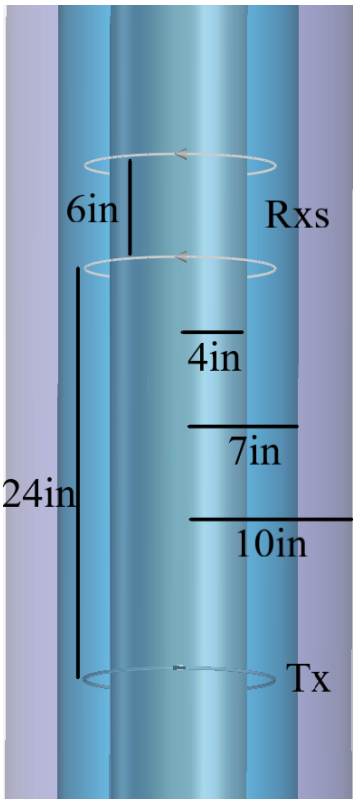

Figure 6.3: Geophysical formation and the geometry for the case study 1.

Figure 6.3 illustrates the geophysical formation and the main parameters. As said before, to avoid very long simulations times in the FDTD method, the radial domain was truncated at 10 in. The operating frequency ranges from 0.5 MHz to 2 MHz, as typical for resistivity sensing. In this problem, the infinitesimal loops have radii of $\rho_T = 5.5$ in. The axial separation between TX and RXs are 24 in and 30 in, as illustrated in Figure 6.3. The real and imaginary parts of the voltage received at the RXs as a function of the operating frequency are shown in Figure 6.4 and Figure 6.5. Good agreement is observed between the voltage computed by the proposed method and those from a commercial finite-difference time-domain (FDTD) solver.

We have calculated the impedance of a coil antenna with rectangular cross-section given by a width of $\Delta\rho = 0.2$ in and a height varying in the range of $\Delta z = \{10, 16\}$ in. Figure 6.6 shows the impedance of these two real antennas as the frequency evolves from 0.5 MHz–2 MHz. Good agreement is observed versus FDTD results.

6.3.3 Case Study 2

As a second example, we consider a formation similar to that presented above, but now we investigate the influence of the conductivity of the soil

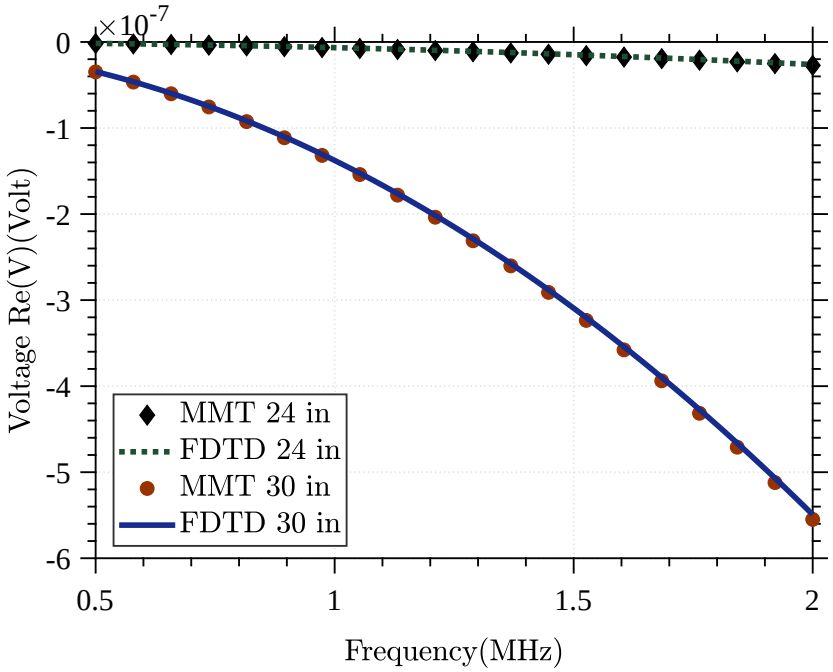

Figure 6.4: Real part of the voltages received at RX antennas axially placed 24 in and 30 in away from the TX.

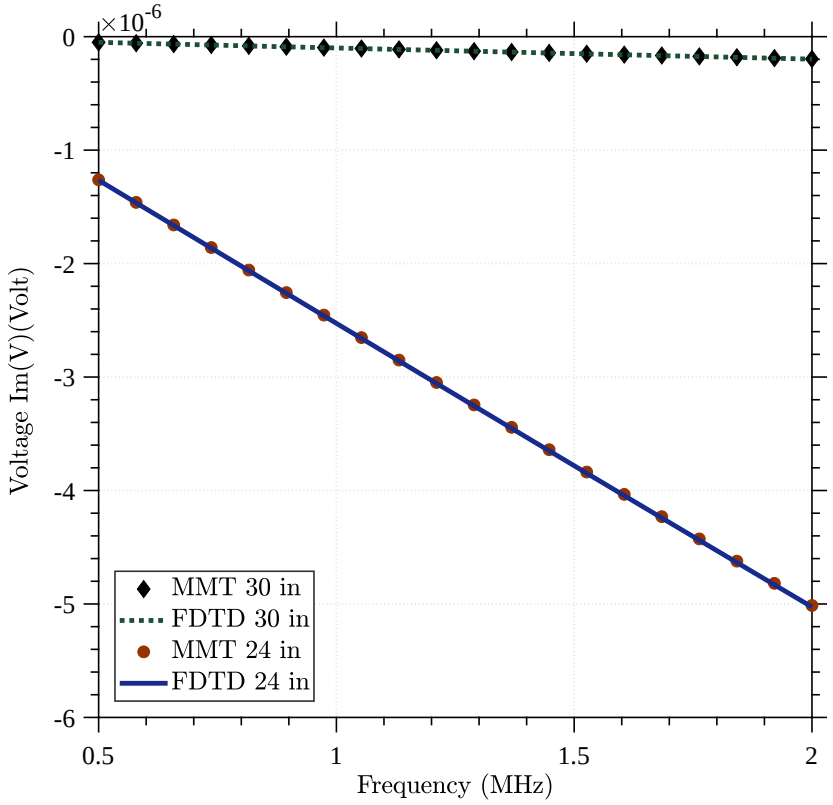

Figure 6.5: Imaginary part of the voltages received at RX antennas axially placed 24 in and 30 in away from the TX.

formation. Figure 6.7 shows the impedance of an antenna with cross-section $\Delta\rho = 0.2$ in by $\Delta z = 10$ in operating at 500 kHz and 2 MHz as the conductivity

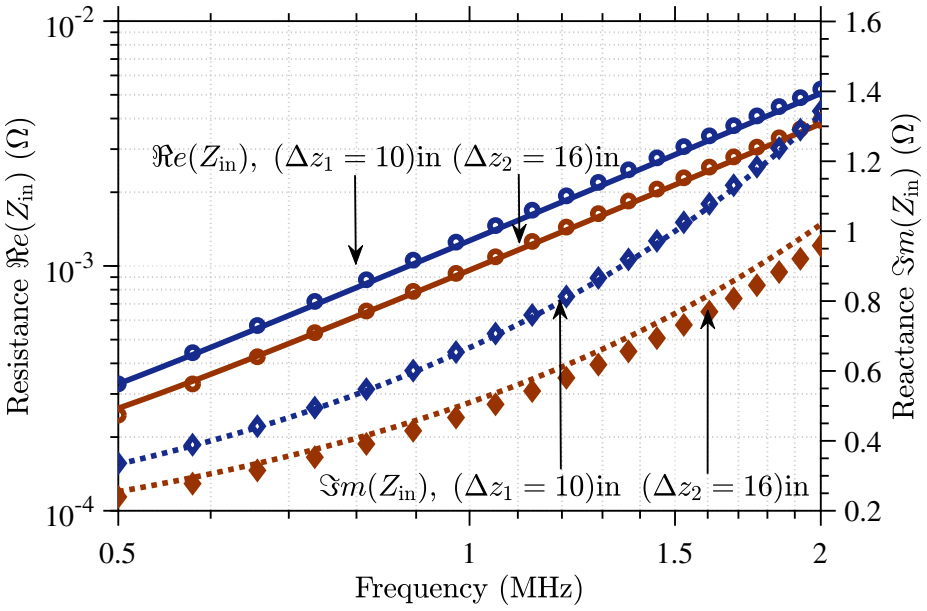

Figure 6.6: Impedance of the antenna with cross-section width $\Delta\rho = 0.2$ in and heights $\Delta z = 10$ in and 16 in. The results from the present algorithm are indicated by small symbols. The solid and dotted lines are FDTD results.

of the soil formation evolves.

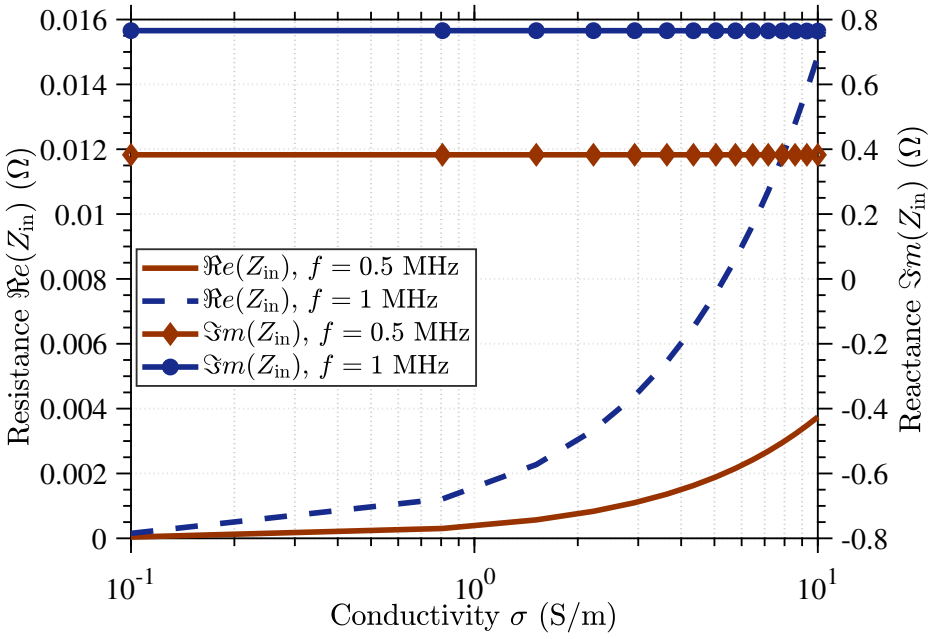

Figure 6.7: Impedance of the antenna as a function of the soil conductivity.

6.3.4 Case Study 3

We next evaluate a scenario similar to case study 1, but now we investigate the influence of the antenna dimensions. Figure 6.8 and Figure 6.9

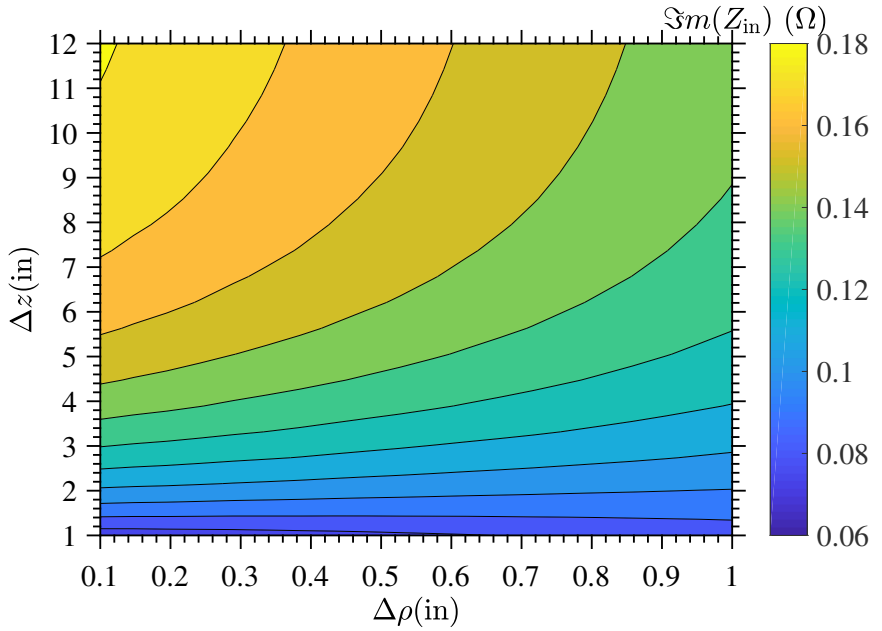

Figure 6.8: Input reactance of the antenna as a function of the cross-section width $\Delta\rho$ and height Δz.

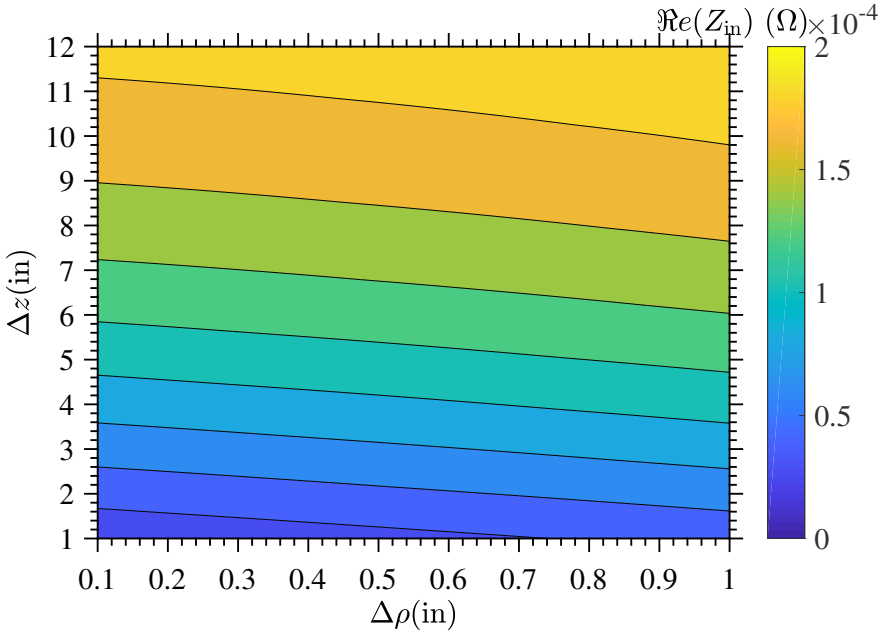

Figure 6.9: Input resistance of the antenna as a function of the cross-section width $\Delta\rho$ and height Δz.

show impedance results as a function of the antenna width $\Delta\rho$ and height Δz, when the operating frequency is fixed at 0.5 MHz.

6.4 Summary of Chapter 6

The sensitivity analysis shows that the antenna impedance changes dramatically in terms of its dimensions, operating frequency, and parameters

of the medium where it is immersed. The analysis results motivated us to investigate another kind of antennas and their practical applications in the LWD industry. A preliminary mathematical formulation for other candidate antennas is presented in Appendix A. It is worth noting that because the infinitesimal coil (placed at the center of the real dimension antennas), is very close to the antenna surface, we require to compute the electric field in some points in the cross-section antenna more than 100 radial modes until the convergence ($p > 100$). It should be stressed that many convergence issues where observed in the FDTD simulations (in CST) due to the complexity associated with this kind of problem. In face of that, just the limited number of case studies displayed above where considered. The study of other antenna geometries and the calculation of its input impedance when immersed in more complex backgrounds becomes out of the scope of the present work.

7
Final Remarks and Recommendations for Future Works

In this thesis we presented a comprehensive study on the electromagnetic propagation in complex geophysical formations for the accurate modeling of well-logging tools. We focused on computing the induced voltages and the self-impedance of coil antennas used in such sensors. We presented some novel full-wave, variational, and perturbational pseudo-analytic methods to describe electromagnetic propagation in complex geophysical formations that can handle realistic LWD tools. The mathematical formulation and the associated numerical algorithms we have developed allows us to account for the effects of an azimuthal symmetric borehole environment with the additional presence of complex-shaped 3D anisotropic scatterers. As far as we know, the proposed pseudo-analytic method is less resource-intensive both in terms of CPU time de RAM requirements when compared with the alternative solutions addressed in the literature.

To the best of our knowledge, we obtained, for the first time, a semi-analytic dyadic Green's function for inhomogeneous cylindrically layered media with both vertical and radial stratifications.

In this research, BA and EBA field solutions were formulated and numerically implemented for modeling the electromagnetic propagation in environments where a 3D anisotropic-magnetodielectric object is immersed. Our approach requires a volumetric integral only over the object region instead of a numerically expensive integral over the entire domain as in the standard BA formulation.

We presented a variational technique for computing the input impedance in realistic LWD sensors immersed in dissipative and inhomogeneous media. The numerical results show that the technique presented herein can describe the LWD tools accurately.

The CPU time and the required computer memory for numerically solving the proposed kind of problems can be prohibitive, even in scaled cases. Our proposal overcomes these problems and contributes to a better understanding of the physical electromagnetic phenomena that occur in these structures.

The limitations of the perturbational methods proposed in this research

are related to the scatterer size and the abrupt variations of σ and μ; thus, the electromagnetic effects of a small scatterer with constitutive parameters not very different from those of the background media will be correctly represented using the say BA and EBA solutions, as shown in Chapter 4.

An essential characteristic of MMT is that this method is presented as a modal sum of eigenfields. When transmitter and receiver are very close to each other (TX→RX), a large number of series terms are required until the convergence. It may affect the performance of the impedance computation considerably due to the proximity between the transmitter (infinitesimal coil) and receiver (real antenna surface), especially for small dimension devices. The same effect may be observed in the BA-based solutions when the scatterer is near the RXs. This is because the scatterer acts as an equivalent source.

As future works, we propose the following recommendations:

- Further studies on EBA and other BA variants, it will require to efficiently take advantage of the algorithms programmed in this thesis. The study of more cases based on BA will allow us to have more precise results and to evaluate cases with a greater contrast between the background media and the scatterer medium.
- Extend the formulation proposed in this thesis, as well as EBA and others related to BA techniques, to directional wells. Directional drilling prevails in modern oilfields exploration. Being a topic of great industrial interest, a detailed and in-depth study would have a great scientific contribution.
- Further studies on the modeling of the self-impedance of realistic antennas other than the presented here, such as toroidal-coils and tilted-coil antennas. They were not addressed in this thesis due to the lack of computational resources or bibliographic examples to present a comparison and validation of the method.
- Compare our BA results with full-wave solver to explore the limits of the representativeness of the presented perturbational algorithm. A comparison with FDTD or 3D-FEM is desirable; it requires an electromagnetic simulation software such as COMSOL, and a powerful computer, especially for solving the scatterer fields of non-symmetric objects.
- Study on the depolarization dyadics [76, 77] to avoid the singularity associated with the calculation of the fields within the source region, that is, in the limit $z_s \rightarrow z_{TX}$. It will also help us to avoid a great computational effort in the vicinity of the vertical boundaries.

Bibliography

[1] T. H. H. Tobin, "Proceedings of the integrated ocean drilling program; expedition 348 of the riser drilling platform from and to shimizu," in *Proceedings of the Integrated Ocean Drilling Program*, vol. 348, 2015.

[2] Darwin V. Ellis, Julian M. Singer, *Well Logging for Earth Scientists*. Dordrech: Springer, 2007.

[3] Schlumberger, "Arcvision312," 2007. [Online]. Available: https://www.slb.com/-/media/files/drilling/brochure/arcvision-br.ashx

[4] ——, "Neoscope," 2012. [Online]. Available: https://www.slb.com/drilling/surface-and-downhole-logging/logging-while-drilling-services/neoscope-sourceless-formation-evaluation-while-drilling-service

[5] G. S. Rosa, "Pseudo-analytical modeling for electromagnetic well-logging tools in complex geophysical formations," Ph.D. dissertation, Pontifical Catholic University of Rio de Janeiro, Rio de Janeiro, RJ, Brazil, 2017.

[6] G. Huchital, "Apparatus and method for determination of subsurface permittivity and conductivity," U.S. Patent 4209747, June 1980.

[7] "ADR azimuthal deep resistivity sensor datasheet," Halliburton Sperry Drilling, Houston, TX, USA, 2016.

[8] "EarthStar^{TM} Ultra-Deep Resistivity Service datasheet," Halliburton Sperry Drilling, Houston, TX, USA, 2018.

[9] Weatherford, "EarthStar^{TM} Ultra-Deep Resistivity Service," 2018. [Online]. Available: https://www.weatherford.com/en/documents/brochure/products-and-services/drilling/magnus-rss

[10] Halliburton, "Oilfield Technology MLWD QA," 2017. [Online]. Available: https://www.halliburton.com/content/dam/ps/premium/ss/contents/Papers_and_Articles/web/Oilfield-Technlogy-2017MLWD-QA.pdf

[11] ——, "EarthStar Ultra-Deep Resistivity Service," 2018. [Online]. Available: https://www.halliburton.com/content/dam/ps/public/ss/contents/Data_Sheets/web/EarthStar-Service-Datasheet.pdf

[12] ——, "AFR Azimuthal Focused Resistivity Sensor," 2016. [Online]. Available: https://www.halliburton.com/content/dam/ps/public/ss/contents/Data_Sheets/web/H05666.pdf

[13] "PeriScope datasheet," Schlumberger, Houston, TX, USA, 2008.

[14] "iriSphere datasheet," Schlumberger, Houston, TX, USA, 2019.

[15] H. O. Lee, F. L. Teixeira, L. E. S. Martin, and M. S. Bittar, "Numerical modeling of eccentered LWD borehole sensors in dipping and fully anisotropic earth formations," *IEEE Trans. Geosci. Remote Sens.*, vol. 50, no. 3, pp. 727–735, Mar. 2012.

[16] H.-H. Wu, C. Golla, T. Parker, N. Clegg, and L. Monteilhet, "A New Ultra-Deep Azimuthal Electromagnetic LWD Sensor for Reservoir Insight," in *SPWLA 59th Annual Logging Symposium*. Society of Petrophysicists and Well-Log Analysts, Jun. 2018. [Online]. Available: https://www.onepetro.org/conference-paper/SPWLA-2018-X

[17] S. Sheng, K. Li, F. Kong, and B. Wang, "Investigation of a Conductivity Logging Tool Based on Single Coil Impedance Measurement Using FDTD Method," *Progress In Electromagnetics Research*, vol. 39, pp. 171–180, 2014. [Online]. Available: http://www.jpier.org/pierm/pier.php?paper=14091905

[18] D. S. Pixton, "Very High-Speed Drill String Communications Network," Novatek, Tech. Rep. 41229R14, Aug. 2002. [Online]. Available: https:https://www.osti.gov/servlets/purl/829805

[19] W. Li, Z. Nie, and X. Sun, "Wireless Transmission of MWD and LWD Signal Based on Guidance of Metal Pipes and Relay of Transceivers," *IEEE Trans. Geosci. Remote Sens.*, vol. 54, no. 8, pp. 4855–4866, Aug. 2016.

[20] Y.-K. Hue, "Analysis of electromagnetic well-logging tools," Ph.D. dissertation, The Ohio State University, Columbus, OH, USA, 2006.

[21] G. S. Rosa, J. R. Bergmann, and F. L. Teixeira, "A robust mode-matching algorithm for the analysis of triaxial well-logging tools in anisotropic geophysical formations," *IEEE Trans. Geosci. Remote Sens.*, vol. 55, no. 5, pp. 2534–2545, May 2017.

[22] M. S. Novo, L. C. da Silva, and F. L. Teixeira, "Three-dimensional finite-volume analysis of directional resistivity logging sensors," *IEEE Trans. Geosci. Remote Sens.*, vol. 48, no. 3, pp. 1151–1158, Mar. 2010.

[23] G.-S. Liu, F. Teixeira, and G.-J. Zhang, "Analysis of directional logging tools in anisotropic and multieccentric cylindrically-layered earth formations," *IEEE Trans. Antennas Propagat.*, vol. 60, no. 1, pp. 318–327, Jan. 2012.

[24] G. S. Rosa, J. R. Bergmann, and F. L. Teixeira, "A perturbation method to model electromagnetic well-logging tools in curved boreholes," *IEEE Trans. Geosci. Remote Sens.*, vol. 56, no. 4, pp. 1979–1993, 2018.

[25] Y.-K. Hue and F. L. Teixeira, "Analysis of tilted-coil eccentric borehole antennas in cylindrical multilayered formations for well-logging applications," *IEEE Trans. Antennas Propagat.*, vol. 54, pp. 1058–1064, 2006.

[26] L. Zhong, J. Li, A. Bhardwaj, L. C. Shen, and R. C. Liu, "Computation of triaxial induction logging tools in layered anisotropic dipping formations," *IEEE Trans. Geosci. Remote Sens.*, vol. 46, no. 4, pp. 1148–1163, April 2008.

[27] Z. Nie, Z. Liu, and X. Sun, "A multirelay cooperation method for wireless transmission of MWD and LWD signals," *IEEE Transactions on Geoscience and Remote Sensing*, vol. 56, no. 3, pp. 1229–1237, 2018.

[28] Y. Fang, J. Dai, Q. Zhan, Y. Hu, M. Zhuang, and Q. H. Liu, "A hybrid 3-d electromagnetic method for induction detection of hydraulic fractures through a tilted cased borehole in planar stratified media," *IEEE Trans. Geosci. Remote Sens.*, pp. 1–9, 2019.

[29] Y. Fang, J. Dai, Z. Yu, J. Zhou, and Q. H. Liu, "Through-casing hydraulic fracture evaluation by induction logging i: An efficient em solver for fracture," *IEEE Trans. Geosci. Remote Sens.*, vol. 55, no. 2, pp. 1179–1188, Feb. 2017.

[30] H. O. Lee and F. L. Teixeira, "Cylindrical FDTD analysis of LWD tools through anisotropic dipping-layered earth media," *IEEE Trans. Geosci. Remote Sens.*, vol. 45, no. 2, pp. 383–388, Feb. 2007.

[31] J. Li, J. Zhuo, Z. Guan, F. Han, and Q. H. Liu, "3-d electromagnetic scattering and inverse scattering by magnetodielectric objects with arbitrary anisotropy in layered uniaxial media," *IEEE Transactions on Antennas and Propagation*, vol. 68, no. 2, pp. 1009–1022, Feb 2020.

[32] G. Gao and C. Torres-Verdin, "Efficient Numerical Simulation of Axisymmetric Electromagnetic Induction Measurements Using a High-Order Generalized Extended Born Approximation," *IEEE Trans. Geosci. Remote Sens.*, vol. 44, no. 9, pp. 2445–2453, Sep. 2006.

[33] Z. Xiong, "Electromagnetic modeling of 3-D structures by the method of system iteration using integral equations," *GEOPHYSICS*, vol. 57, no. 12, pp. 1556–1561, 1992.

[34] S. G. Gao and C. Torres-Verdín, "A New Approximation for 3D Electromagnetic Scattering in the Presence of Anisotropic Conductive Media," in *3DDMIII Workshop*, Adelaide, Feb. 2003.

[35] K. Yang and A. E. Yilmaz, "FFT-Accelerated Analysis of Scattering From Complex Dielectrics Embedded in Uniaxial Layered Media," *IEEE Trans. Geosci. Remote Sens.*, vol. 10, no. 4, pp. 662–666, Jul. 2013.

[36] T. J. Cui and W. C. Chew, "Fast algorithm for electromagnetic scattering by buried 3-D dielectric objects of large size," *IEEE Trans. Geosci. Remote Sens.*, vol. 37, no. 5, pp. 2597–2608, Sep. 1999.

[37] W. C. Chew, *Waves and Fields in Inhomogeneous Media*. New York, NY, USA: John Wiley & Sons, 1995.

[38] C. Torres-Verdín and T. M. Habashy, "Rapid 2.5-dimensional forward modeling and inversion via a new nonlinear scattering approximation," *Radio Science*, vol. 29, no. 04, pp. 1051–1079, July 1994.

[39] C. Torres-Verdin and T. M. Habashy, "Rapid numerical simulation of axisymmetric single-well induction data using the extended born approximation," *Radio Science*, vol. 36, no. 6, pp. 1287–1306, Nov. 2001.

[40] T. M. Habashy, R. W. Groom, and B. R. Spies, "Beyond the born and rytov approximations: A nonlinear approach to electromagnetic scattering," *J. Geophys. Res.*, pp. 1759–1775, 1993.

[41] H. Tseng, K. H. Lee, and A. Becker, "3d interpretation of electromagnetic data using a modified extended born approximation," *GEOPHYSICS*, vol. 68, no. 1, pp. 127–137, 2003.

[42] G. Gao and C. Torres-Verdin, "High-order generalized extended born approximation for electromagnetic scattering," *IEEE Trans. Antennas Propagat.*, vol. 54, no. 4, pp. 1243–1256, Apr. 2006.

[43] G. S. Rosa, J. R. Bergmann, and F. L. Teixeira, "Full-wave pseudoanalytical methods for cylindrically symmetric electromagnetic structures: Applications in sensing and telemetry for geophysical exploration," in *Antennas, Antenna Arrays and Microwave Devices: Electromagnetic Analysis and Applications*,

T. Bauernfeind, Ed. World Scientific Publishing Co, 2020, ch. 4, to appears. See https://www.worldscientific.com/worldscibooks/10.1142/10987.

[44] W. C. Chew, J. M. Jin, and E. Michielssen, "Complex coordinate stretching as a generalized absorbing boundary condition," *Microw. Opt. Tech. Lett.*, vol. 15, no. 6, pp. 363–369, Aug. 1997.

[45] W. C. Chew and W. H. Weedon, "A 3D perfectly matched medium from modified Maxwell's equations with stretched coordinates," *Microw. Opt. Tech. Lett.*, vol. 7, pp. 599–604, 1994.

[46] Z. S. Sacks, D. M. Kingsland, and R. L. and, "A perfectly matched anisotropic absorber for use as an absorbing boundary condition," *IEEE Trans. Antennas Propagat.*, vol. 43, no. 12, pp. 1460–1463, Dec. 1995.

[47] F. L. Teixeira and W. C. Chew, "Complex space approach to perfectly matched layers: a review and some new developments," *Int. J. Num. Model.*, vol. 13, pp. 441–455, 2000.

[48] J. W. Brown and R. V. Churchill, *Complex Variables and Applications*, 7th ed. New York, NY, USA: McGrawHill, 2004.

[49] M. Petkovic, B. Neta, L. Petkovic, and J. Dzunic, *Multipoint Methods for Solving Nonlinear Equations*. New York: Elsevier Science, 2012.

[50] W. H. Press, S. A. Teukolsky, W. T. Vetterling, and B. P. Flannery, *Numerical recipes: the art of scientific computing*, 3rd ed. New York, NY, USA: Cambridge University Press, 2007.

[51] R. F. Harrington, *Time-harmonic electromagnetic fields*. New York, NY, USA: McGraw-Hill, 1961.

[52] V. H. Rumsey, "Reaction concept in electromagnetic theory," *Phys. Rev.*, vol. 94, pp. 1483–1491, Jun. 1954.

[53] M. Abramowitz and I. A. Stegun, *Handbook of Mathematical Functions: With Formulas, Graphs, and Mathematical Tables*. New York, NY, USA: Dover Publications, 1964.

[54] D. M. Pozar, *Microwave Engineering*, 3rd ed. Hoboken, NJ, USA: John Wiley & Sons, Inc., 2005.

[55] A. Abubakar and T. M. Habashy, "A green function formulation of the extended born approximation for three-dimensional electromagnetic modelling," *Wave Motion*, vol. 41, no. 3, pp. 211 – 227, 2005.

[56] A. Abubakar and P. van den Berg, "Iterative forward and inverse algorithms based on domain integral equations for three-dimensional electric and magnetic objects," *Journal of Computational Physics*, vol. 195, no. 1, pp. 236–262, 2004.

[57] L. Gelius, "Electromagnetic scattering approximations revisited," *Progress In Electromagnetics Research*, vol. 76, pp. 75–94, 2007.

[58] Z. Q. Zhang and Q. H. Liu, "The hybrid extended born approximation and CG-FFHT method for axisymmetric media," *IEEE Trans. Geosci. Remote Sens.*, vol. 39, no. 4, pp. 710–717, April 2001.

[59] M. Yuan and Q. Liu, "The diagonal tensor approximation (DTA) for objects in a non-canonical inhomogeneous background," *Progress In Electromagnetics Research*, vol. 112, pp. 1–21, 2011.

[60] P. Imperatore, A. Iodice, and D. Riccio, "Volumetric-perturbative reciprocal formulation for scattering from rough multilayers," *IEEE Trans. Antennas Propagat.*, vol. 58, no. 3, pp. 877–887, Mar. 2011.

[61] L. Saavedra, G. S. Rosa, and J. R. Bergmann, "An accurate technique for modeling realistic well-logging sensors inside complex media," in *International Applied Computational Electromagnetics Society Symposium (ACES)*, April 2019, pp. 1–2.

[62] ——, "A novel semi-analytical mode-matching technique for modeling realistic electromagnetic well-logging sensors immersed in dissipative inhomogeneous media," in *International Symposium on Electromagnetic Theory*, May 2019, pp. 1–4.

[63] M. Novo, "Numerical analysis of electromagnetic well-logging tools by using finite volume methods," Ph.D. dissertation, Pontifical Catholic University of Rio de Janeiro, Rio de Janeiro, RJ, Brazil, 2007, DOI: 10.17771/PUCRio.acad.11478.

[64] D.-Y. Na, B.-H. V. Borges, and F. L. Teixeira, "Finite element time-domain body-of-revolution maxwell solver based on discrete exterior calculus," *Journal of Computational Physics*, vol. 376, pp. 249 – 275, 2019.

[65] J. X. Liu, W. C. Zhu, J. Liu, J. C. Sheng, B. H. Brady, and C. A. Tang, "Simulation of progressive borehole failure at multi-lateral junctions," *Petroleum Science and Technology*, vol. 25, no. 9, pp. 1185–1198, 2007.

[66] Q. H. Liu and W. C. Chew, "Numerical mode-matching method for the multiregion vertically stratified media," *IEEE Trans. Antennas Propagat.*, vol. 38, no. 4, pp. 498–506, Apr. 1990.

[67] Q.-H. Liu and W. C. Chew, "Diffraction of nonaxisymmetric waves in cylindrically layered media by horizontal discontinuities," *Radio Science*, vol. 27, no. 5, pp. 569–581, 1992.

[68] M. dos Santos Canabarro, "Aplicação do método de casamentos de modos com b-splines de múltiplos nós ao estudo de perfilagem de poços petrolíferos," Ph.D. dissertation, Pontifical Catholic University of Rio de Janeiro, Rio de Janeiro, RJ, Brazil, 2016.

[69] G. S. Rosa, M. S. Canabarro, J. R. Bergmann, and F. L. Teixeira, "A comparison of two numerical mode-matching methodologies for the analysis of inhomogeneous media with radial and vertical stratifications," *IEEE Transactions on Antennas and Propagation*, vol. PP, pp. 1–1, 09 2018.

[70] J. Galejs, "Impedance of Linear Antennas in the Presence of a Stratified Dielectric," in *Antennas in inhomogeneous media*. New York: Pergamon Press, 1969.

[71] C. V. Dodd and W. E. Deeds, "Analytical Solutions to Eddy-Current Probe-Coil Problems," *Journal of Applied Physics*, vol. 39, no. 6, pp. 2829–2838, May 1968.

[72] J. R. Bowler and T. P. Theodoulidis, "Eddy currents induced in a conducting rod of finite length by a coaxial encircling coil," *Journal of Physics D: Applied Physics*, vol. 38, no. 16, p. 2861, 2005.

[73] C. A. Balanis, "Loop Antennas," in *Antenna Theory: Analysis and Design*, 4th ed. Hoboken, New Jersey: Wiley, Feb. 2016.

[74] P. S. Carter, "Circuit Relations in Radiating Systems and Applications to Antenna Problems," *Proceedings of the Institute of Radio Engineers*, vol. 20, no. 6, pp. 1004–1041, Jun. 1932.

[75] CST AG, CST Studio Suite 2019, Darmstadt, Germany, 2019.

[76] Y. Rahmat-Samii, "On the question of computation of the dyadic green's function at the source region in waveguides and cavities," *IEEE Transactions on Microwave Theory and Techniques*, vol. 23, no. 9, pp. 762–765, Sep. 1975.

[77] R. E. Collin, "On the incompleteness of e and h modes in wave guides," *Canadian Journal of Physics*, vol. 51, no. 11, pp. 1135–1140, 1973.

A
Impedance Modeling of Some Typical LWD-Sensing Antennas

A.1
Horizontal Electric Coil with Circular Cross-Section

Some LWD tools use arranges of coil antennas with circular cross-section of radius ρ_1 like the illustrated in Figure A.1. As presented in Section 6.3 horizontal coil excites only TM to z modes and we could use (6-7) to calculate the input impedance. Considering the fact that E_ϕ^{TE} is independent of ϕ, and the current is constant along the antenna surface (6-7) can be solved by

$$Z_{\mathrm{in}} = -\frac{J_s}{I_{\mathrm{TX}}^2} 2\pi \int_0^{2\pi} E_\phi^{\mathrm{TE}}(\gamma)\rho \, d\gamma, \tag{A-1}$$

where

$$\rho = \rho_0 + \rho_1 \cos\gamma, \tag{A-2}$$

$$z = z_0 + \rho_1 \sin\gamma, \tag{A-3}$$

$$\gamma = \arctan\left(\frac{z - z_0}{\rho - \rho_0}\right), \tag{A-4}$$

where z_0 and ρ_0 are the coordinates of the center of the circle.

To calculate mutual impedance of a circular cross-section antenna, we could applied the same parametrization above in (6-3) and (6-5).

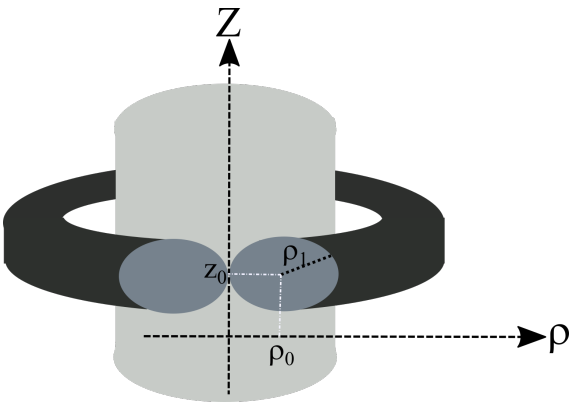

Figure A.1: Horizontal electric coil with circular cross-section

A.2
Tilted-Coil Antennas

A tilted-coil antenna as depicted in Figure 2.6 excites hybrid modes with azimuthal index $n \neq 0$. Then, we should consider all the electric fields associated with those azimuthal harmonics for computing the antenna impedance. In the case of a square cross-section wire, the parameters ρ_1 and ρ_2 are fixed trough ϕ, while z_1 and z_2 change with the azimuthal angle ϕ. In this scenario, we can calculate the input impedance by using

$$Z_{\text{in}} = -\frac{J_s}{I_{\text{TX}}^2}\Bigg[\int_0^{2\pi}\int_{\rho_1}^{\rho_2}\mathbf{E}(\rho, z_1, \phi)\,\rho\,d\rho\,d\phi + \rho_2\int_0^{2\pi}\int_{z_1}^{z_2}\mathbf{E}(\rho_2, z, \phi)\,dz\,d\phi - \int_0^{2\pi}\int_{\rho_2}^{\rho_1}\mathbf{E}(\rho, z_2, \phi)\rho\,d\rho\,d\phi - \rho_1\int_0^{2\pi}\int_{z_2}^{z_1}\mathbf{E}(\rho_1, z, \phi)\;dz\,d\phi\Bigg], \tag{A-5}$$

where

$$z_1 = z_0 - \frac{\Delta}{2} - \rho\tan\theta_T\,\cos(\phi - \phi_T), \tag{A-6}$$

$$z_2 = z_0 + \frac{\Delta}{2} - \rho\tan\theta_T\,\cos(\phi - \phi_T), \tag{A-7}$$

Δ describes the thickness of the antenna, ϕ_T and θ_T are the azimuthal and elevation tilt angles, as illustrated in Figure 2.6.

For tilted antennas width circular cross-section we have

$$Z_{\text{in}} = -\frac{J_s}{I_{\text{TX}}^2}\int_0^{2\pi}\int_0^{2\pi}\mathbf{E}(\gamma, \phi)\,\rho\,d\gamma\,d\phi, \tag{A-8}$$

where ρ is defined in (A-2) and z is

$$z = z_0 + \rho_1\sin\gamma - \rho\tan\theta_T\,\cos(\phi - \phi_T), \tag{A-9}$$

$$\gamma = \arctan\left[\frac{z - z_0 + \rho\tan\theta_T\,\cos(\phi - \phi_T)}{\rho - \rho_0}\right]. \tag{A-10}$$

Similar process can be used to determine mutual impedance of tilted antennas.